Materials Chemistry of Superprotonic Solid Acids

Thesis by

Mikhail N. Kislitsyn

In Partial Fulfillment of the Requirements

for the Degree of

Doctor of Philosophy

California Institute of Technology

Pasadena, California

2009

Acknowledgements.

First and foremost, I'd like to thank my advisor, Dr. Sossina Haile. Her support, guidance and personal example throughout my time at Caltech developed my abilities to continue to educate myself and learn how to approach any problem. With that, I feel fully prepared for any life path I'd like to choose. I must also thank Caltech and the Materials Science department for giving me the opportunity to study at an amazing place, and option representative Dr Brent Fultz for guidance. I'm also blessed to be surrounded by extraordinary scientists, co-workers and friends and there are just too many to mention everyone.

Next, I'd like to mention two special people Mike Vondrus and his wife Masako, for their support and help. I was delighted to feel as a part of your family, when you allowed me to stay at your place for several months, which felt like home away from home.

I have to thank my parents for their support and the sacrifices they made, accepting my choice to continue my study overseas, even though that meant they would not see me for five years.

I must acknowledge Dr Andrew Yaroslavtsev, who was my undergraduate mentor for five years and my high school chemistry teacher Valentina Vasilievna Blednyh. Their mentorship has shaped my and life and helped me to appreciate science and academic research.

Last but never the least; I must mention my wonderful wife Judy. She truly made my last year here at Caltech the best, despite the stress of the thesis preparation and facing career choices.

Abstract

Solid acid is a class of materials that shows potential as a fuel cell electrolyte. Understanding the phase and mechanical stability are required for further development of this technology. We addressed both issues in this work.

We expanded the use of the crystallographic theory of the phase transformation to three major classes of solid acids. That allowed us to relate material properties hysteresis to fundamental crystallographic and thermodynamic parameters. The understanding of the mechanism of the transformation can guide the effort to create materials with desired hysteresis. Careful investigation of the thermal and phase behavior of $CsHSO_4$, CsH_2PO_4, $Rb_3H(SeO_4)_2$ and in $Cs_{1-x}Rb_xH_2PO_4$ solid solution series for both low and high temperature phases was performed and crystal symmetry and lattice parameters for $Cs_{0.75}Rb_{0.25}H_2PO_4$, $T=240^0C$ phase were found for the first time. Consistency between predicted and measured properties was shown for all three different classes of solid acids as well as for the isostructural solid solution series.

Nanocomposite materials based on cesium hydrogen sulfate and nanometer size silica were characterized. We observed 30-40 nm size surface stabilization of our material at the high temperature phase, otherwise metastable at room temperature. We developed methods to quantitatively study interface phases and its effect on ion mobility. The method allowed us to quantitatively find crystalline and amorphous amounts in the composites. We observed 3-4 order decrease in spin-lattice relaxation values of the metastable phase in the composite. Solid state NMR allowed surface interactions directly and suggest high ion mobility. Strong effect on superprotonic transition temperature in composites was observed. Superprotonic phase was stable in composites at temperatures up to 70^0C below phase transition compared with pure phase $CsHSO_4$.

The mechanism and activation energy of the creep plastic deformation in $CsHSO_4$ were found. Based on that, a method to reduce creep by 1-2 orders of magnitude was developed and creep-resistant material was synthesized.

Table of Contents

Appendixes

A-1. Supplemental diffraction information

A-1. LaB$_6$ standard for powder X-ray diffraction.

List of Figures

List of Tables.

Chapter 1.   Introduction

1.1 Overview of solid acid materials

Solid acids are intermediates between the normal salt and normal acids. At room temperatures solid acids are similar to ionic salts and most of them are white brittle insulating crystalline powders, highly water soluble. Water solubility and ease to grow large good optical quality single crystals, along with a non-centrosymmetric crystal structure, determine the interest to the first extensively studied solid acid: KH_2PO_4[1]. As a crystal, it is noted for its non-linear optical properties and used in optical modulators and for non-linear optics.

Most of the solid acid materials have a proton conductivity $10^{-6}\ldots 10^{-9}\,\Omega^{-1}cm^{-1}$ at room temperature and are not attractive as a fuel cell electrolyte at this conditions. Unique property of solid acids to undergo order-disorder solid state phase transition at elevated temperatures was discovered[2] in 1981-1982 for $CsHSO_4$. Resulting high temperature phase[3] has a proton conductivity increase by three-four orders of magnitude. Although initially use of the solid acids in electrochemical devices, such as fuel cells, are thought to be challenging due to its water solubility. When Haile *et al.*[4] demonstrated proof-of-principle a solid acid fuel cell based on $CsHSO_4$, it drew significant interest to the solid acids materials. Electrochemical, thermodynamic, and phase behavior of the solid acids followed[5,6,7,8,9]

The presence of the hydrogen network in the structure leads to interesting properties of the solid acids.

In this work we will focus on three major classes of solid acids. We will classify them by symmetry relationship between low temperature and high temperature phases.

1. $MHXO_4$ monoclinic – tetragonal.

Example: $CsHSO_4$

2. MH_2XO_4 monoclinic – cubic.

Example: CsH_2PO_4

3. $M_3H(XO_4)_2$ monoclinic – hexagonal.

Example: $Rb_3H(SeO_4)_2$

The specific choice of these three classes of materials is due to their potential practical importance (for example CsH_2PO_4) as well as existence of literature studying those materials.

1.2 Properties of the hydrogen-bond network

The hydrogen atom and the corresponding ion have several unique properties. Most of it is due to its extremely small radius. The key feature of the solid acids materials is a hydrogen network. There are four possible types of the network: 0-D, 1-D, 2-D, 3-D. In general, the higher the ratio between XO_4 group and numbers of hydrogen ion in the structure, the higher the likeliness to form a high-dimensional network.

Table 1 Examples of the hydrogen networks

Dimensionality	Configuration	Ratio of the H/XO_4	Example
0-D	Dimers	1:2	$Rb_3H(SO_4)_2$
1-D	Chains	1:1	$CsHSO_4$

2-D	Layers	3:2	$Cs_2HSO_4H_2PO_4$
3-D	Network	2:1	CsH_2PO_4

The hydrogen mobility at the low temperature phase is usually limited to the presence of the intrinsic defects in the structure where thermally activated hydrogen ions jump between equivalent positions in the hydrogen bond.[10]

1.3 Phase transitions in solid acids

All previously described classes of the solid acids experience first order, order-disorder phase transitions at elevated temperatures. Phase transformations in the solid acids are enthropy driven and were extensively studied in, for example, [11]. In this work we will focus on a crystallographic relationship between low temperature and high temperature phases. In Chapter 4 we will focus on the application of the austenite-martensite theory of phase transformations in solid acids. The approach allows us to connect fundamental crystallographic parameters to the transition properties, such as hysteresis of the phase transformations. Relating mechanical compatibility to the crystallographic parameters allows us to engineer by chemical substitution, materials with desired properties. Examples of this theoretical approach will be shown in Chapters 5 and 6.

1.4 Influence of the inert media on the conductivity and phase transition

Proton conducting solid acids are not the only type of ion conductors to experience ionic phase transformations. It is not uncommon for many ion conducting

materials to have a solid-solid transformation with several order increase in conductivity. There is however an interesting effect observed in many materials. Before the "superionic" phase transformation, ion conductivity of the material is usually quite low. Large body of literature showed that adding non-reactive and insulating phases, such as Al_2O_3, SiO_2 or TiO_2, can increase the ion conductivity by several orders of magnitude. The effect was first studied in β-AgJ and LiJ with Al_2O_3[12],[13] followed by the composite materials based on solid acids[14],[15]. Study of the solid acid composites are mostly focused on the effect on conductivity and only briefly mentioned the mechanism and materials interaction in the system. In Chapters 5 and 6 we will study $CsHSO_4/SiO_2$ in detail. We will focus on developing and applying quantitative methods of the phase analysis based on diffraction techniques. We will quantitatively describe the system at all composition and temperatures. In Chapter 6 we will directly study surface interaction by solid state NMR techniques.

1.5 Mechanical properties of the solid acids

Solid acids experience superionic phase transition at temperatures close to melting or decomposition. Long term operations in a fuel cell or any other device require mechanical stability. In Chapter 7 we will describe our effort to study long term stability of the solid acid materials under compressive stress, simulating a fuel cell system. Only a few literature reports are known to address mechanical properties of the solid acids. They mostly focus on cesium hydrogen sulfate. Uda *et al.* postulated formation of the microcracks caused by thermal expansion with its healing due to plastic flow of the material in the superprotonic phase, thus leading to no alteration in conductivity[16] and

solid acids' poor thermal stability[9]. Urusovskaya et al.[17] showed the ability of the cesium hydrogen sulfate to plastically deform up to 5% strains under relatively low stresses (5MPa). In Chapter 7 we will determine the amount and the mechanism of the plastic deformation under constant stress. We will discuss possible ways of prevention and show the development of creep-resistant cesuim hydrogen sulfate based material.

References

[1]Busch, G. and P. Scherrer (1935). "A new seignette-electrical substance." Naturwissenschaften **23**: 737-737.

[2] Komukae, M., T. Osaka, et al. (1981). "Dielectric and Thermal Studies on New Phase-Transitions of Cshso4." Journal of the Physical Society of Japan **50**(10): 3187-3188..

[3] Baranov, A. I., L. A. Shuvalov, et al. (1982). "Superion Conductivity and Phase-Transitions in Cshso4 and Cshseo4 Crystals." Jetp Letters **36**(11): 459-462..

[4] Haile, S. M., D. A. Boysen, et al. (2001). "Solid acids as fuel cell electrolytes." Nature **410**(6831): 910-913.

[5] Uda, T., D. A. Boysen, et al. (2005). "Thermodynamic, thermomechanical, and electrochemical evaluation of CsHSO4." Solid State Ionics **176**(1-2): 127-133.

[6] Boysen, D. A. (2004) Superprotonic Solid Acids: Structure, Properties, and Applications. California Institute of Technology.

[7] Norby, T. (2001). "The promise of protonics." Nature **410**(6831): 877-878.

[8] Haile, S. M. (2003). "Fuel cell materials and components." Acta Materialia **51**(19): 5981-6000.

[9]Boysen, D. A., T. Uda, et al. (2004). "High-performance solid acid fuel cells through humidity stabilization." Science **303**(5654): 68-70.

[10] Baranov, A. I. (1987). "Anomalies of Proton Conductivity under Structural Phase-Transitions in Crystals with Hydrogen-Bonds." Izvestiya Akademii Nauk Sssr Seriya Fizicheskaya **51**(12): 2146-2155.

[11] Chisholm, C. (2003) Superprotonic Phase Transition in Solid Acid: Parameters affecting the presence and stability of superprotonic transitions in the MH_nXO_4. California Institute of Technology.

[12] Wagner, J. B. (1980). "Transport in Compounds Containing a Dispersed 2nd Phase." Materials Research Bulletin **15**(12): 1691-1701.

[13] Jow, T. and J. B. Wagner (1979). "Effect of Dispersed Alumina Particles on the Electrical-Conductivity of Cuprous Chloride." Journal of the Electrochemical Society **126**(11): 1963-1972.

[14] Ponomareva, V. G., G. V. Lavrova, et al. (1999). "The influence of heterogeneous dopant porous structure on the properties of protonic solid electrolyte in the CsHSO4-SiO2 system." Solid State Ionics **118**(3-4): 317-323.

[15] Otomo, J., H. Shigeoka, et al. (2005). "Phase transition behavior and proton conduction mechanism in cesium hydrogen sulfate/silica composite." Journal of Physics and Chemistry of Solids **66**(1): 21-30.

[16] Uda, T., D. A. Boysen, et al. (2005). "Thermodynamic, thermomechanical, and electrochemical evaluation of CsHSO4." Solid State Ionics **176**(1-2): 127-133.

[17] Urusovskaya, A. A. and L. F. Kirpichnikova (1998). "Specific features of plastic deformation in CsHSO4 crystals." Crystallography Reports **43**(2): 307-310.

Chapter 2.   Experimental methods

2.1 Synthesis of the solid acids

Crystalline solid acids were synthesized from aqueous solutions, containing stoichiometric quantities of the corresponding ions:

$$Cs^+ \quad + \quad HSO_4^{2-} \; = \; CsHSO_4$$

$$Cs^+ \quad + \quad H_2PO_4^{2-} \; = \; CsH_2PO_4$$

$$Rb^+ \quad + \quad H_2PO_4^{2-} \; = \; RbH_2PO_4$$

Precipitations from aqueous solutions were carried out by (1) heating to evaporate excess water, and (2) solvent introduction to saturated water solution. Single crystals were obtained by slow water evaporation from the saturated water solutions. Crystalline powders were dried to remove excessive water. Detailed descriptions of the synthesis are included in Appendix (A-1).

2.2 X-ray powder diffraction

X-ray powder diffraction characterization was carried out using Panalytical X'pert Pro diffractometer with Cu K_α radiation, $\lambda=1.5418$ Å and an applied voltage and current 45 kV, 40 mA, respectively. Scanned 2 theta range was 5-70^0 with step size of 0.017 degrees 2 theta. Anton Paar HTK1200 high temperature furnace was used for non-ambient temperature measurements. Internal thermocouple in the chamber was regularly calibrated with the use of the external thermocouple, since large (up to 70^0 C) discrepancies between internal thermocouple and actual temperatures were confirmed to be regular by the manufacturer at temperatures below 500-600^{0}C, for details see Appendix A-2.

Depending on the quality of the data required, different collection times were used. In typical general phase characterization and analysis we used 10s time per step. In quantitative phase and composition analysis, we used time per step of up to 50s.

Powder diffraction techniques on a single crystal leads to the appearance of many parasitic secondary reflections. The mirror stage, which uses a highly parallel and focused beam, was used to eliminate that effect. This produces clean pattern. Instrumental peak broadening was measured using LaB_6 as a standard. Detailed techniques of crystalline size measurement is described in Appendix A-2.

Powders were ground in the mortar for similar particle size distribution and diffraction patterns were obtained at room temperature. Identical sample preparation technique, amount of the sample and data collection conditions were used for absolute comparison of peak intensities between different samples.

Philips X'Pert Plus software was utilized to perform Reitveld refinements of the unknown phases[1].

2.3 X-ray powder absorption spectroscopy

Diffraction patterns from powder samples are routinely used for sample identification and phase analysis. Powder X-ray diffraction is ideally positioned for quantitative multiphase analysis, since each phase has its unique set of the diffracted intensities. First work in this field was done by Clark et al[2]. Although due to the absence of precise radiation counters, measurements sometimes lacked the desired precision. Only recently, with a high speed high resolution X-ray diffractometer, is the method becoming more attractive and easily applicable.

The key concept in the diffraction-absorption analysis is to properly account for absorption of each component of the mixture. The first theoretical description was given by Klug et al[3]. The assumptions of uniform sample with small enough particle size were used. We will use the following equations to apply the method to our solid acid composite systems.

The total intensity of the i-th component by some selected (hkl) is given by

$$I_i = \frac{K_i * f_i}{\mu}.$$

Equation 2-1 The total intensity of the i-th component by some selected (hkl)

where

K_i – constant, depends on the nature of the component and geometry of the XRD system,

f_i – volume fraction of the i-th component,

μ - linear absorption coefficient of the powder mixture.

We can rewrite Equation 2-1 using more practical mass absorption coefficient of each component and weight fraction of the components:

$$I_i = \frac{K_i * x_i / \rho_i}{\sum \mu_i^m * x_i}.$$

Equation 2-2 The total intensity of the i-th component as a function of mass-absorption coefficient

where

μ_i^m , x_i– mass absorption coefficient and weight fraction of the component i

ρ_i – density of the component i.

Let's derive the expression for relative intensity of the three-component system:

Absolute intensity for pure component 1 will be –

$$I_1^0 = \frac{K_1}{\rho_1 * \mu_1^m}.$$

Equation 2-3 Absolute intensity for pure component 1

Absolute intensity of the component 1 in the mixture of 3 components –

$$I_1 = \frac{K_1 * x_1 / \rho_1}{(\mu_1^m * x_1 + \mu_2^m * x_2 + \mu_3^m * x_3)}.$$

Equation 2-4 Absolute intensity of the component 1 in the mixture of 3 components

We will get relative intensity for the component 1 in the mixture by dividing Equation 2-3 by Equation 2-4.

$$\frac{I_1}{I_1^0} = \frac{\mu_1^m * x_1}{(\mu_1^m * x_1 + \mu_2^m * x_2 + \mu_3^m * x_3)} \quad \text{or} \quad \frac{I_1}{I_1^0} = \frac{\mu_1^m * x_1}{\sum_{i=1}^{n} \mu_i^m * x_i}.$$

Equation 2-5 Relative intensity of component 1 in the mixture of 3 or n components

where in our case,

μ_1^m and x_1 – mass absorption coef. and weight fraction of the phase-III

μ_2^m and x_2 - mass absorption coef. and weight fraction of the phase -II

μ_3^m and x_3 – mass absorption coef. and weight fraction of of the SiO_2.

We will demonstrate how we can apply this method to complex mixtures of crystalline and amorphous components.

2.4 NMR Spectroscopy

Magic Angle Spinning Solid State NMR measurements were performed using Bruker DSX 500 at 11.7 T and magic angle spinning at 12kHz and using 4 μs, 90^0 pulse with repetition delay time 5 times the relaxation time. Empty rotor proton background was obtained and subtracted from the spectra. Spin-lattice relaxation time was measured by inversion recovery pulse sequence or saturation recovery pulse sequence.

2.5 Impedance Analysis

Impedance spectroscopy method was used to determine the ionic conductivity of the samples. The conductivity was measured on a pressed pellet, unless otherwise specified. In some cases, wet nitrogen or wet argon was used to prevent sample dehydration. Silver paste (Ted Pella) was applied on the sides of the pellets and was used as electrodes. A.C. impedance data were collected over the frequency range of 20 Hz – 1 MHz using an HP 4284 precision LCR meter at an applied voltage of 500 mV. Appropriate equivalent circuit was used to describe the data. Zview (Scribner Associates Inc.) software was used for data analysis.

2.6 Scanning Electron Microscopy

LEO 1550 VP Filed Emission Scanning electron microscope, equipped with in-lens SE, below-lens SE, variable pressure SE, Robinson-type BSE detectors and Oxford

INCA Energy 300 X-ray Energy Dispersive Spectrometer (EDS) system were used for particle size and composition analysis of the samples. Low voltage was used during imaging to avoid local overheating and decomposition of the solid acid samples.

2.7 Dilatometer and TMA measurements

Linseis dilatometer and Perkin Elmer TMA 7 Thermomechanical Analyzer was utilized for creep testing of the solid acids at different measurements and stress loads. Typical applied force was 2-7 N for TMA and up to 0.5 N for the dilatometer at temperatures of $100\text{-}260^{0}C$. The major difference between dilatometer and thermomechanical analyzer (TMA) is that TMA allows using higher stresses.

2.8 Thermal Analysis

Neztsch STA 449 thermal analyzer equipped with a Pfeiffer Vacuum Thermal Star attachment was used for thermogravimetric analysis and differential scanning calorimetry. Experiments were performed under flowing of argon, unless otherwise specified.

References

[1] X'Pert Plus. Philips Analytical B.V.: Almelo, 1999.2. X'Pert HighScore. Philips Analytical B.V.: Almelo, 2002.

[2] Clark, G. L. and D. H. Reynolds (1936). "Quantitative analysis of mine dusts - An x-ray diffraction method." Industrial and Engineering Chemistry-Analytical Edition **8**: 36-40.

[3] Klug H, Alexander L, X-ray diffraction procedures for polycrystalline and amorphous materials, p 413, New York, Willey, 1954.

Chapter 3. Crystallographic approach to the phase transitions in three classes of solid acids

3.1 Theory of the austenite-martensite transformations

3.1.1 Basic concepts

The method which connects in quantitative matter crystallography, microstructure and macroscopic parameters in austenite-martensite phase transformation was developed by D. James and K. Bhattacharya. It was successfully applied to several classes of the solid state transformations, primarily shape-memory alloys. That allowed engineering desired properties of the materials, based on fundamental parameters[1]. In this chapter I will try to give a brief description of the theory necessary for understanding its application to three classes of the solid acid phase transitions. For additional information and further details please refer to the "Microstructure of Martensite[2]" by Kaushik Bhattacharya and other references[3],[4],[5]. I will identify and show the key criterion, which makes this theory applicable to our class of materials.

The theory of the austenite-martensite transformation was first developed to (1) describe the microstructure evolution during transformation, and (2) connect the thermal hysteresis in the phase transitions to the crystallographic parameters of the transformation. It is generally applicable to the solid to solid phase transformations where structure changes rapidly. High temperature high symmetry phase is usually called austenite and low symmetry low temperature phase is called martensite. There is a historic reason, behind that, as first observation of the needle-like structures was made in steel. Cooling the austenite phase below certain transition temperature, causes transition

from high symmetry lattice to low symmetry. The transformation has to be and first order

(abrupt thermodynamic properties change) with ultimately no diffusion. An example of

the transformation is shown in Figure 3-1.
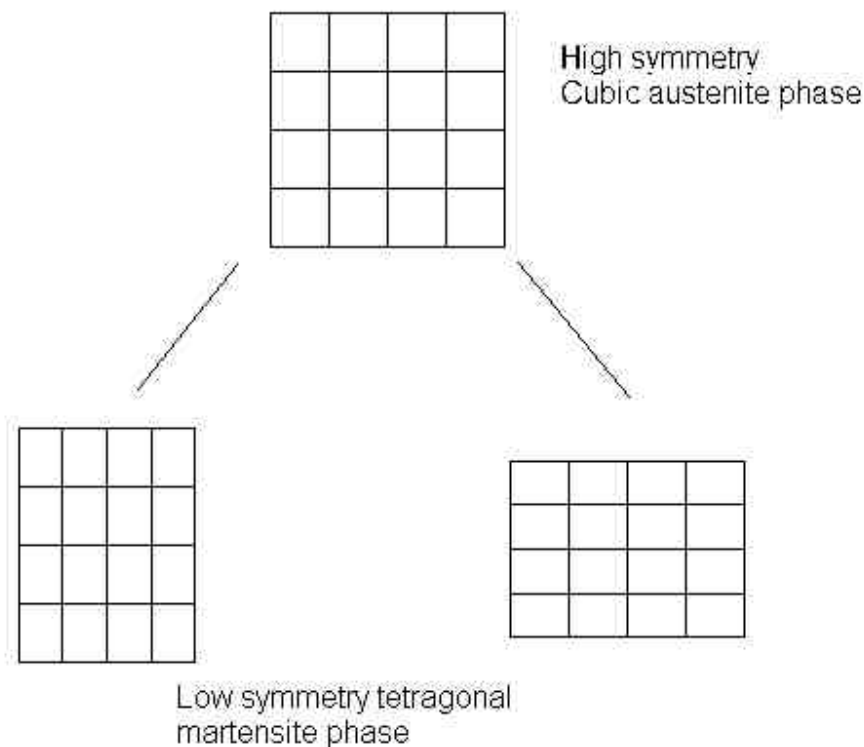
Figure 3-1 Example of the 2-D cubic – tetragonal austenite-martensite

transformation

Upon heating the martensite phase it will transform back to the austenite. The

temperature difference between forward and reverse transformation is called hysteresis.

One of the major tasks of this work is to connect hysteresis in solid acid phase

transformations to the fundamental crystallographic and thermodynamic properties.

As you can see from the example in Figure 3-1, there are two distinct geometrical

configurations of the martensite. It is always possible to write a matrix of transformation

from austenite to martensite. In general, to determine the number of different variants of the martensite phase we would need to apply all symmetry operations from the austenite symmetry group, which are not in the martensite symmetry group.

Expression for the possible number of variants:

$$N = \frac{\text{Austenite point group order}}{\text{Martensite point group order}}$$

Equation 3-1

N- number of possible variants.

The central concept of the crystallographic theory of the austenite-martensite transformation is based on the ability of the different variants to form coherent stress free interfaces with the other variant and with the austenite. An example of that type of microstructural behavior is shown below
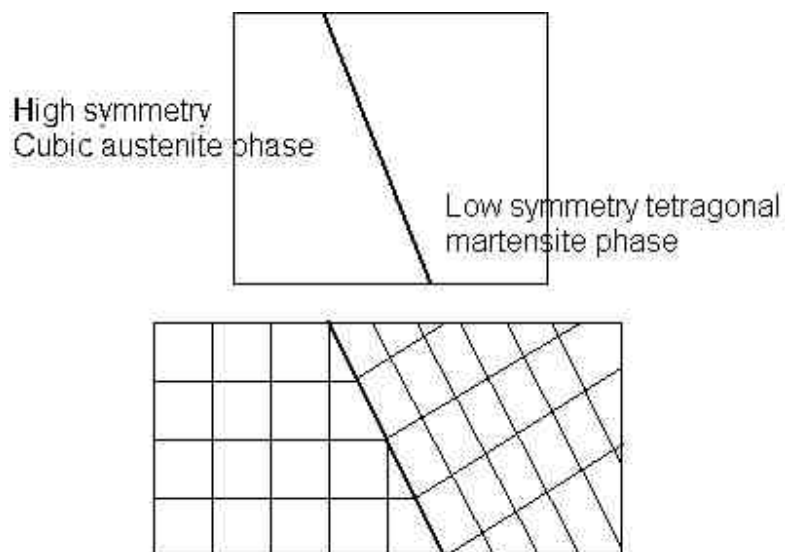
Figure 3-2 Schematic example of the stress-free interfaces

3.1.2 Constructing the transformation matrix

For a correct transformation matrix we need a so-called lattice correspondence. It is a structural relationship between austenite and martensite phases. It identifies the structural unit in the austenite that transforms into the martensite and a corresponding deformation. Assuming $\begin{pmatrix} a_o^m \\ b_o^m \\ c_o^m \end{pmatrix}$ is a basis vector of the martensite phase and $\begin{pmatrix} a_o^a \\ b_o^a \\ c_o^a \end{pmatrix}$ basis vector of the austenite phase, the choice of the lattice vectors in austenite and martensite phases is critical and reflects the transformation mechanism and materials' chemistry. Non-symmetric transformation matrix can always be written for vector transformations. T_1 matrix is not unique and there are several symmetry-related transformation matrices, the number of which is determined by Equation 3-1.

$$\begin{pmatrix} a_o^m \\ b_o^m \\ c_o^m \end{pmatrix} = T_1 * \begin{pmatrix} a_o^a \\ b_o^a \\ c_o^a \end{pmatrix}.$$

Equation 3-2

We can find other transformation matrices as described in[2]. In order to do so, we need to make matrix T_1 symmetric. Matrix T_1 is not symmetric in a general case. We can apply the procedure described in[2] to find all symmetric transformation matrices from one known non-symmetric transformation matrix T_1.

$$T_1 = QU_1.$$

Equation 3-3

Where Q is a rotation and U_1 is the positive-definite symmetric Bain matrix. According to the idea of frame-indifference, the state of the lattice is left unchanged since T_1 and U_1 are related by a rotation. To find U_1, first calculate

$$C = T^t_1 * T_1.$$

Equation 3-4

Next, the positive root of $\mu_i = \sqrt{\gamma_i}$ (i = 1, 2, 3) is taken, where the eigenvalues of the matrix C are γ_i and they are positive because C is a positive-definite matrix. Matrices U_1 and C share the same eigenvectors. The Bain matrix, U_1, with eigenvalues $\{\mu_1, \mu_2, \mu_3\}$ and eigenvectors $\{u_1, u_2, u_3\}$, is given by:

$$\mathbf{U}_1 = \mu_1 \mathbf{u}_1 \otimes \mathbf{u}_1 + \mu_2 \mathbf{u}_2 \otimes \mathbf{u}_2 + \mu_3 \mathbf{u}_3 \otimes \mathbf{u}_3.$$

Equation 3-5

Since all U_i are related by rotations, they will share same eigenvalues and sets of the eigenvectors, related by the same rotation. To find other variants we need to apply all the possible rotations of the austenite group R. Variants will be related as

$$U_i = R^t * U_1 * R.$$

Equation 3-6

In our case there will be:

12 variants for monoclinic-cubic transformation

4 variants for monoclinic-tetragonal transformation

3 variants for monoclinic-hexagonal transformation.

3.1.3 Compatibility criteria between austenite-martensite and martensite-martensite interfaces

Following Ball and James[6], we will show the route of selecting geometrically compatible variants of martensite and the austenite phase. The general idea consists of two steps:

1. Find variants pair geometrically compatible between each other

2. Check if they are compatible with the austenite phase.
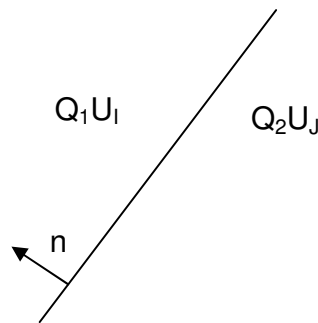
Figure 3-3 Two variants of the martensite phase

Two variants of the martensite can form a twin, (Figure 3-3) when you can find rotations Q_1 and Q_2, so that:

$$\mathbf{Q}_1\mathbf{U}_I - \mathbf{Q}_2\mathbf{U}_J = b \otimes n.$$

Equation 3-7

Figure 3-3 shows example of that interface. Multiplying Equation 3-7 by Q_2^T and setting $Q = Q_2^T {}_* Q_1$ and $a = Q_2^T {}_* b$, we can write Equation 3-8. Equation 3-8 called twining equation and its solution (Q, a and n) will fully describe martensite-martensite twinning interface.

Matensite-martensite twin can form when:

$$\mathbf{QU}_I - \mathbf{U}_J = \mathbf{a} \otimes \mathbf{n}.$$

Equation 3-8

where n-vector normal to the interface and a-vector along direction of shear.

Equation 3-8 has a solution if, and only if, the eigenvalues of the matrix

$$\Re = \mathbf{U}_J^{-T} \mathbf{U}_I^T \mathbf{U}_I \mathbf{U}_J^{-1}.$$

Equation 3-9

satisfy the condition of $\lambda_1 \leq 1$, $\lambda_2 = 1$, $\lambda_3 \geq 1$.

The matrix $\Re$ describes one variant deformation relative to the other, with the stretches given by eigenvalues. To make two sides coherent we will have to find a plane that is unstretched, which is possible only when we have one stretch equal and two others surround the one.

If the condition of $\lambda_1 \leq 1$, $\lambda_2 = 1$, $\lambda_3 \geq 1$ holds, there are exactly two solutions of Equation 3-8 providing two sets of a and n vectors:

$$\mathbf{a} = \rho \left(\sqrt{\frac{\lambda_3(1-\lambda_1)}{\lambda_3 - \lambda_1}} \mathbf{e}_1 + \kappa \sqrt{\frac{\lambda_1(\lambda_3 - 1)}{\lambda_3 - \lambda_1}} \mathbf{e}_3 \right)$$

Equation 3-10

and

$$\mathbf{n} = \frac{\sqrt{\lambda_3} - \sqrt{\lambda_1}}{\rho\sqrt{\lambda_3 - \lambda_1}} \left(-\sqrt{1-\lambda_1} \mathbf{U}_J^T \mathbf{e}_1 + \kappa\sqrt{\lambda_3 - 1} \mathbf{U}_J^T \mathbf{e}_3 \right).$$

Equation 3-11

where $\kappa = \pm 1$, and ρ is non-zero and chosen such that $|\mathbf{n}| = 1$. As with Equation 3-7, two solutions (one for $\kappa = 1$ and one for $\kappa = -1$) are expected, a-vector and e_i are the eigenvectors of the matrix $\mathfrak{R}$ in Equation 3-9.

Solutions of the twinning equations: vectors a and n, define characteristics of the twin interface – twinning shear ($|a|*|U^{-1}_j*n|$), the direction of shear ($a/|a|$) and twin plane $(U^{-1}_j*n/|U^{-1}_j*n|$.

The solution above is general, but a shorter way is possible for the special case, when disappearance of the 180-degree rotation from austenite group, but not in martensite, gives rise to the twinning system. It is often the case for this type of the transformation. It will be shown that some of the possible twinning interfaces in CsH_2PO_4 and $CsHSO_4$ are created by 180^0 rotation from austenite group. In this case we can solve Equation 3-8, which also gives us two solutions

1. $\mathbf{a} = 2\left(\dfrac{\mathbf{U}_J^{-T}\mathbf{v}}{\left|\mathbf{U}_J^{-T}\mathbf{v}\right|^2} - \mathbf{U}_J\mathbf{v} \right), \qquad \mathbf{n} = \mathbf{v},$

Equation 3-12

where v-axes of the 180^0 rotation, and

2. $\mathbf{a} = \rho\mathbf{U}_J\mathbf{v}, \qquad \mathbf{n} = \dfrac{2}{\rho}\left(\mathbf{v} - \dfrac{\mathbf{U}_J^T\mathbf{U}_J\mathbf{v}}{\left|\mathbf{U}_J\mathbf{v}\right|^2} \right).$

Equation 3-13

In the first solution (Equation 3-12) twinning plane is the plane of the symmetry of the austenite – Type-I twin.

In the second solution (Equation 3-13) shearing direction is a direction of the symmetry in the austenite – Type-II twin.

In the case when the solution satisfies both equations and both twinning plane and twinning directions are rational - these are called Compound twins.

Next, we need to calculate which one of the martensitic twins are compatible with the austenite phase.
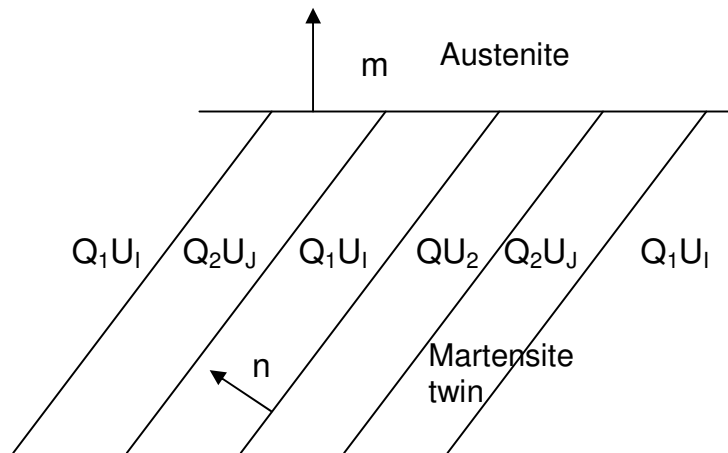
Figure 3-4 Austenite-martensite interface

Austenite-martensite interface can be schematically shown (Figure 3-4). The interface can be described by vectors normal to the interface (m).

The interface is defined by the solution to the twinning equation and the austenite-martensite interface equation:

1. Twinning equation

$$\mathbf{QU}_I - \mathbf{U}_J = \mathbf{a} \otimes \mathbf{n}.$$

Equation 3-14

2. Austenite-martensite interface equation

$$\mathbf{Q'}(l\mathbf{QU}_J + (1-l)\mathbf{U}_I) = \mathbf{I} + \mathbf{b} \otimes \mathbf{m}.$$

Equation 3-15

where l is some scalar satisfying $0 \leq l \leq 1$ and corresponds to the relative amounts of the two variants of martensite. **m** is the unit vector normal to the interface (Figure 3-4).

Ball and James[5] showed detailed solutions of these equations. We will just outline major steps towards it, following[2].

1. Calculate

$$\delta = \mathbf{a} \cdot \mathbf{U}_I (\mathbf{U}_I^2 - \mathbf{I})^{-1} \mathbf{n},$$

Equation 3-16

and $\eta = \mathrm{tr}(\mathbf{U}_I^2) - \det(\mathbf{U}_I^2) - 2 + \dfrac{|\mathbf{a}|^2}{2\delta}$,

Equation 3-17

while $\delta \leq -2$, $\eta \geq 0$.

2. To find the solutions, calculate

$$l = \frac{1}{2}\left(1 - \sqrt{1 + \frac{2}{\delta}}\right).$$

Equation 3-18

3. Find

$$C^* = (\mathbf{U}_I + l\mathbf{n} \otimes \mathbf{a})(\mathbf{U}_I + l\mathbf{a} \otimes \mathbf{n}).$$

Equation 3-19

4. Find eigenvalues and eigenvectors of C^* (e_1, e_2, e_3), then the solution for the austenite-martensite equation will be:

$$\mathbf{b} = \rho\left(\sqrt{\frac{\lambda_3(1 - \lambda_1)}{\lambda_3 - \lambda_1}}\mathbf{e}_1 + \kappa\sqrt{\frac{\lambda_1(\lambda_3 - 1)}{\lambda_3 - \lambda_1}}\mathbf{e}_3\right)$$

Equation 3-20

$$\mathbf{m} = \frac{\sqrt{\lambda_3} - \sqrt{\lambda_1}}{\rho\sqrt{\lambda_3 - \lambda_1}}\left(-\sqrt{1 - \lambda_1}\,\mathbf{e}_1 + \kappa\sqrt{\lambda_3 - 1}\mathbf{e}_3\right).$$

Equation 3-21

where $\kappa = \pm 1$, ρ is chosen such that $|\mathbf{m}| = 1$, and $\lambda_1 \leq \lambda_2 \leq \lambda_3$ with $\lambda_2 = 1$, are the

eigenvalues corresponding to the eigenvectors (e_1, e_2, e_3) of matrix C^*.

5. if $\delta < -2$, repeat step 3 after replacing l with $1 - l$.

The austenite-martensite compatibility equation (Equation 3-15) implies the

criteria $\lambda_1 \leq \lambda_2 \leq \lambda_3$ with $\lambda_2 = 1$ is for acceptable solution. In the case of the $\lambda_2 = 1$, stress-

free interface between austenite and single variant of the martensite is possible.[1] Near the

transformation temperature free energies of the austenite and variants of martensite are

very close, making possible the creation of complex microstructures. The condition of

$\lambda_2 = 1$ is usually not achieved by one variant of the martensite, but a fine mixture of

variants with fractions defined by l, and is approximately compatible with austenite.

The interface is a transition layer containing elastic energy, and the fineness of the

microstructure is determined by a competition between the elastic energy stored in the

transition layer and the interfacial energy on the twin boundaries between the variants[1].

The incompatibility between austenite and martensite, there is both elastic and

interfacial energy stored owing to the presence of the two phases. This occurs in both

directions of the transformation, and in the case of temperature change, the temperature

must be raised sufficiently above the transformation temperature on heating, or below on

cooling, to supply the additional free energy, leading to hysteresis. The further value of λ_2

from one, higher degree of overheating or undercooling would be needed, widening the hysteresis of the phase transformation.

3.1.4. Summary

A described mathematical approach will allow us to find compatible interfaces between high and low temperature phases of the solid acids in a precise geometrical nature. The result is given as a set of the directions in which certain interfaces are compatible as well as twin volume fractions. Connection between the transformation parameter λ_2 and hysteresis width is established.

3.2 Modeling the phase transition for certain structural types of solid acids

   3.2.1 MHXO$_4$ – monoclinic to tetragonal

The compound CsHSO$_4$ displays a sequence of phase transitions described by the following scheme:

   phase III (P2$_1$/c) $\xrightarrow{\text{60-100 }^\circ\text{C}}$ phase II (P2$_1$/c) $\xrightarrow{\text{141 }^\circ\text{C}}$ phase I (I4$_1$/amd) ,
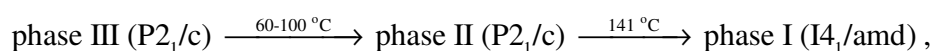
where phase I, the tetragonal phase, is superprotonic in nature. Accordingly, the martensite – austenite transition corresponds here to that between phase II and phase I. Phase III is generally obtained on room temperature synthesis of CsHSO$_4$, however, the reverse transformation of II → III on cooling is extremely sluggish (requiring several days) and is not detectable by methods such as thermal analysis or conductivity measurements performed on typical timescales. The compound CsHSeO$_4$ is isostructural to CsHSO$_4$. Domain structure of the CsHSO$_4$ was studied by Merinov et al.[7] and a possible mechanism was established: phases share the same plane (a$_t$b$_t$ and a$_m$b$_m$) and deformation during the transition occurs in the direction of the c$_t$ and can be represented by the spontaneous deformation vector. It was suggested by Merinov et al.[8] on the basis of domain pattern formation, we take the monoclinic and tetragonal cell parameters to be related according to Equation 3-22-Equation 3-26.
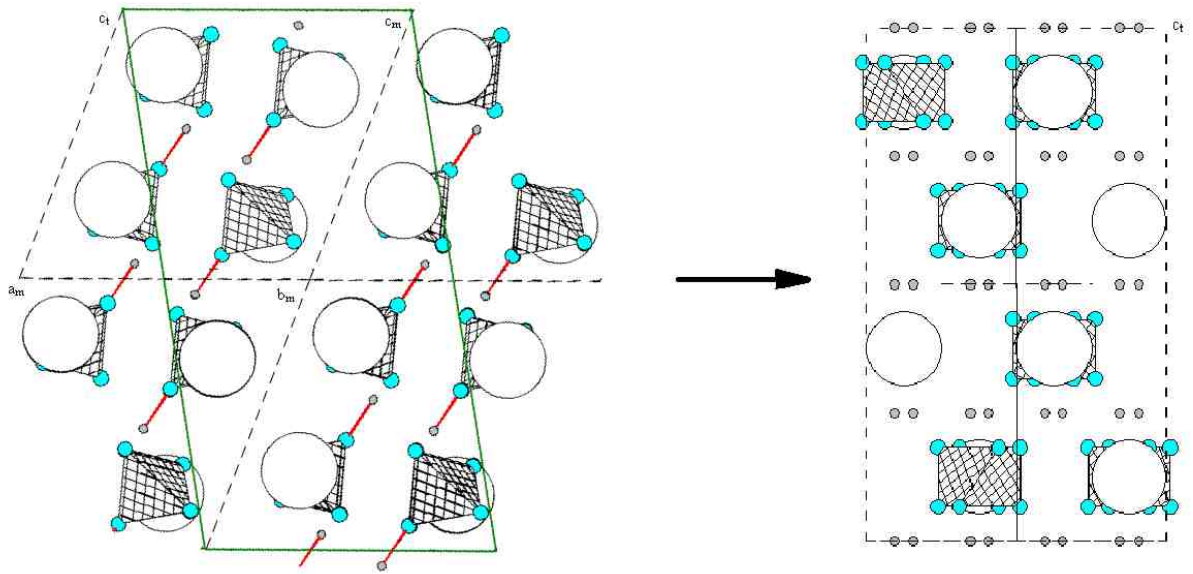
Figure 3-5 Structural changes throughout the phase transformation

(Pseudoorthorombic cell shown in dark green)

Both phase-II and phase-I can be written in the pseudoorthorombic basis as shown in **Figure 3-5**. We will use this notation in our derivations.

Lattice correspondence, which identifies the structural unit in the austenite that transforms into the martensite and a corresponding deformation, is necessary for successful creation of the transformation matrix. Domain pattern in the isostructural material, such as $CsHSeO_4$, studied in[9], allows us to choose and describe lattice correspondence, as proposed in[7].

We will use unit cell basis transformation suggested by[7*]

$a_t = 1/2*(a_m+b_m)$,

Equation 3-22

---

[*] Slight difference between Equation 3-24 in[7] and in[9] is due to different direction of the b_m-vector.

$b_t = 1/2 * (b_m - a_m),$

Equation 3-23

$c_t = a_m + 2 * c_m.$

Equation 3-24

With the chosen lattice vectors, we can write for:

Phase-II, CHS

$$a_o^m = a_m \begin{pmatrix} 1 \\ 0 \\ 0 \end{pmatrix} \quad b_0^m = b_m \begin{pmatrix} 0 \\ 1 \\ 0 \end{pmatrix} \quad c_0^m = \begin{pmatrix} a_m + 2 * \cos \beta * c_m \\ 0 \\ 2 * \sin \beta * c_m \end{pmatrix}.$$

Equation 3-25

Phase-I, CHS

$$a_o^t = a_t \begin{pmatrix} 1 \\ 1 \\ 0 \end{pmatrix} \quad b_0^t = b_t \begin{pmatrix} -1 \\ 1 \\ 0 \end{pmatrix} \quad c_0^t = c_t \begin{pmatrix} 0 \\ 0 \\ 1 \end{pmatrix}.$$

Equation 3-26

The non-symmetric transformation matrix T_1 will be equal:

$$\mathbf{T}_1 = \begin{pmatrix} \dfrac{a_m}{2 * a_t} & \dfrac{a_m}{2 * a_t} & \dfrac{a_m + 2 * \cos \beta * c_m}{c_t} \\ -\dfrac{b_m}{2 * b_t} & \dfrac{b_m}{2 * b_t} & 0 \\ 0 & 0 & 2 * \sin \beta * c_m \end{pmatrix}.$$

Equation 3-27

We derived the transformation matrix between two phases of CsHSO$_4$. Next step – find

how many variants are possible to form in our system.

$$N = \frac{\text{Austenite point group order}}{\text{Martensite point group order}},$$

Equation 3-28

N- number of possible variants.

The point group of the phase-I is 4/mmm and phase-II 2/m, predicted number of variants

is equal to **4**.

T_1 matrix is not symmetric. Following the procedure described above (Equation 3-2-

Equation 3-6) we can derive symmetric Bain matrix of the transformation (U_1) after

finding C= T^t*T .

$$C = \begin{pmatrix} \frac{(a_m)^2}{4*a_t^2} + \frac{(b_m)^2}{4*b_t^2} & \frac{(a_m)^2}{4*a_t^2} - \frac{(b_m)^2}{4*b_t^2} & 1/2*\frac{a_m*(a_m+2*\cos\beta*c_m)}{a_t*c_t} \\ \frac{(a_m)^2}{4*a_t^2} - \frac{(b_m)^2}{4*b_t^2} & \frac{(a_m)^2}{4*a_t^2} + \frac{(b_m)^2}{4*b_t^2} & 1/2*\frac{a_m*(a_m+2*\cos\beta*c_m)}{a_t*c_t} \\ 1/2*\frac{a_m*(a_m+2*\cos\beta*c_m)}{a_t*c_t} & 1/2*\frac{a_m*(a_m+2*\cos\beta*c_m)}{a_t*c_t} & \frac{(a_m+2*\cos\beta*c_m)^2}{c_t^2} + \frac{(2*\sin\beta*c_m)^2}{c_t^2} \end{pmatrix}$$

.

Equation 3-29

Matrix U_1 has a form of

$$U_1 = \begin{pmatrix} \alpha & \delta & \varepsilon \\ \delta & \alpha & \varepsilon \\ \varepsilon & \varepsilon & \gamma \end{pmatrix}.$$

Equation 3-30

Numerical expression for the terms in matrix U_1 will be shown in Chapter-4, after

we determine lattice parameters at the transformation temperatures. The symmetry of the

matrix U_1 is important to create other variant matrices, even though the exact expression

for matrix components will be provided later. Once U_1 is known, the other variants can be obtained by applying the rotations of the tetragonal austenite lattice to this matrix.

Matrices of four variants can be written as follows:

$$U_1 = \begin{pmatrix} \alpha & \delta & \varepsilon \\ \delta & \alpha & \varepsilon \\ \varepsilon & \varepsilon & \gamma \end{pmatrix} \qquad U_2 = \begin{pmatrix} \alpha & \delta & -\varepsilon \\ \delta & \alpha & -\varepsilon \\ -\varepsilon & -\varepsilon & \gamma \end{pmatrix}$$

$$U_3 = \begin{pmatrix} \alpha & -\delta & \varepsilon \\ -\delta & \alpha & -\varepsilon \\ \varepsilon & -\varepsilon & \gamma \end{pmatrix} \qquad U_4 = \begin{pmatrix} \alpha & -\delta & -\varepsilon \\ -\delta & \alpha & \varepsilon \\ -\varepsilon & \varepsilon & \gamma \end{pmatrix}.$$

Equation 3-31

3.2.2 $M_3H(XO_4)_2$ – monoclinic to hexagonal

The compound $Rb_3H(SeO_4)_2$ displays a sequence of phase transitions in 25-170^{0}C:

Phase-III (C2/c) →448K →possible Phase-II (C2/m) → 451K→ Phase I (R$\overline{3}$m)

where phase I, triclinic phase, is superprotonic in nature. The martensite – austenite transition was studied between phase III and phase I. Transformation between phase III and phase I was studied using diffraction and thermogravimetric techniques and extremely low hysteresis behavior was observed.[10]

Required lattice correspondence, which identifies the structural unit in the austenite that transforms into the martensite and a corresponding deformation was taken after studying the mechanism of the transformation. Transformation mechanism is known and just a minor reconfiguration of the selenate groups and rubidium atoms along c-axes[11]. Proper choice of the transformation unit cell was performed:

Monoclinic basis:

$$a_m^0 = a_m$$

$$b_m^0 = b_m$$

$$c_m^0 = 3*c_m - a_m$$

Equation 3-32
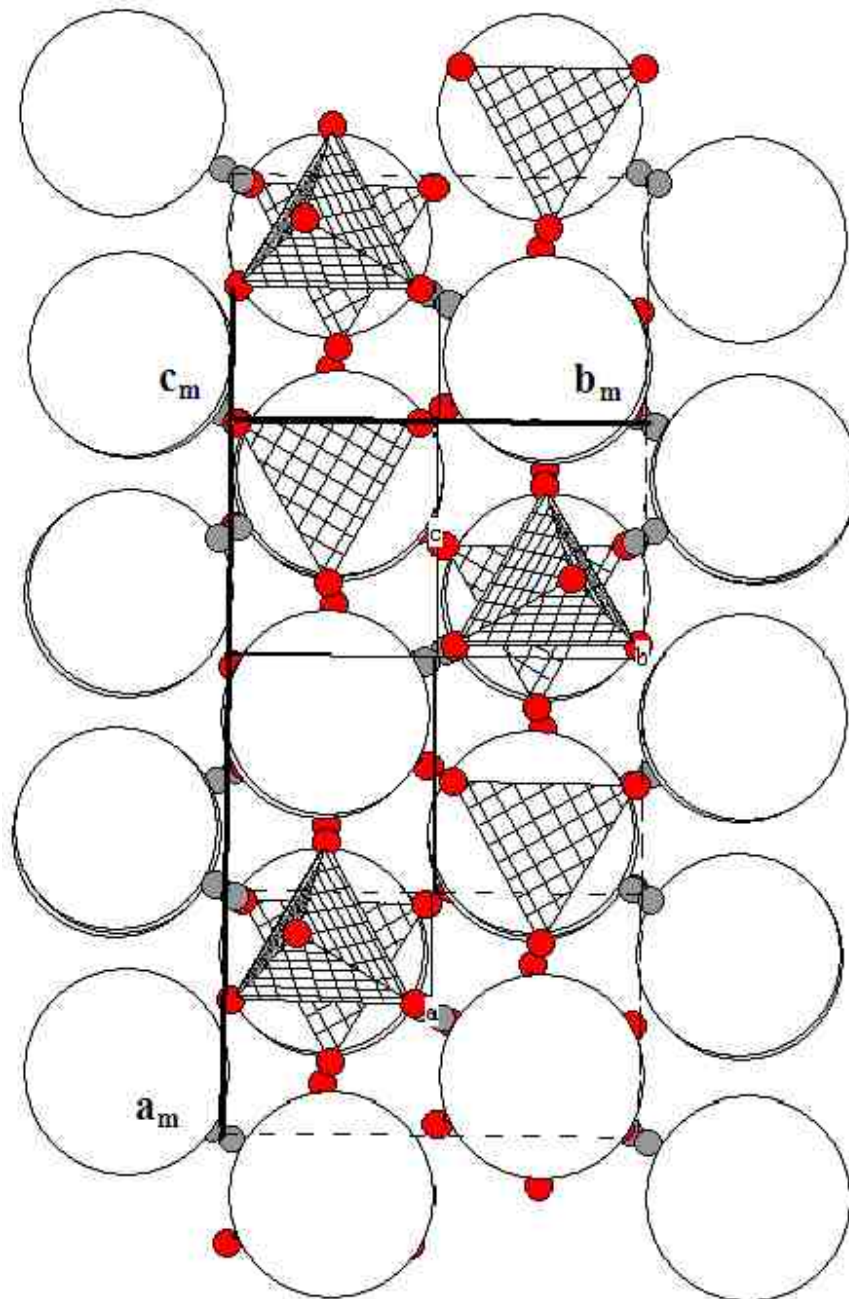
Figure 3-6. Monoclinic Rb₃H(SeO₄) choice of the unit cell, projection along [30-1] axes in low temperature phase
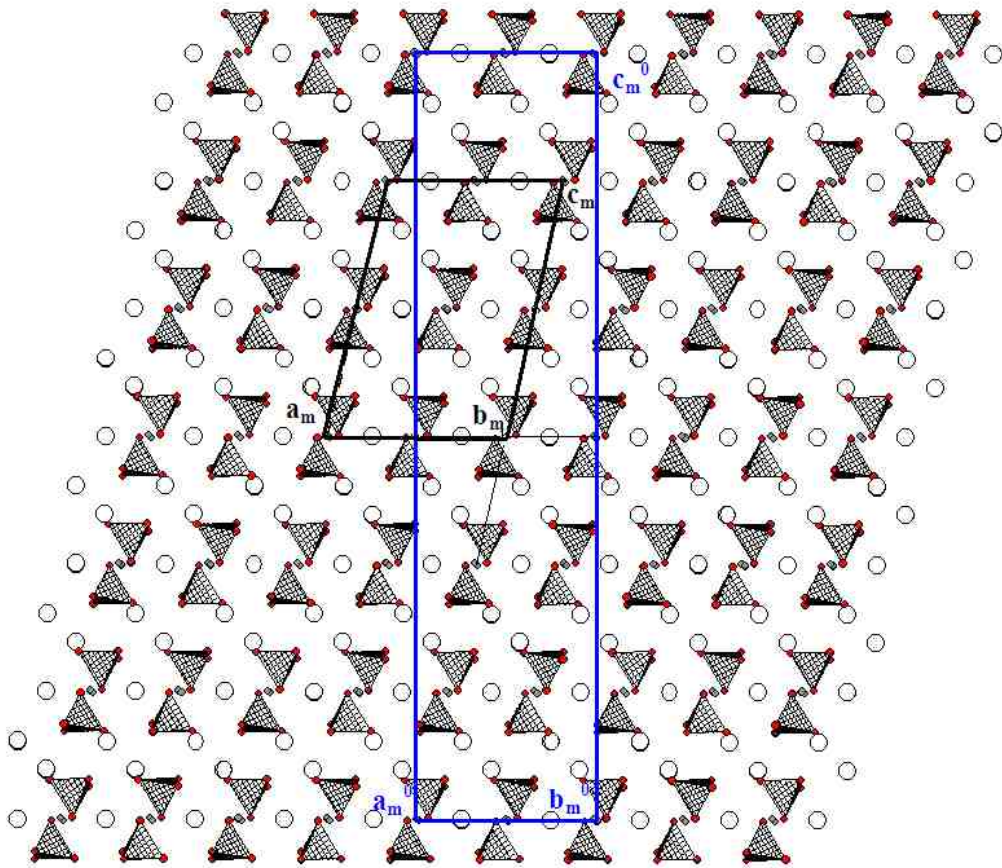
Figure 3-7. Monoclinic Rb$_3$H(SeO$_4$) choice of the unit cell projection along b$_m$

Original unit cell is shown in black, new unit cell in blue

Rhombohedral basis:

$$a_r = a_1 + a_2$$

$$b_r = a_1 - a_2$$

$$c_r = 2*c.$$
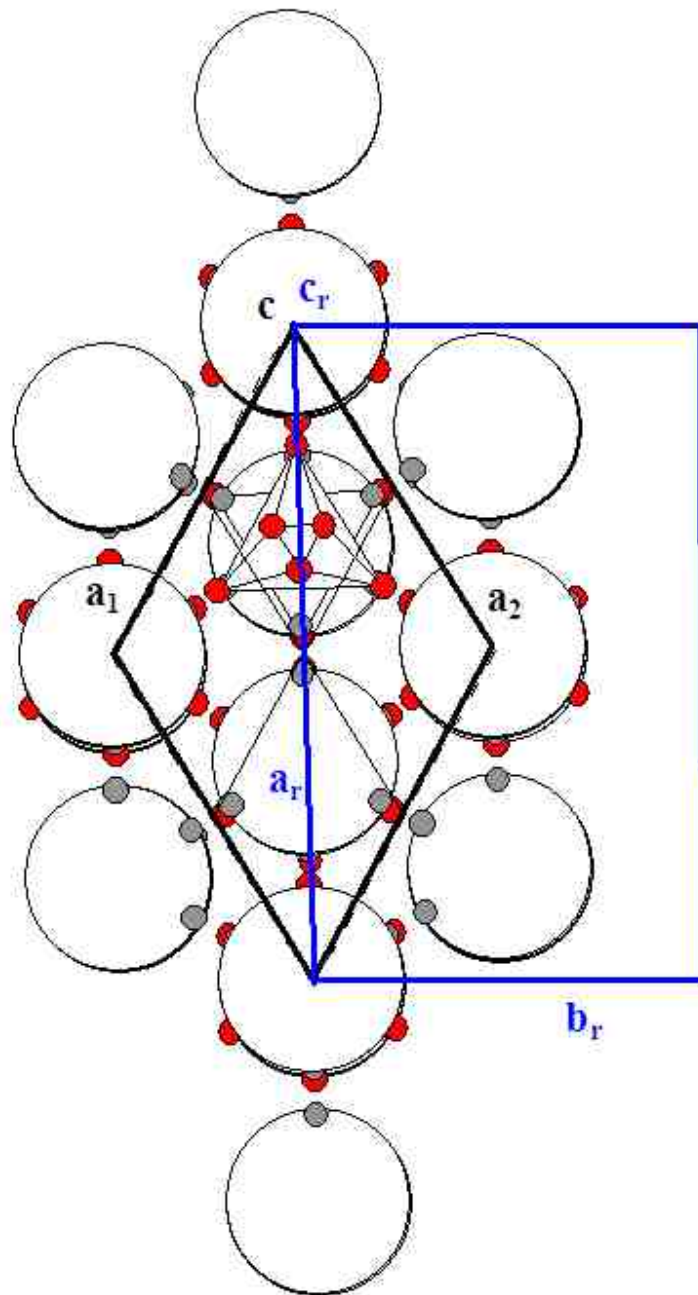
Figure 3-8. Projection along [001] in high temperature phase of the Rb$_3$H(SeO$_4$)

Different choice of the unit cell is required for high temperature phase (shown in

blue), to maintain same volume and same configuration

Equation 3-33

We can express chosen unit cell vectors from original unit cell vectors for low

temperature and high temperature phase, such as

Low temperature phase,

$$a_o^m = a_m \begin{pmatrix} 1 \\ 0 \\ 0 \end{pmatrix} \quad b_0^m = b_m \begin{pmatrix} 0 \\ 1 \\ 0 \end{pmatrix} \quad c_0^m = \begin{pmatrix} -a_m \\ 0 \\ 3*\sin\beta*c_m \end{pmatrix},$$

Equation 3-34

High temperature phase

$$a_o^r = \begin{pmatrix} \sqrt{3}a_1 \\ 0 \\ 0 \end{pmatrix} \quad b_0^r = \begin{pmatrix} 0 \\ a_1 \\ 0 \end{pmatrix} \quad c_0^r = \begin{pmatrix} 0 \\ 0 \\ 2*c \end{pmatrix}.$$

Equation 3-35

T_1 can be written as

$$\mathbf{T}_1 = \begin{pmatrix} \dfrac{\sqrt{3}*a_m}{3*a_1} & 0 & -\dfrac{a_m}{2*c} \\ 0 & \dfrac{b_m}{a_1} & 0 \\ 0 & 0 & \dfrac{3*\sin\beta*c_m}{2*c} \end{pmatrix}.$$

Equation 3-36

Based on the symmetry relationship, the number of variants can be found using Equation

3-1 and

$$\text{Number of variants} = 12/\,4 = 3$$

Following the T_1 symmetrization procedure, we will obtain C= T^t*T:

$$
C = \begin{pmatrix}
\dfrac{a_m^2}{3*a_1} & 0 & -\dfrac{a_m^2*\sqrt{3}}{6*a_1*c} \\[3mm]
0 & \left(\dfrac{b_m}{a_1}\right)^2 & 0 \\[3mm]
-\dfrac{a_m^2*\sqrt{3}}{6*a_1*c} & 0 & \dfrac{a_m^2}{4*c^2}+\dfrac{9*\sin^2\beta*c_m^2}{4*c^2}
\end{pmatrix}
$$

Equation 3-37

and three variants of the symmetric matrix U:

$$
U_1 = \begin{pmatrix}
\alpha & \delta & 0 \\
\delta & \varepsilon & 0 \\
0 & 0 & \gamma
\end{pmatrix},
$$

$$
U_2 = \begin{pmatrix}
0.25*\alpha+0.866*\delta+0.75*\mathrm{e} & -0.433*\alpha-0.5*\delta+0.433*\varepsilon & 0 \\
-0.433*\alpha-0.5*\delta+0.433*\varepsilon & 0.75*\alpha-0.866*\delta+0.25*\varepsilon & 0 \\
0 & 0 & \gamma
\end{pmatrix},
$$

$$
U_3 = \begin{pmatrix}
0.25*\alpha-0.866*\delta+0.75*\mathrm{e} & 0.433*\alpha-0.5*\delta-0.433*\varepsilon & 0 \\
0.433*\alpha-0.5*\delta-0.433*\varepsilon & 0.75*\alpha+0.866*\delta+0.25*\varepsilon & 0 \\
0 & 0 & \gamma
\end{pmatrix}.
$$

3.2.3 MH_2XO_4 – monoclinic to cubic

CsH_2PO_4 experiences the following phase transformations upon heating:

Monoclinic phase $(P2_1/m) \rightarrow \sim503\ K \rightarrow$ Cubic $(Pm\overline{3}m)$.
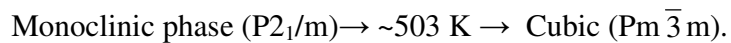
Transition occurs only under sufficient water partial pressure, otherwise dehydration occurs. Cubic phase is a superprotonic phase.

Theoretical treatment of the monoclinic-cubic transformation was developed by authors in [12], as well as in[13]. We will include the derivation for the completeness. It is also necessary to point out that the lattice parameters have to be calculated as close to the transition temperature as possible, while[12] uses room temperature data for the martensite

phase and austenite lattice parameters at temperatures higher than 230^0C. We will focus on determination of the correct lattice parameters for all three classes of the solid acids in Chapter 4. The results summary will be provided below, and transformation lattice formulas will be used with correct lattice parameters to predict transformation characteristics in Chapter 4.

Lattice correspondence was not studied for the monoclinic-cubic transformations, but transformation mechanism can be determined from crystal structure analysis alone. Only slight deformation of the structure will lead to the cubic symmetry. That strongly suggests the proposed basis vector relationship:

(a)

(b)
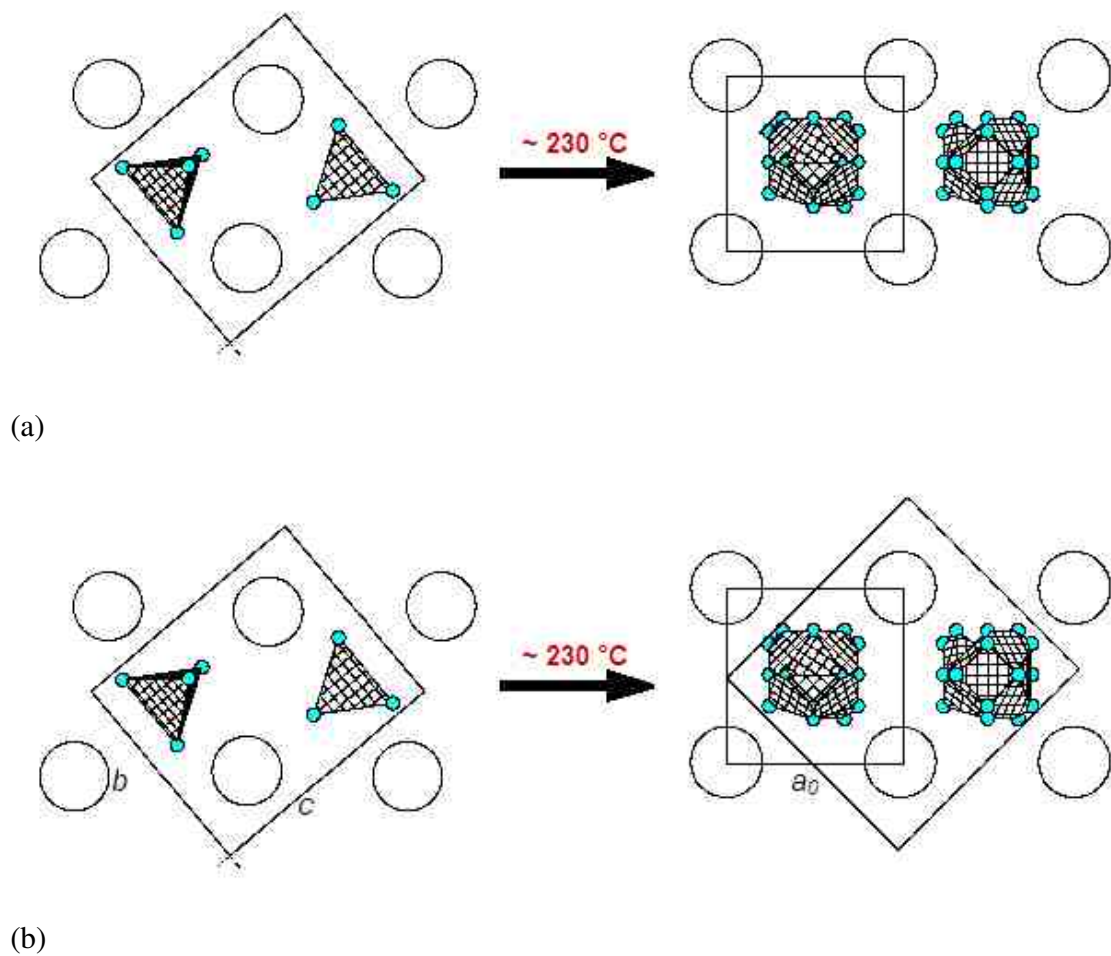
Figure 3-9 Structure relationship between low temperature (moclinic) and superprotonic high temperature (cubic) forms of CsH$_2$PO$_4$. (b) Choice of the same unit cell

Tetragonal unit cell was chosen to describe the cubic austenite phase, with the following relationship between unit cell vectors.

$$a_1^a = a_0 \begin{pmatrix} 0 \\ 1 \\ 1 \end{pmatrix} \qquad a_2^a = a_0 \begin{pmatrix} 0 \\ -1 \\ 1 \end{pmatrix} \qquad a_3^a = a_0 \begin{pmatrix} 1 \\ 0 \\ 0 \end{pmatrix}.$$

Equation 3-38 Choice of the lattice vectors for the cubic CsH$_2$PO$_4$

Figure 3-9 shows the selected tetragonal unit cell and corresponding monoclinic cell. Monoclinic lattice vectors can be written as

$$a_1^m = \frac{c}{\sqrt{2}} \begin{pmatrix} \sqrt{2}\cos\beta \\ \sin\beta \\ \sin\beta \end{pmatrix} \quad a_2^m = \frac{b}{\sqrt{2}} \begin{pmatrix} 0 \\ -1 \\ 1 \end{pmatrix} \quad a_3^m = a \begin{pmatrix} 1 \\ 0 \\ 0 \end{pmatrix}.$$

Equation 3-39 Choice of the lattice vectors for the monoclinic CsH$_2$PO$_4$

With the transformation matrix

$$\mathbf{T}_1 = \begin{pmatrix} \dfrac{a}{a_0} & \dfrac{c}{2a_0}\cos\beta & \dfrac{c}{2a_0}\cos\beta \\ 0 & \dfrac{c\sin\beta + b}{2a_0\sqrt{2}} & \dfrac{c\sin\beta - b}{2a_0\sqrt{2}} \\ 0 & \dfrac{c\sin\beta - b}{2a_0\sqrt{2}} & \dfrac{c\sin\beta + b}{2a_0\sqrt{2}} \end{pmatrix}.$$

Equation 3-40

The Bain matrix would be

$$\mathbf{U}_1 = \begin{pmatrix} \gamma & \varepsilon & \varepsilon \\ \varepsilon & \alpha & \delta \\ \varepsilon & \delta & \alpha \end{pmatrix}.$$

Equation 3-41

Number of variants in the case of monoclinic-cubic transformation will be N=24/2=12.

The list of variants was first derived by[12]:

$$
\mathbf{U}_1 = \begin{pmatrix} \gamma & \varepsilon & \varepsilon \\ \varepsilon & \alpha & \delta \\ \varepsilon & \delta & \alpha \end{pmatrix}
\mathbf{U}_2 = \begin{pmatrix} \gamma & -\varepsilon & -\varepsilon \\ -\varepsilon & \alpha & \delta \\ -\varepsilon & \delta & \alpha \end{pmatrix}
\mathbf{U}_3 = \begin{pmatrix} \gamma & -\varepsilon & \varepsilon \\ -\varepsilon & \alpha & -\delta \\ \varepsilon & -\delta & \alpha \end{pmatrix}
\mathbf{U}_4 = \begin{pmatrix} \gamma & \varepsilon & -\varepsilon \\ \varepsilon & \alpha & -\delta \\ -\varepsilon & -\delta & \alpha \end{pmatrix}
$$

$$
\mathbf{U}_5 = \begin{pmatrix} \alpha & \varepsilon & \delta \\ \varepsilon & \gamma & \varepsilon \\ \delta & \varepsilon & \alpha \end{pmatrix}
\mathbf{U}_6 = \begin{pmatrix} \alpha & -\varepsilon & \delta \\ -\varepsilon & \gamma & -\varepsilon \\ \delta & -\varepsilon & \alpha \end{pmatrix}
\mathbf{U}_7 = \begin{pmatrix} \alpha & -\varepsilon & -\delta \\ -\varepsilon & \gamma & \varepsilon \\ -\delta & \varepsilon & \alpha \end{pmatrix}
\mathbf{U}_8 = \begin{pmatrix} \alpha & \varepsilon & -\delta \\ \varepsilon & \gamma & -\varepsilon \\ -\delta & -\varepsilon & \alpha \end{pmatrix}
$$

$$
\mathbf{U}_9 = \begin{pmatrix} \alpha & \delta & \varepsilon \\ \delta & \alpha & \varepsilon \\ \varepsilon & \varepsilon & \gamma \end{pmatrix}
\mathbf{U}_{10} = \begin{pmatrix} \alpha & \delta & -\varepsilon \\ \delta & \alpha & -\varepsilon \\ -\varepsilon & -\varepsilon & \gamma \end{pmatrix}
\mathbf{U}_{11} = \begin{pmatrix} \alpha & -\delta & \varepsilon \\ -\delta & \alpha & -\varepsilon \\ \varepsilon & -\varepsilon & \gamma \end{pmatrix}
\mathbf{U}_{12} = \begin{pmatrix} \alpha & -\delta & -\varepsilon \\ -\delta & \alpha & \varepsilon \\ -\varepsilon & \varepsilon & \gamma \end{pmatrix}
$$

.

Equation 3-42 Different variants of the martensite

3.3 Conclusions

Analysis of the crystallography of the transformation mechanism allowed us to create transformation matrices. Crystallographic mathematical description of the transformation was shown in this Chapter. According to the symmetry relationship between phases the number of the possible variants is found. After we created transformation matrices for three classes of the solid acids, we need to utilize correct lattice parameters at the transformation. That will allow us to extract several important characteristics and allow us to determine which variants are compatible with each other and with the austenite phase. Middle eigenvalue could theoretically predict the properties hysteresis width.

References

[1]Cui, J., Y. S. Chu, et al. (2006). "Combinatorial search of thermoelastic shape-memory alloys with extremely small hysteresis width." <u>Nature Materials</u> **5**(4): 286-290.

[2] K. Bhattacharya, Microstructure of Martensite: Why It Forms and How It Gives Rise to the Shape-Memory Effect, Oxford University Press (2003).

[3]Bhattacharya, K., S. Conti, et al. (2004). "Crystal symmetry and the reversibility of martensitic transformations." <u>Nature</u> **428**(6978): 55-59.

[4]Bhattacharya, K. and R. D. James (2005). "The material is the machine." <u>Science</u> **307**(5706): 53-54.

[5] Ball, J. M. and R. D. James (1992). "Proposed Experimental Tests of a Theory of Fine Microstructure and the 2-Well Problem." <u>Philosophical Transactions of the Royal Society of London Series a-Mathematical Physical and Engineering Sciences</u> **338**(1650): 389-450.

[6] Ball, J. M. and R. D. James (1987). "Fine Phase Mixtures as Minimizers of Energy." <u>Archive for Rational Mechanics and Analysis</u> **100**(1): 13-52.

[7]Merinov, B. V., A. I. Baranov, et al. (1987). "Crystal-Structure of the Superionic Phase of Csdso4 and Phase-Transitions in Cesium Hydrosulfates and Deuterosulfates (Selenates)." <u>Kristallografiya</u> **32**(1): 86-92.

[8]Ibid.

[9] Yokota, S. (1982). "Ferroelastic Phase-Transition of Cshseo4." <u>Journal of the Physical Society of Japan</u> **51**(6): 1884-1891.

[10] Pawlowski, A., L. Szczesniak, et al. (2003). "Pretransitional effects at the superionic phase transition of Rb3H(SeO4)(2) protonic conductor." Solid State Ionics **157**(1-4): 203-208.

[11]Melzer, R., R. Sonntag, et al. (1996). "Rb3H(SeO4)(2) at 4K by neutron powder diffraction." Acta Crystallographica Section C-Crystal Structure Communications **52**: 1061-1063.

[12] Louie, M., D. Smirnova, M. Swaroop Martensitic transformations in cesium dihydrogen phosphate Micromechanics 260a, California Institute of Technology

[13] Louie, M.W., M. Kislitsyn, et al., (2009) "Phase transformation and hysteresis behavior in $Cs_{1-x}Rb_xH_2PO_4$" Solid State Ionics, doi:10.1016/j.ssi.2008.11.014

Chapter 4. Systems of interest for property-hysteresis study

a) Three classes of solid acids. (ex. $CsHSO_4$, CsH_2PO_4, $Rb_3H(SeO_4)_2$)

b) Isostructural solid solution series. (ex. $Cs_{1-x}Rb_xH_2PO_4$)

4.1 Three different classes of solid acids. ($CsHSO_4$, CsH_2PO_4, $Rb_3H(SeO_4)_2$) as a model system for hysteresis-crystallographic parameters study

New theoretical treatment of martensitic phase transitions was developed for three classes of the transformations in solid acids. The theory suggests that[1] it is not volume change but crystallographic compatibility between phases that determines transformation properties (such as hysteresis) during the transformation between phases. We'll test that hypothesis on experimental study for three different types of solid acids.

4.1.1 Determine lattice parameters in $CsHSO_4$ from 25 to 140^0C

High temperature X-ray diffraction technique was used to determine lattice parameters of $CsHSO_4$ at different temperatures. Heating rate was 1^0C/min and X-ray diffraction patterns were taken with the increment $5-10^0C$ on heating and on cooling (see Table 4-1 for details) for 10 to 70 degrees 2 theta.

Table 4-1 List of temperatures the diffraction patterns were collected at for pure $CsHSO_4$

Heating	50^0C	80^0C	130^0C	155^0C
30^0C	55^0C	90^0C	135^0C	160^0C
35^0C	60^0C	100^0C	140^0C	165^0C

40^{0}C	65^{0}C	110 h	145^{0}C	
45^{0}C	70^{0}C	120^{0}C	150^{0}C	

Cooling	60^{0}C	110^{0}C	160^{0}C
25^{0}C	70^{0}C	120^{0}C	
30^{0}C	80^{0}C	130^{0}C	
40^{0}C	90^{0}C	140^{0}C	
50^{0}C	100^{0}C	150^{0}C	

To ensure precise temperature control, temperature calibration was performed before the experiment. Diffraction patterns were analyzed and refined using the Rietveld refinement technique.

Rietveld refinement was performed using X'Pert Plus software package. The structures reported by Chisholm[2] and by Itoh[3] for phases II and III, respectively, were used as starting models. The following parameters were refined for all phases:

- Lattice constants, scale factors

- Overall isotropic atomic displacement parameter and site occupancies

- Peak profiles, $\Gamma = (W + U*\tan^2\theta + V*\tan\theta)^{1/2}$ (3 refined parameters per phase)

- 6 background parameters and zero shift parameter

The quality of the refinement can be seen in the examples for three different temperatures and phases of $CsHSO_4$ (see Figure 4-1-Figure 4-3) and the summary is shown in Table 4-2.
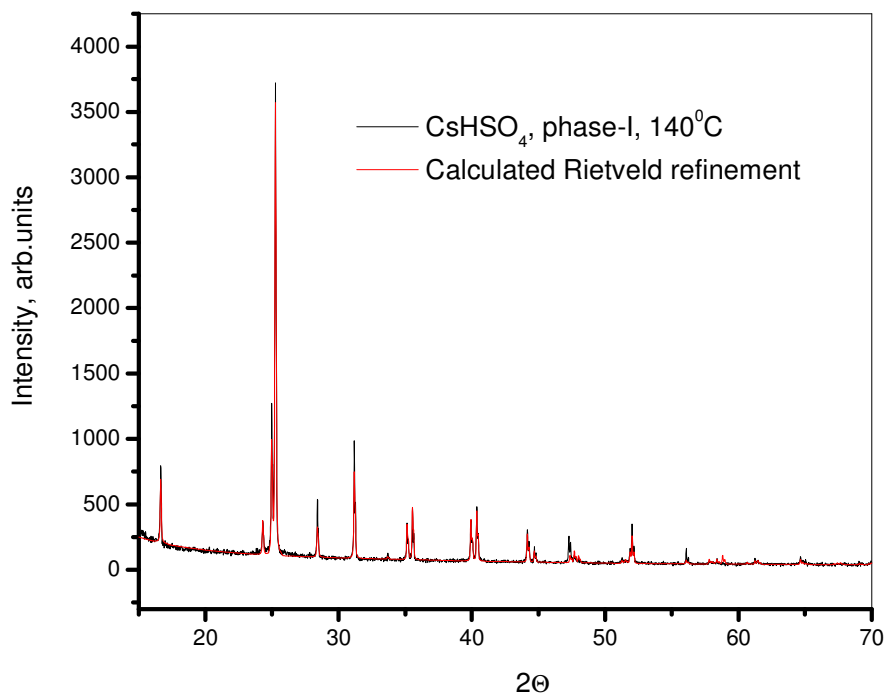
Figure 4-1 Measured and calculated from Rietveld refinement X-ray diffraction

patterns of CsHSO$_4$, phase-I, T=140^{0}C taken on cooling
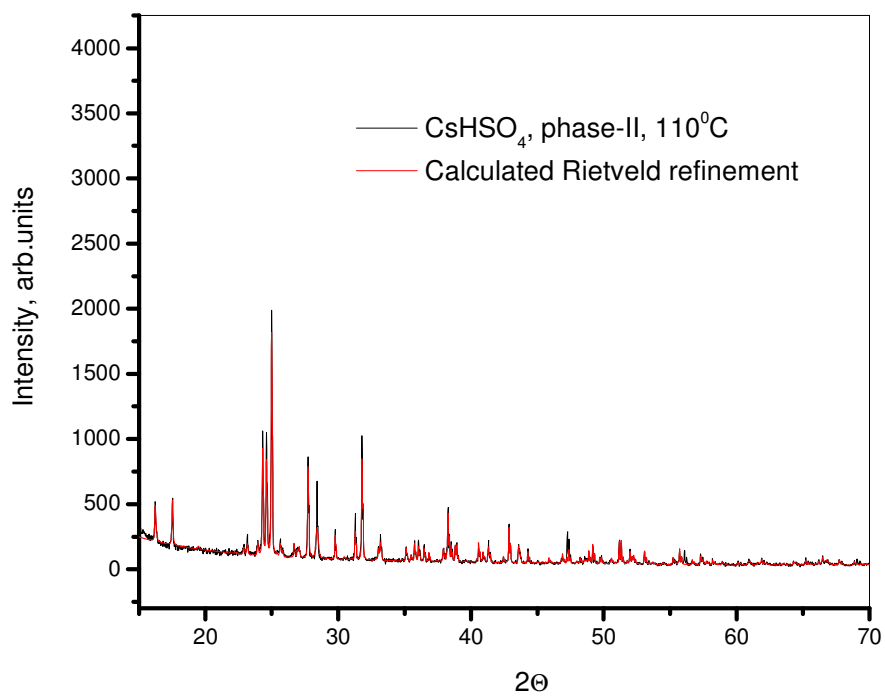
Figure 4-2 Measured and calculated from Rietveld refinement X-ray diffraction patterns of CsHSO$_4$, phase-II, T=110^{0}C
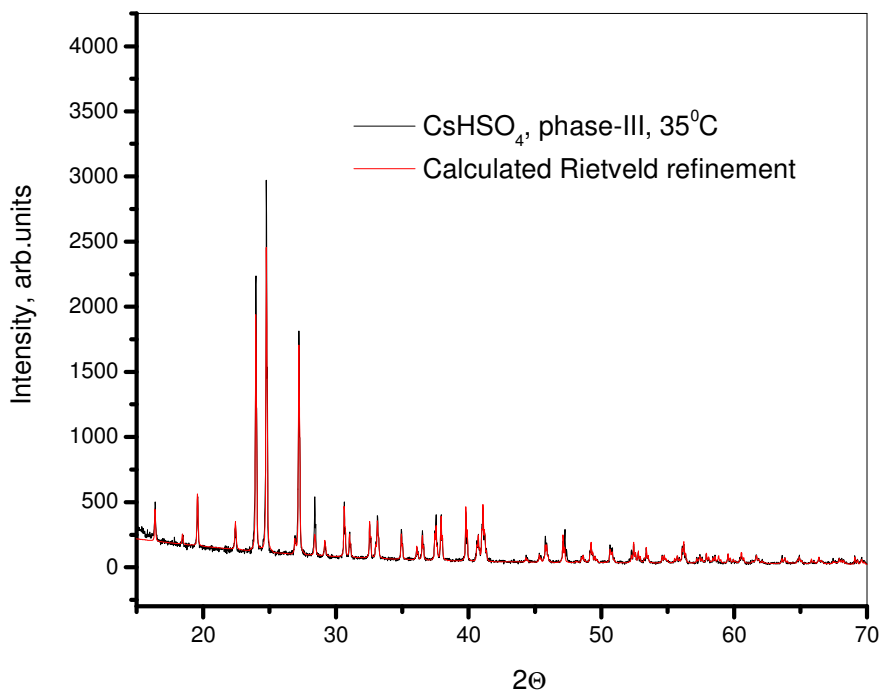
Figure 4-3 Measured and calculated from Rietveld refinement X-ray diffraction patterns of CsHSO₄, phase-III, T=35⁰C

Table 4-2 Rietveld refinement parameters for CsHSO₄ at different temperatures

Heating	R (expected) / %	R (profile)/ %	R (weight. profile)/ %	Cooling	R (expected)/ %	R (profile)/ %	R (weight. profile)/ %%
30⁰C	9.626	11.532	15.25	25⁰C	9.77	10.701	14.504
35⁰C	9.627	11.533	15.13	30⁰C	9.753	10.853	14.711
40⁰C	9.624	11.322	15.135	40⁰C	9.771	9.793	13.362
45⁰C	9.647	11.613	15.418	50⁰C	9.803	9.752	13.412
50⁰C	9.649	11.471	15.292	60⁰C	9.802	9.674	13.289
55⁰C	9.643	11.417	15.429	70⁰C	9.82	10.056	13.634
60⁰C	9.656	11.676	15.717	80⁰C	9.81	9.839	13.387
65⁰C	9.659	11.509	15.355	90⁰C	9.828	10.134	13.64
70⁰C	9.653	11.679	15.724	100⁰C	9.824	10.097	13.69
80⁰C	9.683	11.603	15.548	110⁰C	9.85	11.2	14.988

4-6

90^{0}C	9.723	11.943	15.975	**120^{0}C**	9.832	10.674	14.531
100^{0}C	9.929	12.065	16.099	**130^{0}C**	9.827	10.525	14.248
110^{0}C	9.917	11.66	15.628	**140^{0}C**	9.829	10.775	14.451
120^{0}C	9.96	11.779	16.101	**150^{0}C**	9.863	11.616	15.398
130^{0}C	9.908	11.499	15.617	**160^{0}C**	9.839	11.56	15.291
135^{0}C	9.837	11.25	15.11				
140^{0}C	9.825	10.416	14.075				
145^{0}C	9.829	10.782	14.604				
150^{0}C	9.835	10.723	14.304				
155^{0}C	9.833	10.797	14.483				
160^{0}C	9.826	10.686	14.463				
165^{0}C	9.845	11.687	15.47				

Information necessary for applying martensite-austenite theory to the solid acids consists of two parts:

1. Volume change during the transformation

2. Lattice parameters at the transformation temperatures.

Both quantities are extractable from the refinement. Unit cell volume dependence is shown in Figure 4-4, lattice parameter dependence on temperature is shown in Figure 4-5. We were able to obtain CsHSO$_4$ lattice parameters below 141^{0}C in the metastable region. That allowed us to have lattice parameters for both phases at the same temperature, while one is taken on heating and the other on cooling.
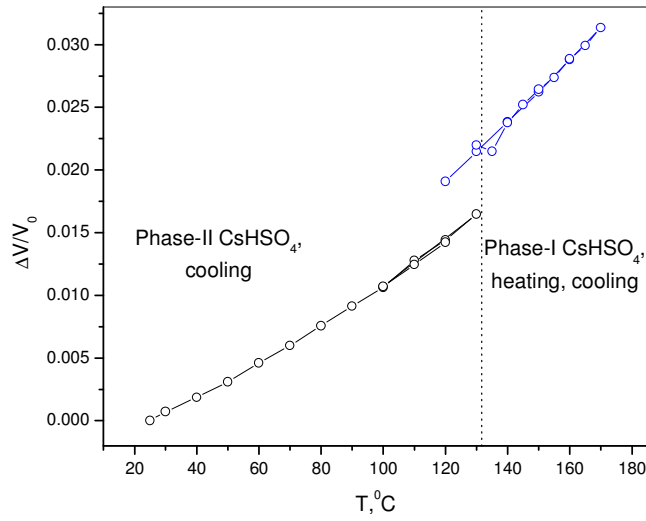
Figure 4-4 Relative volume change of the CsHSO₄ during phase-II to phase-I

transformation
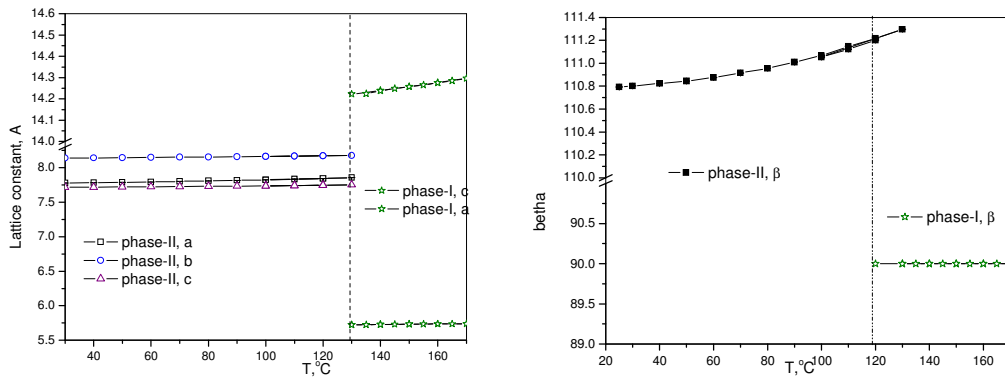
Figure 4-5 Lattice parameters (a,b,c, β for phase-II and a,c, β for phase-I) as a

function of the temperature

The temperature of 130^0C was chosen for austenite-martensite analysis because of

the lattice parameters availability for both phase-I and phase-II CsHSO₄ at that

temperature. The following lattice parameters were used:

<u>Monoclinic phase-II CsHSO$_4$</u>   <u>Tetragonal phase-I CsHSO$_4$</u>

<u>At 130 °C</u>   <u>At 130 °C</u>

$a = 7.8558(4)$ Å $a = 5.7249(4)$ Å

$b = 8.1749(4)$ Å $c = 14.2223(7)$ Å

$c = 7.7522(4)$ Å $V = 466.126$ Å^3

$\beta = 111.2970(2)$

$V = 463.847$ Å^3

Using the same pseudoorthorombic unit cell for both high and low temperature phase, we can write the lattice parameters as follow:

Table 4-3.Lattice parameters in the same orthorhombic basis:

PseudoOrthorombic			
Phase-II, (T=130^{0}C)		Phase-I (T=130^{0}C,)	
a	7.8558(4)	a	8.0962(6)
b	8.1749(4)	b	8.0962(6)
c	14.6158(8)	c	14.2223(7)
β	98.754(2)	β	90

With the symmetric transformation matrix being equal:

$$U_1 = \begin{pmatrix} 0.98851 & -0.021204 & 0.053870 \\ -0.021204 & 0.98851 & 0.053870 \\ 0.053870 & 0.053870 & 1.0248 \end{pmatrix}.$$

Equation 4-1 CsHSO$_4$ symmetric transformation matrix

Which can also be written as

$$U_1 = \begin{pmatrix} \alpha & \delta & \varepsilon \\ \delta & \alpha & \varepsilon \\ \varepsilon & \varepsilon & \gamma \end{pmatrix}.$$

Equation 4-2 CsHSO$_4$ symmetric transformation matrix in symbolic notation.

4.1.2 Determine lattice parameters in CsH$_2$PO$_4$ from 25 to 250^{0}C

The same approach was used for CsH$_2$PO$_4$. High temperature diffraction patterns were recorded at the same conditions (1^0/min heating rate), but only on heating. Since CsH$_2$PO$_4$ is known to decompose under ambient conditions upon heating, additional preparation procedures were used to avoid it. Only high quality CsH$_2$PO$_4$ powders were used and less scans on heating and cooling were performed as well as smaller 2 theta range (10-60), to decrease the experiment time. We were able to obtain impurities-free diffraction patterns of the low and high temperature phases of the CsH$_2$PO$_4$.
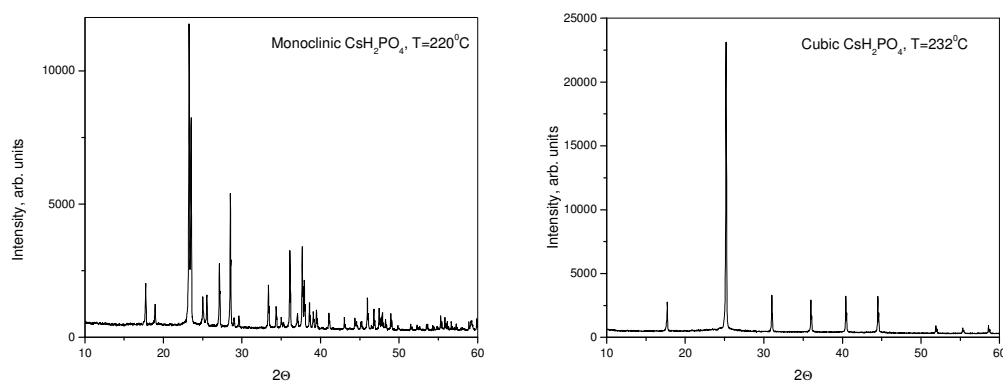
Figure 4-6 Diffraction patterns of the Monoclinic CsH$_2$PO$_4$ (left) and Cubic CsH$_2$PO$_4$ (right) at 220 and 232^{0}C

Relative volume change upon heating can be seen in Figure 4-7.
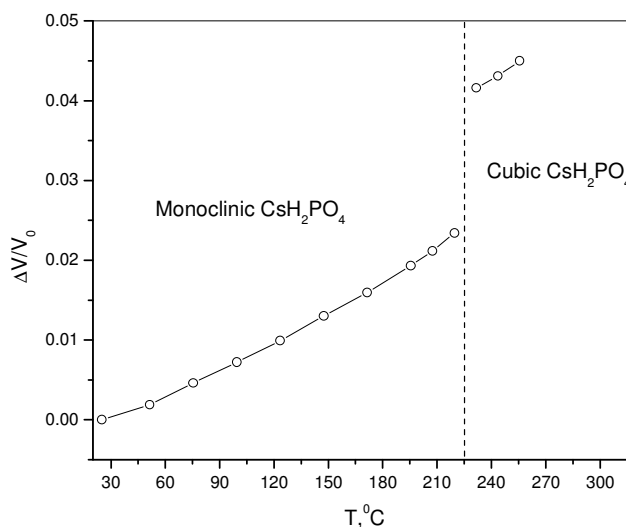
Figure 4-7 Relative volume change of the CsH_2PO_4 during monoclinic to cubic transition

Lattice parameters temperature dependence was determined based on Rietveld refinement using X'Pert Plus software package. The structures reported by Ueso[4] and by Yamada[5] for low and high temperature, respectively, were used as starting models. The following parameters were refined for all phases:

- Lattice constants, scale factors,

- Overall isotropic atomic displacement parameter and site occupancies.

- Peak profiles, $\Gamma = (W + U*\tan^2\theta + V*\tan\theta)^{1/2}$ (3 refined parameters per phase)

- Asymmetry, peak shape and preferred orientation (3 parameters total)

- 6 background parameters and zero shift parameter

Summary of the refinement is provided in Table 4-4.

Table 4-4 Summary of the Rietveld refinement of the CsH_2PO_4 at 25 to 250^0C.

Heating	R	R	R

	(expected) / %	(profile)/ %	(weight. profile)/ %
25.0⁰C	4.298	9.782	13.927
51.4⁰C	4.325	10.029	14.41
75.4⁰C	4.379	10.919	16.059
99.4⁰C	4.311	10.324	14.706
123.5⁰C	4.413	9.821	13.747
147.5⁰C	4.357	10.616	15.418
171.5⁰C	4.335	10.428	14.963
195.5⁰C	4.394	9.648	14.001
207.5⁰C	4.345	9.391	12.970
219.5⁰C	4.354	9.583	13.818
231.5⁰C	4.277	7.358	**9.837**
243.5⁰C	4.291	6.518	**8.845**
255.6⁰C	**4.897**	**7.251**	**9.313**
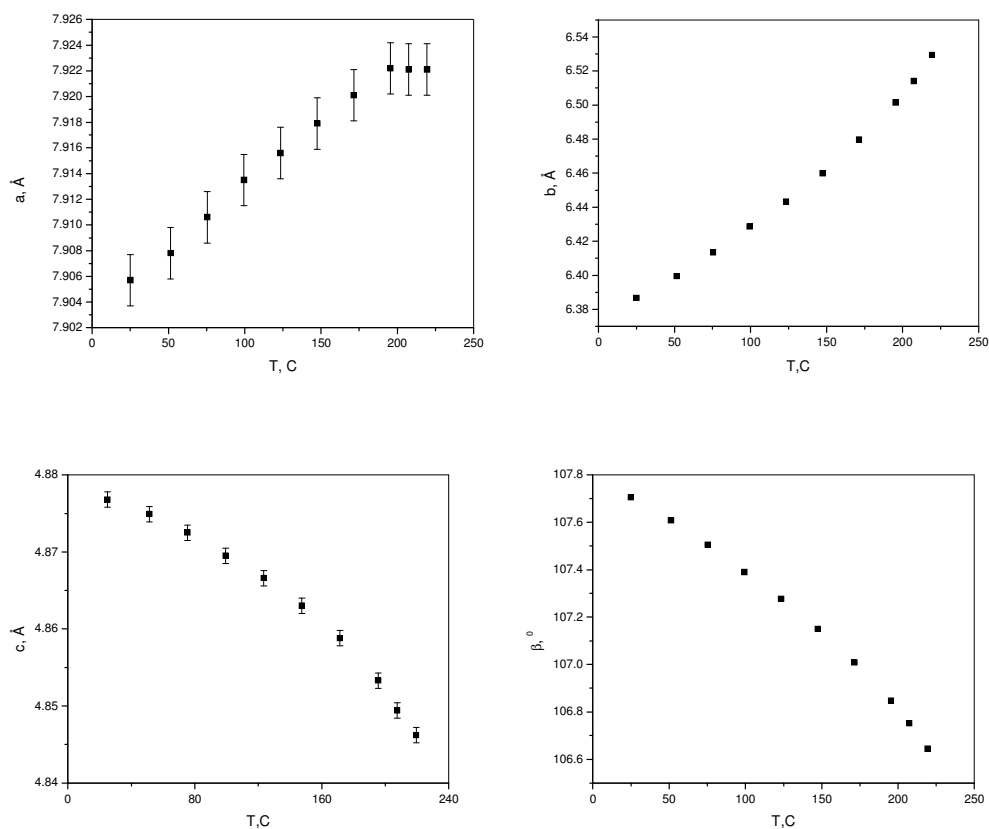
Figure 4-8 Monoclinic CsH₂PO₄ lattice parameters temperature dependence

Monoclinic phase CsH_2PO_4	Cubic phase CsH_2PO_4
At 220 °C	At 232 °C
$a = 7.921(2)$ Å	$a_o = 4.9628(1)$ Å
$b = 6.530(2)$ Å	$V = 122.231$ Å^3
$c = 4.847(1)$ Å	
$\beta = 106.642(9)$ °	
$V = 240.19$ Å^3	

The transformation temperature of CsH_2PO_4 is known to be 228^0C and we need to extrapolate our values of the lattice parameters and cell volume to that temperature to have data as accurate as possible. We weren't able to experimentally measure the lattice parameters at the same temperature. Anisotropic thermal expansions for each lattice parameters were found for monoclinic and cubic phase. Results are shown in Table 4-5.

Table 4-5 Thermal expansion parameters for CsH_2PO_4 for the form:

$\Delta a/a0 = A(T-T_0) + B(T-T_0)^2$, where $T_0 = 25.0$°C

Relative thermal expansion	$Ax10^{-4}/K^{-1}$	$Bx10^{-7}/K^{-1}$	$T_{meas}/°C$
$\Delta a/a_0$	−0.102(13)	−1.10(8)	25–220
$\Delta b/b_0$	0.662(30)	2.38(18)	25–220
$\Delta c/c_0$	0.145(8)	−0.167(50)	25–220
$\Delta\beta/\beta_0$	−0.303(11)	−1.00(7)	25–220
$\Delta V/V_0$ (monoclinic)	0.804(23)	1.99(14)	25–220
$\Delta V/V_0$ (cubic)	1.98(2)	0	232–256

*For the cubic phase, relative volumetric thermal expansion is taken to be linear with temperature.

Final lattice parameters at the transformation temperature (228^0C) will be

Monoclinic phase CsH_2PO_4 Cubic phase CsH_2PO_4

At 228 °C   At 228 °C

$a = 7.9221(1)$ Å $a_o = 4.9620(1)$ Å

$b = 6.5401(2)$ Å

$c = 4.8450(2)$ Å

$\beta = 106.604(9)$ °

$V = 240.559(1)$ Å^3

Using these lattice parameters, symmetric transformation matrix can be written as

$$U_1 = \begin{pmatrix} 0.9646 & -0.1069 & -0.1069 \\ -0.1069 & 1.0254 & 0 \\ -0.1069 & 0.09339 & 1.0254 \end{pmatrix}.$$

Equation 4-3

4.1.3 Extract lattice parameters from literature single crystal data for $Rb_3H(SeO_4)_2$ from 25 to 150^{0}C

$Rb_3H(SeO_4)_2$ has been a model system on superprotonic phase transformations since its discovery. There is a large block of literature on crystal structures and lattice parameters. One of the unique properties of that material is a decrease in volume when going into the superprotonic phase[6].

Trirubidium selenate exists at monoclinic phase from 4K to around 448-451K, superprotonic phase is stable above 451K. It is also suggested[7],[8],[9],[10] that intermediate phase exists in 448-451K. The crystal forms dense networks of domains around 448-451K, that makes structure refinement of the intermediate phase more challenging. It was

proposed that the structure remain monoclinic and lattice parameters were found[7]. The interest of the research community to that narrow temperature range has a huge benefit to us, since reliable lattice parameters right before and after transformation were determined by several groups.

We used four literature sources - two low temperature structure information ($0K^{11}$ and $300K^{12}$), one intermediate (450 K) crystal diffraction[7] and high temperature single crystal diffraction[13] for transformation matrix determination. Table 4-6 illustrates unit cell volume for different phases of the $Rb_3H(SeO_4)_2$.

Table 4-6. Unit cell volumes for three phases of the $Rb_3H(SeO_4)_2$

Stuctures		Volume	Volume, Z=1
Low temperature (monoclinic) structure, T=300 K	Z=4	958.6903	**239.67**
Intermediate (monoclinic) structure, T=450 K	Z=2	503.6	**251.80**
High temperature (trigonal) structure, T=470 K	Z=3	735.8205	**245.27**

After recalculating lattice parameters to the same basis, we have:

Room temperature phase, (T=4 K)

a= 10.38719(8) A,

b=6.03925(2) A,

c=15.29563(7) A

β= 102.8250(4)

V=233.89 A^3/Z,

Intermediate temperature (T=450 K)   High temperature (T=470 K)

(in LT unit cell)   a=6.125(1) A

a= 10.691(3) A,   c=22.6480(20) A

b=6.167(2) A,   V= 245.27(2) A^3/Z

c*sin(b)=15.279 A

V=251.8 A^3/Z

Taking into account that the transformation matrix is

$$\mathbf{T}_1 = \begin{pmatrix} \dfrac{\sqrt{3}*a_m}{3*a_1} & 0 & -\dfrac{a_m}{2*c} \\[2ex] 0 & \dfrac{b_m}{a_1} & 0 \\[2ex] 0 & 0 & \dfrac{3*\sin\beta*c_m}{2*c} \end{pmatrix}.$$

Equation 4-4

The symmetric transformation matrix will be equal

$$U_1 = \begin{pmatrix} 1.0009 & -0.1170 & 0 \\ -0.1170 & 1.0325 & 0 \\ 0 & 0 & 1.006857 \end{pmatrix}.$$

Equation 4-5

This can also be written as

$$U_1 = \begin{pmatrix} \alpha & \delta & 0 \\ \delta & \varepsilon & 0 \\ 0 & 0 & \gamma \end{pmatrix}.$$

Equation 4-6

4.2 Transformation parameters from the austenite-martensite transformation theory applied to three classes of the solid acids

a) Monoclinic – Tetragonal transformation in CsHSO₄

Analyzing any of the variants' matrices we can obtain determinant, which corresponds to the volume change during transformation.

$$\text{Det}(U_i) - 1 = -0.0049357;$$

Eigenvalues of the transformation matrix were found to be:

$$\{0.914626, \quad \textbf{1.00971}, \quad 1.07748\}$$

We can see that middle eigenvalue is very close to 1.

For the case of CsHSO₄ monoclinic to tetragonal transformation, the variant pairs that can form twins form a two-fold rotation. Variants pairs $U_1 - U_2$, $U_1 - U_3$, $U_1 - U_4$, $U_2 - U_3$, $U_2 - U_4$, and $U_3 - U_4$ form compound twins. The twinning modes are summarized in Table 4-7, where Y indicates a pair of variants capable of forming a twin boundary, N indicates that a pair of twins cannot form a twin boundary, and C indicates a compound twin.

Table 4-7. Possible twin formation table

	1	2	3	4
1		Y	Y	Y
2	Y		Y	Y
3	Y	Y		
4	Y	Y	Y	Y

Possible twin pair and their volume fractions

For each allowable variant pair, two types of twins can form, each of which has four possible solutions for the austenite-martensite interface. Therefore, there are up to **eight** solutions expected for any given variant pair.

1. Pairs comparable between each other.

Variant pair	Eigenvalues	2-fold rotation axes
U_1 --- U_2,	{0.735801,1,1.35906}	(0,0,1); (1/√2, 1/√2,0)
U_1 --- U_3	{0.790133,1,1.26561}	(0,1,0)
U_1 --- U_4	{0.790133,1,1.26561}	(1,0,0)
U_2 --- U_3	{0.790133,1,1.26561}	(1,0,0)
U_2 --- U_4	{0.790133,1,1.26561}	(0,1,0)
U_3 --- U_4	{0.735801,1,1.35906}	(0,0,1); (1/√2,-1/√2,0)

2. Pairs comparable between each other AND austenite.

1. U_1-U_3,

2. U_1-U_4,

3. U_2-U_3,

4. U_2-U_4

For cases U_1-U_3, U_1-U_4, U_2-U_3, U_2-U_4 all **eight** possible interfaces are allowed. Interface normal vector and volume fractions are shown in Table 4-8.

Table 4-8. U_1-U_3 possible interfaces and volume fraction

	b	**m**	Twin vol.

			fraction
1.	b= {-0.112755,-0.0798422,-0.0190051}	m= {{0.087109},{0.172353},{-0.981176}}	0.165588
2.	b= {-0.0199517,-0.0294866,0.134841}	m= {{0.802455},{0.560503},{0.2047}}	0.165588
3.	b= {0.0199517,-0.0294866,-0.134841}	m= {{-0.802455},{0.560503},{-0.2047}}	0.834412
4.	b= {0.112755,-0.0798422,0.0190051}	m= {{-0.087109},{0.172353},{0.981176}}	0.834412
5.	b= {-0.11485,-0.068162,-0.0155714}	m= {{0.0899978},{0.145836},{-0.985207}}	0.209801
6.	b= {-0.0197666,-0.0240995,0.130796}	m= {{0.848294},{0.497236},{0.18208}}	0.209801
7.	b= {0.0197666,-0.0240995,-0.130796}	m= {{-0.848294},{0.497236},{-0.18208}}	0.790199
8.	b= {0.11485,-0.068162,0.0155714}	m= {{-0.0899978},{0.145836},{0.985207}}	0.790199

The theory of martensitic transformations is applied to the solid acid material $CsHSO_4$, for the first time, to determine the possible austenite-martensite interfaces that can be formed. Four variants of the austenite phase exist for the tetragonal to monoclinic transition that occurs in $CsHSO_4$ upon cooling below ~141°C. Six variant pairs can form twins, 4 of which can form austenite-martensite interfaces. From these 4 variant pairs, it is calculated that there are 32 austenite-martensite interfaces for the $CsHSO_4$ phase transformation.

b) Monoclinic – Cubic transformation in CsH_2PO_4

Performing the same analysis as above, we can find transformation matrix determinant (which corresponds to the volume change during transformation)

$$Det(U_i) - 1 = -0.015488;$$

and eigenvalues:

{0.872008,   **0.931993**   ,1.2114}.

1. Martensite pairs comparable between each other AND austenite.

U_1-U_3, U_1-U_4 U_1-U_5 U_1-U_9 U_2-U_3, U_2-U_4, U_2-U_7, U_2-U_{12} U_3-U_6, U_3-U_{11}, U_4-U_8, U_4-U_{10}, U_5-U_7, U_5-U_8, U_5-U_9, U_6-U_7, U_6-U_8, U_6-U_{11}, U_7-U_{12}, U_8-U_{10}, U_9-U_{11}, U_9-U_{12}, U_{10}-U_{11}, U_{10}-U_{12}.

Qualitative details of the calculations are identical to[14], although actual transformation parameters and vectors are quite different, since we use precise lattice parameters.

Calculation to determine how many possible austenite-martensite interfaces that can form was performed and a mechanism of transformation was proposed. Twelve variants of the austenite phase can exist for the cubic to monoclinic transition that occurs in CsH_2PO_4. upon cooling below ~ 230ºC. Forty-two variant pairs can form twins, 24 of which can form austenite-martensite interfaces. From these 24 variant pairs (listed above), it is found that there are 96 austenite-martensite interfaces for the CsH_2PO_4 phase transformation.

c) Monoclinic-Trigonal transformation in $Rb_3H(SeO_4)_2$.

Transformation matrix analysis gives us matrix determinant (which corresponds to the volume change during transformation).

$$\mathbf{Det(U_i) - 1 = \ 0.0267;}$$

Since the rotation is on 120^0C, we can write three other variants.

$$U_1 = \begin{pmatrix} 1.0009 & -0.1170 & 0 \\ -0.1170 & 1.0325 & 0 \\ 0 & 0 & 1.006857 \end{pmatrix}$$

$$U_2 = \begin{pmatrix} 0.9233 & 0.0721 & 0 \\ 0.0721 & 1.1101 & 0 \\ 0 & 0 & 1.006857 \end{pmatrix}$$

$$U_3 = \begin{pmatrix} 1.1259 & 0.0448 & 0 \\ 0.0448 & 0.9075 & 0 \\ 0 & 0 & 1.006857 \end{pmatrix}$$

Corresponding eigenvalues will be:

$$\{0.89867, \quad \mathbf{1.006857}, \quad 1.1347\}.$$

4.3 Comparison of the transformation parameters to the hysteresis width and conclusions for three different classes of the solid acids.

According to the austenite-martensite theory, middle eigenvalue (λ_2) of the transformation matrix is especially important. If $\lambda_2=1$, stress-free interface of a single variant of the martensite forms strain-free interface with the austenite. When λ_2 is not one, the combination of several martensite can still form strain-free interface with the austenite. It was suggested, that the further λ_2 is from one, larger hysteresis may be observed. Three studied classes of the solid acids are good examples to test the hypothesis of the hysteresis width being independent from relative volume change during the transformation.

Table 4-9 Summary of the transformation parameters for three classes of the solid acids

Class of the	Volume	Middle	Measured

Solid Acids	change*, %	eigenvalue	Hysteresis[**], ^{0}C
Monoclinic-Tetragonal ($CsHSO_4$)	**0.49**	**1.00971**	**5.2**
Monoclinic-Cubic (CsH_2PO_4)	**1.55**	**0.931993**	**13.4**
Monoclinic-Trigonal ($Rb_3H(SeO_4)_2$)	**-2.67**	**1.006857**	**2**

* Positive values mean expansion upon transition from low to high temperature phase, negative- contraction.
** Literature data.

Comparing Monoclinic-Cubic (CsH_2PO_4) and Monoclinic-Tetragonal ($CsHSO_4$), we can see that hysteresis width increases with the increase of the volume change during transformation as well as the distance of the middle eigenvalue from one.

Monoclinic – Trigonal ($Rb_3H(SeO_4)_2$) system despite ***unusual large contraction*** by 2.67% during transformation to the high temperature phase, has the smallest temperature hysteresis among all three classes. Middle eigenvalue was calculated based on single crystal X-ray diffraction data analysis (at 450K and 470K) and was the closest to 1 (1.006857) among studied solid acids.

Although we studied materials with different transformation symmetry, transformation temperature, chemical composition and transformation volume, we can see the clear correlation between middle eigenvalue and measured hysteresis. We can conclude that austenite-martensite theory holds, while applied to the solid acids materials and qualitatively correctly predicts the hysteresis width.

This suggests that it is neither volume change nor different symmetry relationship, but crystallographic compatibility between phases that determines mechanical failure (and hysteresis) during the transformation between phases.

4.4 $Cs_{1-x}Rb_xH_2PO_4$ as a model system of the austenite-martensite transformation

CsH_2PO_4 forms isostructural solid solution series with rubidium substitution ($Cs_{1-x}Rb_xH_2PO_4$). Extensive characterization of materials in the $Cs_{1-x}Rb_xH_2PO_4$ at ambient conditions was done by Cowan[15]. It shows the Rb solubility limit in CsH_2PO_4 to be ~ 80 mol% and shows the occurrence of a high-temperature polymorphic transition to a high conductivity phase for all compositions (including x = 1). Our studies have also revealed that the superprotonic transition temperature generally increases with increasing Rb content[16].

The CsH_2PO_4 – RbH_2PO_4 pseudo-binary system serves as an ideal model because of the wide solubility range. Up to ~ 80 mol% Rb can be substituted into the CsH_2PO_4 structure type, the features of the room-temperature, monoclinic phase vary monotonically with composition, and all compositions display a superprotonic transition (T_{tr} = 220-270 °C).

While the structure of CsH_2PO_4 at high temperature phase are known, the high-temperature crystal structures of all other members of the solution, $Cs_{1-x}Rb_xH_2PO_4$, where x > 0, remain unknown. Determination of these structures is critical both to understanding the nature of superprotonic conductivity and for evaluating the new theory of martensitic transitions. It is also critical to know low temperature anisotropic expansion coefficient and lattice parameters at the transformation temperature. We will address those issues in the following sections.

4.4.1 Determine lattice parameters in $Cs_{1-x}Rb_xH_2PO_4$ from 25 to 200^0C

Determination of the lattice parameters at low and high temperature phases in solid solution series CsH_2PO_4 – RbH_2PO_4 brings several significant challenges. It becomes more and more difficult to access the higher Rb-content materials as a consequence of high temperature dehydration. A water partial pressure of 0.3 atm is required to observe the superprotonic phase for x = 0.6, whereas only about 0.05 atm is required for x = 0. Dehydration starts at temperatures below 190^0C for x>0. In the case of x = 1 (the Rb end-member) reliable conductivity data could only be obtained under high pressure (1 GPa).

Extreme precautions are required to avoid dehydration during high temperature X-ray diffraction data collection, since we cannot sustain high humidity levels inside the entire XRD camera for a long time. Localized humidification technique was used.

High temperature diffraction patterns were recorded at 1^0/min heating rate and collected only on heating. Only high quality powders were used and less scans on heating and cooling were performed as well as smaller 2 theta range (10-60), to decrease the experiment time.

Lattice parameters temperature dependence was determined based on Rietveld refinement using X'Pert Plus software package. The structures reported by Ueso[4] and by Yamada[5] for low and high temperature, respectively, were used as starting models. The following parameters were refined for all phases:

- Lattice constants, scale factors,

- Overall isotropic atomic displacement parameter.

- Peak profiles, $\Gamma = (W + U*\tan^2\theta + V*\tan\theta)^{1/2}$ (3 refined parameters per phase)

- 6 background parameters and zero shift parameter

Summary of the refinement is provided in Table 4-4.

Table 4-10 Rietveld refinement parameters for $Cs_{1-x}Rb_xH_2PO_4$ at different temperatures

Heating	$Cs_{0.75}Rb_{0.25}H_2PO_4$			$Cs_{.050}Rb_{0.50}H_2PO_4$		
Heating	R (expected)/ %	R (profile)/ %	R (weight. Profile)/ %	R (expected) / %	R (profile)/ %	R (weight. Profile)/ %
30^0C	2.493	8.011	11.341	2.215	8.542	12.415
100^0C	2.495	8.631	12.489	2.212	8.392	12.381
125^0C	2.496	8.584	12.268	2.211	8.364	12.358
150^0C	2.497	8.355	11.892	2.211	8.33	12.249
170^0C	2.498	8.408	11.9	2.211	8.411	12.439
190^0C	2.505	8.514	11.893	2.211	8.376	12.413
200^0C	2.511	12.305	18.474	2.213	8.337	12.47
Heating	$Cs_{0.25}Rb_{0.75}H_2PO_4$					
30^0C	1.881	14.562	21.65			
100^0C	1.881	13.998	20.873			
125^0C	1.881	13.658	**20.438**			
150^0C	1.881	13.334	**20.24**			
170^0C	1.881	13.12	**20.143**			
190^0C	1.881	12.917	**19.899**			
200^0C	**1.881**	**12.981**	**19.911**			

Typical refinement results are shown in Figure 4-9. We can see that all the samples were phase pure and have a monotonic decrease in lattice parameters with the increase of the Rb-content.
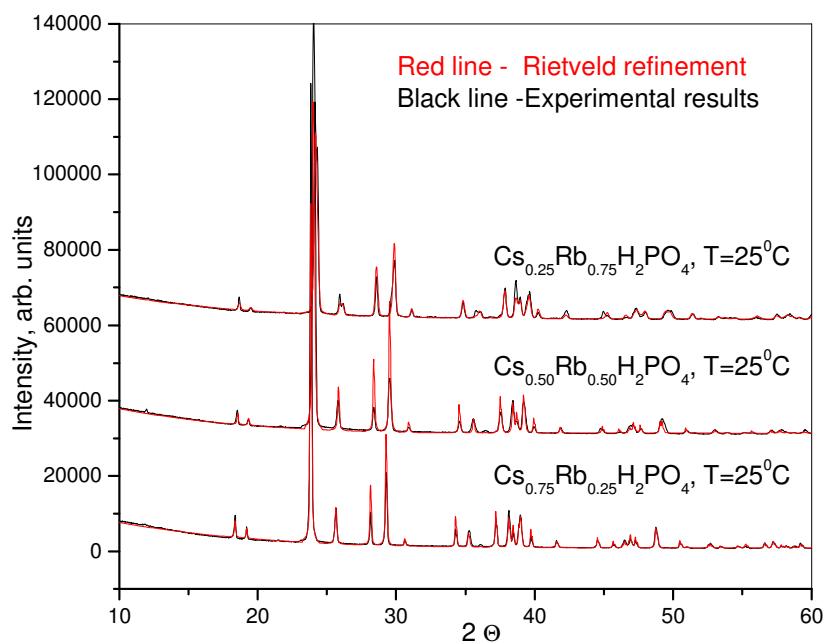
Figure 4-9 Rietveld refinement and experimental X-ray diffraction curves for Cs$_{1-x}$Rb$_x$H$_2$PO$_4$ at room temperature

We do need to extract the lattice parameters at the transformation temperatures. Since the highest temperature of the X-ray diffraction for monoclinic phase was 200^0C, we extrapolated the lattice parameters up to the real transformation temperature.
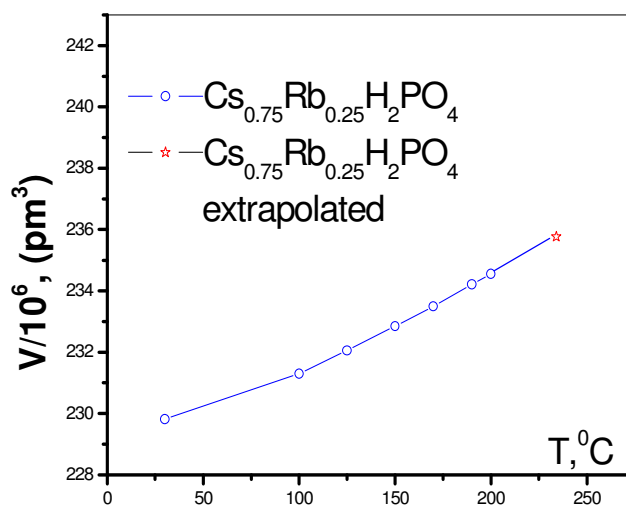
Figure 4-10 Volumetric expansion of the Cs$_{0.75}$Rb$_{0.25}$H$_2$PO$_4$ in monoclinic phase extrapolated values up to 234^{0}C

Same analysis was performed for other members of the solid solution. Anisotropic thermal expansion and lattice parameters were determined in 25-200^{0}C range (see Figure 4-11).
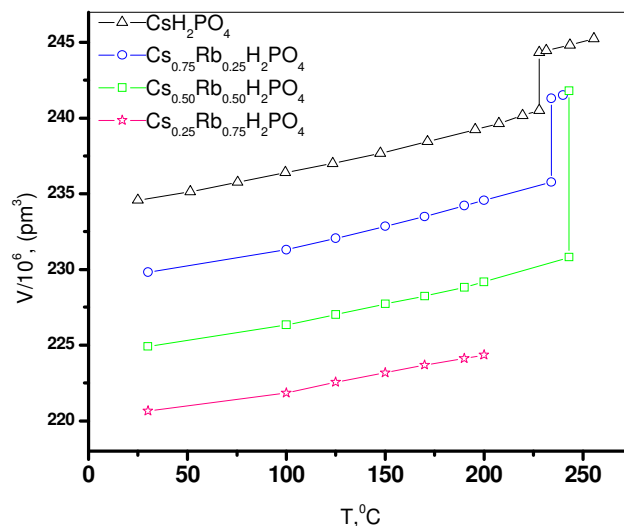
Figure 4-11 $Cs_{1-x}Rb_xH_2PO_4$ temperature lattice parameters dependence (for high temperature phase structure see below)

4.4.2 High temperature structure determination and volume change during transformation

High temperature structures of the $Cs_{1-x}Rb_xH_2PO_4$ were not known except for x=0. As a part of our work, we needed a high temperature structure and lattice parameters. High temperature X-ray investigation of the $Cs_{0.75}Rb_{0.25}H_2PO_4$ was performed. As mentioned earlier, the compound is not stable at the high temperature phase under ambient conditions. Several techniques were introduced to successfully obtain structure information and avoid dehydration. Faster heating rate and shorter collection times were used. We were successful in getting the high temperature diffraction pattern, although some amount of the monoclinic phase was present, Figure 4-12.
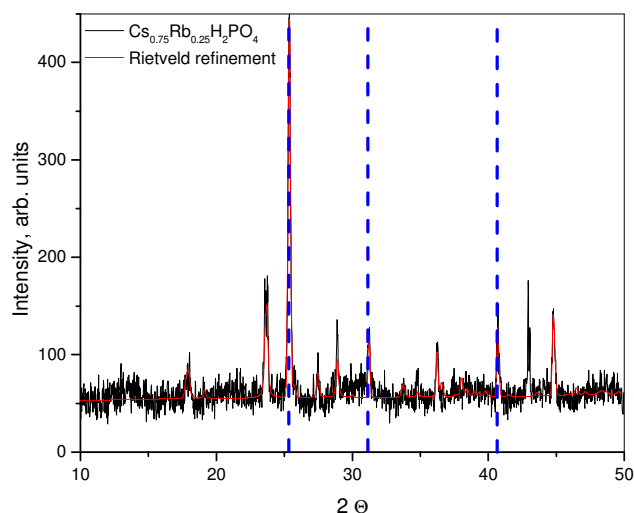
Figure 4-12 X-ray diffraction pattern with the cubic (51wt%) and monoclinic (49 wt%) phase of the $Cs_{0.75}Rb_{0.25}H_2PO_4$ at 240^0C

High temperature phase of the $Cs_{0.75}Rb_{0.25}H_2PO_4$ at 240^0C is cubic (blue dash lines representing unique reflections on Figure 4-12), with lattice parameters:

a/ Å	4.943(2)
b/ Å	4.943(2)
c/ Å	4.943(2)
α/ °	90
β/ °	90
γ/ °	90
V/ 10^6 pm^3	120.769

Table 4-11 Occupancy, atomic fractional coordinates and isotropic displacement parameters B for $Cs_{0.75}Rb_{0.25}H_2PO_4$

Atom	Wyck.	s.o.f.	x	y	z	B/ 10^4 pm^2
Cs1	1a	0.750000	0.000000	0.000000	0.000000	5.000000
P1	1b	1.000000	0.500000	0.500000	0.500000	14.6000
O1	24l	0.166700	0.500000	0.247960	0.321990	25.5000

Table 4-12 Indices, 2Theta values, calculated and observed relative intensities of

$Cs_{0.75}Rb_{0.25}H_2PO_4$

h	k	l	2Theta	d-spacing	Icalc.	Iobs.
0	0	1	17.931	4.94294	74	69
0	1	1	25.464	3.49519	998	1000
1	1	1	31.319	2.85381	135	143
0	0	2	36.321	2.47147	91	99
0	1	2	40.787	2.21055	160	162
1	1	2	44.881	2.01795	220	218

This finding allowed us to compare the crystallographic parameters at least for two members of the solution series.
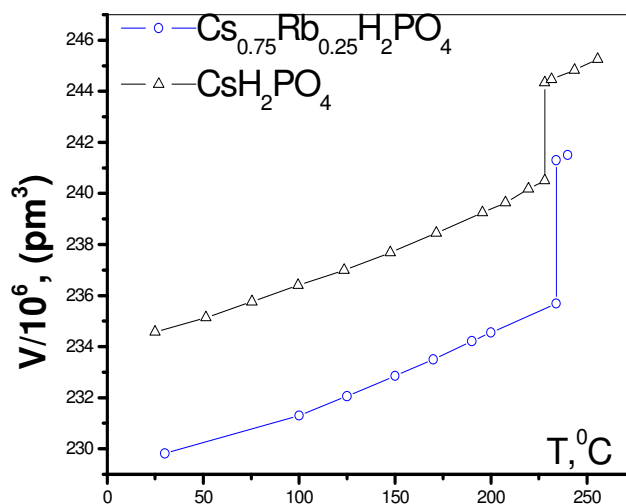
Figure 4-13 $Cs_{0.75}Rb_{0.25}H_2PO_4$ and CsH_2PO_4 volume expansion and transformation volume (dV/V$_{tr}$ 2.322% at T$_{tr}$=234^{0}C, 1.55% at 228^{0}C, respectively)

Final lattice parameters at the transformation temperature (234^{0}C) for $Cs_{0.75}Rb_{0.25}H_2PO_4$ will be

Monoclinic phase CsH_2PO_4 Cubic phase CsH_2PO_4

At 234 °C	At 234 °C

$$a = 7.8712(3) \text{ Å}$$

$$a_o = 4.9413(1) \text{ Å}$$

$$b = 6.4923(2) \text{ Å}$$

$$c = 4.8180(4) \text{ Å}$$

$$\beta = 106.809(9) \,°$$

$$V = 235.6939(1) \text{ Å}^3$$

4.4.4 Estimating volume change during phase transformation for CsH_2PO_4-RbH_2PO_4 solid solution system

We were not be able to get exact lattice parameters of the high temperature phase of the $Cs_{1-x}Rb_xH_2PO_4$, x>0.25 by high temperature X-ray diffraction techniques due to a high humidity requirement.

We used the dilatometer measurement technique to estimate volume change during the transition. Dilatometer measurements were held under the minimum amount of force (150 mN) necessary to minimize the effect of the creep. Cylindrical pellets, pressed from ground powders, with the density of at least 96% of theoretical was used for measurements. Heating rate of 1^0/min was used; data was recorded every 5 seconds. Sides of the samples were covered with the silicon grease to prevent dehydration at high temperatures. Since our samples were crystalline powders, thermal expansion was assumed to be uniform and vertical displacement was measured as a function of time and temperature. Two parameters of interest were extracted from the date – thermal expansion coefficient and volume change during phase transition. In the case of the phase transition with significant volume change, sudden sample's height expansion (or

contraction) was observed. To convert linear thermal expansion to volumetric expansion, well know relationship was used (3*linear thermal expansion = volumetric thermal expansion coefficient).

It was also found that untreated samples of the material experience rapid expansion at around 80-120^{0}C, while samples from powders heated for 4 hours at 120^0-190^{0}C prior to pressing do not. The sudden expansion of untreated samples was attributed to the absorbed water loss, causing the expansion. That did not affect the actual measurement of the volume change during transformation. Since we measured volume change for some compositions of the solid solution series by X-ray diffraction technique, we can compare it with our measurements. It was noticed that untreated samples always yielded lower values of the expansion, probably due to lower pellet densities right before the transformation. Sintered sample, on the other hand always provided values very close to the diffraction data. Examples of the data and comparison with the diffraction data are shown in Figure 4-14.

CsH_2PO_4
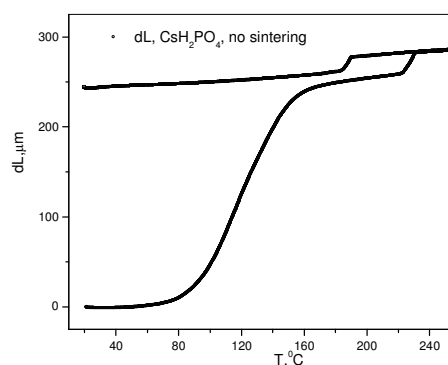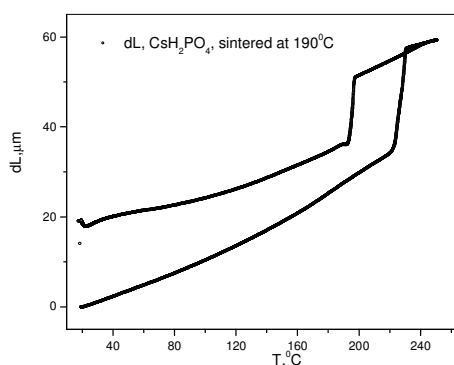
| After sintering; dV/V | **1.799%** | Before sintering: dV/V | **1.747%** |

Density,% theor.   90.3%   Density,%theor   100.0%

(dV/V from diffraction data: **1.7854%**   T=219-231^{0}C
                                        1.55%   T$_{tr}$=228^{0}C

$Cs_{0.75}Rb_{0.25}H_2PO_4$
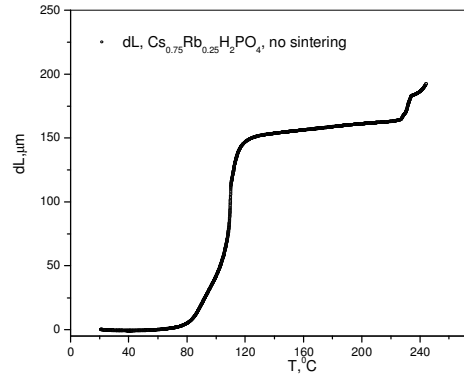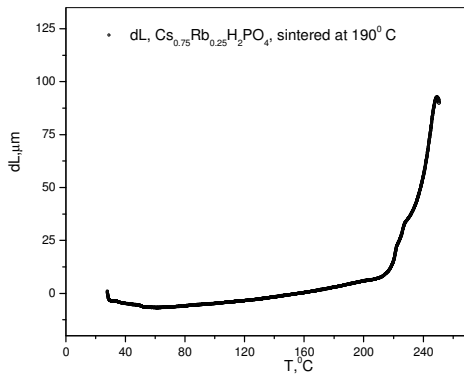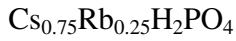
After sintering; dV/V   **3.202%**   Before sintering: dV/V   **1.958%**
Density,% theor.   91.7%   Density,%theor   94.8%
                                 215-228^{0}C   227-234^{0}C
(dV/V from diffraction data: **2.97%**   T=219-231^{0}C
                             2.322%   T$_{tr}$=234^{0}C

$Cs_{0.5}Rb_{0.5}H_2PO_4$
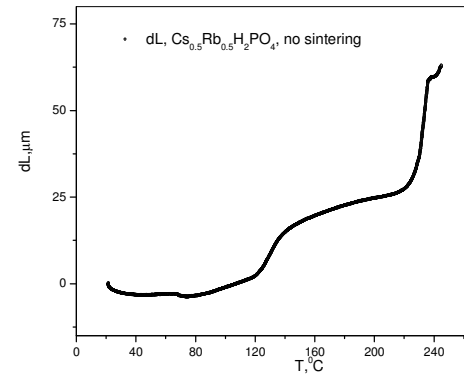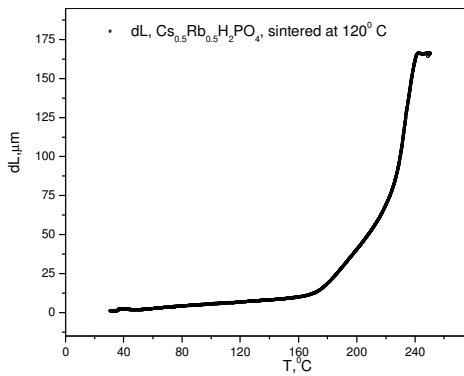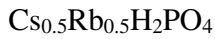
After sintering; dV/V   **5.293%**   Before sintering: dV/V   **4.507%**
Density,% theor.   94.9%   Density,%theor   90.2%
                                 232-241^{0}C   220-238^{0}C

Figure 4-14 Dilatometer measurements for volume change during phase transitions

This method allowed us to measure the volume change during transformation for $Cs_{0.5}Rb_{0.5}H_2PO_4$, which was not possible by the X-ray diffraction technique. Relative volume change was found to be between 4.507-5.293%.

4.6 Comparison of the transformation parameters to the hysteresis width and conclusions for CsH_2PO_4-RbH_2PO_4 solid solution system

CsH_2PO_4-RbH_2PO_4 solid solution series allows us to test the limits of the austenite-martensite theory. Rb-atoms are randomly distributed on a Cs-position in the structure. Due to the smaller ionic radius of Rb, unit cell volume decreases with the increase of Rb-content. That allows us to vary crystallographic parameters of high and low temperature phase, while minimizing other changes, such as transformation temperature, phase symmetry. For the first time high temperature phase of $Cs_{0.75}Rb_{0.25}H_2PO_4$ was determined.

Crystallographic parameters of transformation are shown in Table 4-13.

Table 4-13 Summary of the transformation parameters for CsH_2PO_4-RbH_2PO_4 solid solution series

Monoclinic-Cubic	Volume change*, %	Middle eigenvalue	Measured Hysteresis[16], ^0C
CsH_2PO_4 (x=0)	**1.55**	**0.93199**	**13.4**
$Cs_{0.75}Rb_{0.25}H_2PO_4$ (x=0.75)	**2.32**	**0.92906**	**13.8**
$Cs_{0.5}Rb_{0.5}H_2PO_4$ (x=0.5)	**4.8****	**0.91872****	**16.0**

* Positive values mean expansion upon transition from low to high temperature phase, negative- contraction.
** Estimated from the dilatometer measurements under assumption that high temperature phase is cubic.

Analysis of the transformation matrix U_1 shows that at current lattice parameters middle eigenvalue is defined as

$$\lambda_2 = a_0 / b * \sqrt{2},$$

Equation 4-7

where a_0 – cubic phase lattice parameter and b-monoclinic phase parameter.

Middle eigenvalues are getting further away from 1 with the increase of the Rb-content. That, according to the austenite-martensite theory, should lead to the increase of the hysteresis. We can see very slight hysteresis increase with Rb increase from 0 to 0.25 by 0.4^0C and significant increase by 2.2^0C when Rb content increases from 0.25 to 0.5. We can say that the hysteresis behavior is dependant on crystallographic parameters, according to the austenite-martensite theory. Although the dependence is much weaker than compared to shape memory alloys. A major reason for that might be the fact that solid acids are ionic salts and have high plasticity at elevated temperatures and can accommodate higher strains in the lattice.

References

[1] Cui, J., Y. S. Chu, et al. (2006). "Combinatorial search of thermoelastic shape-memory alloys with extremely small hysteresis width." <u>Nature Materials</u> 5(4): 286-290.

[2] Chisholm, C. R. I. and S. M. Haile (2000). "X-ray structure refinement of CsHSO4 in phase II." <u>Materials Research Bulletin</u> **35**(7): 999-1005.

[3] Itoh, K., T. Ukeda, et al. (1990). "Redetermination of the Structure of Cesium Hydrogensulfate." <u>Acta Crystallographica Section C-Crystal Structure Communications</u> **46**: 358-361.

[4] Uesu, Y. and J. Kobayashi (1976). "Crystal-Structure and Ferroelectricity of Cesium Dihydrogen Phosphate Csh-2po4." <u>Physica Status Solidi a-Applied Research</u> **34**(2): 475-481.

[5] Yamada, K., T. Sagara, et al. (2004). "Superprotonic conductor CsH2PO4 studied by H-1, P-31 NMR and X-ray diffraction." <u>Solid State Ionics</u> **175**(1-4): 557-562.

[6] Sinitsyn, V. V., A. I. Baranov, et al. (1995). "Pressure Effect on Phase-Transitions and Protonic Conductivity in Rb3h(Seo4)(2) and (Nh4)(3)H(So4)(2)." Ibid. **77**: 118-121.

[7] Merinov, B. V., S. M. Haile, et al. (2002). "Crystal structure of the "intermediate" phase of the protonic conductor Rb3H(SeO4)(2)." Ibid. **146**(3-4): 355-365.

[8] Shchepetilnikov, B. V., A. I. Baranov, et al. (1990). "Elastic Wave Interaction with the Proton Subsystem in Rb3h(Seo4)2." <u>Fizika Tverdogo Tela</u> **32**(10): 2885-2894.

[9] Dilanyan, R. A., V. V. Sinitsyn, et al. (1994). "The Discovery of an Intermediate Phase between the Low-Conducting and Super-Protonic Phases in Rb3h(Seo4)2 Crystal." <u>Kristallografiya</u> **39**(3): 484-487.

[10] Merinov, B. V., U. Bismayer, et al. (1999). "Mixed alkali metal selenate proton conductors: Phase transitions and crystal structure of [Rb-0.54(NH4)(0.46)](3)H(SeO4)(2)." Phase Transitions **69**(4): 439-453.

[11] Melzer, R., R. Sonntag, et al. (1996). "Rb3H(SeO4)(2) at 4K by neutron powder diffraction." Acta Crystallographica Section C-Crystal Structure Communications **52**: 1061-1063.

[12] Fortier, S., M. E. Fraser, et al. (1985). "Structure of Trirubidium Hydrogenbis(Sulfate), Rb3h(So4)2." Ibid. **41**(Aug): 1139-1141.

[13] Melzer, R., T. Wessels, et al. (1996). "The structure of the proton conducting phase of Rb3H(SeO4)(2) at 470 K." Solid State Ionics **92**(1-2): 119-127.

[14] Louie, M., D. Smirnova, M. Swaroop. Martensitic transformations in cesium dihydrogen phosphate Micromechanics 260a, California Institute of Technology

[15] Cowan, L. A., PhD Thesis, Ch. 6. California Institute of Technology

[16] Louie, M.W., M. Kislitsyn, et al., (2009). "Phase transformation and hysteresis behavior in $Cs_{1-x}Rb_xH_2PO_4$" Solid State Ionics, doi:10.1016/j.ssi.2008.11.014

Chapter 5. Influence of inert media on phase transformations in CsHSO$_4$/SiO$_2$ and role of interface interactions

5.1 Heterogeneous doping in the solid acids ionic conductors

Oxide additives, such as SiO$_2$, TiO$_2$, Al$_2$O$_3$ [1,2,3,4,5,6,7,8,9] have been recently used as additives to ion conductors to improve its properties. The original goal was to sacrifice some of the conductivity but achieve higher mechanical stability of the devices. Although, it has been surprisingly observed that some additives dramatically enhance the conductivity at temperatures below the superionic transition. As a consequence, in almost all cases, the magnitude of the conductivity discontinuity otherwise observed at the superprotonic transition is substantially lowered. Such smoothing of the conductivity behavior can be anticipated to be beneficial in technological applications.

CsHSO$_4$ has been a model material for studying the influence of oxide additives on proton transport properties. Introduction of SiO$_2$ into CsHSO$_4$ has been shown to influence the phase behavior. There is strong evidence that the SiO$_2$ induces amorphization of the solid acid (as reflected in the broadening of X-ray powder diffraction peaks), and it has been proposed than an amorphous interfacial phase forms between the silica and the solid acid. On cooling from high temperature, it has further been observed that the transformation from phase II to phase III is highly retarded in the presence of SiO$_2$, whereas the influence on the phase I to II transformation is minimal. These effects have largely been observed in composites formed using microporous SiO$_2$

(having nanoscale pores) and subjected to heat treatment at ~ 150 – 210 °C prior to characterization so as to achieve infiltration of the $CsHSO_4$ into the silica pores[3,5,7,8,9]. As a consequence, it has not been possible to establish whether the modifications to the phase behavior of $CsHSO_4$ are a result of strong chemical interactions between the solid acid and silica, or of the high temperature treatment, or of mechanical stresses during preparation.

In this Chapter we investigate the interaction of $CsHSO_4$ with nanoparticles rather than microporous SiO_2, where the composites are not subjected to high temperature treatment, with the aim of establishing the nature of the interaction of SiO_2 and $CsHSO_4$ in the absence of mechanical and thermal effects. In second part we will focus on the phase transformation on heating and cooling. There were no direct crystallographic studies of the $CsHSO_4$ and its composites at the temperatures above and below superionic transformation. This work will also focus on the origin of the conductivity behavior from the phase equilibrium point of view.

5.2 Influence of the silica on the phase behavior in $CsHSO_4$

The as-synthesized $CsHSO_4$ (prepared in the absence of SiO_2) was confirmed to be entirely phase III and the annealed material to be entirely phase II, Figure 5-1. The diffraction patterns of the as-synthesized composites, Figure 5-1, reveal that in the presence of relatively small amounts of SiO_2, $CsHSO_4$ crystallizes as phase III as expected. We will describe samples as CHS-XX, where XX-mole per cent of the $CsHSO_4$. It is important to note that there is a significant difference in molar and weight per cent. See Table 5-1 for details.

Table 5-1 Nominal compositions of CsHSO$_4$ – SiO$_2$ composite samples prepared in this work

Name	Mol % CsHSO$_4$	Weight % CsHSO$_4$	Vol % CsHSO$_4$
CHS-10	10	29.8	24.5
CHS-20	20	48.9	42.3
CHS-30	30	62.1	55.7
CHS-40	40	71.9	66.1
CHS-50	50	79.3	74.5
CHS-60	60	85.2	81.5
CHS-70	70	89.9	87.2
CHS-80	80	93.9	92.1
CHS-90	90	97.2	96.3

It was noticed that silica does strongly affect phase behavior of the CsHSO$_4$. With increasing SiO$_2$ content, otherwise metastable phase II occurs in significant quantities and is the dominant crystalline phase for CHS-30 samples. That can be observed from unique phase-II peak appearance in the diffraction pattern (17.6 and 32.0 °2Θ) Figure 5-1(b). These peaks are also significantly broader than those of phase III.

Simultaneously, we observed the increase of the amorphous material (amorphous CsHSO$_4$), which can be seen by increasing intensity of a broad amorphous peak centered at ~ 23 °2Θ. In fact, for the highest SiO$_2$ content sample no crystalline peaks are observed despite the nominal CsHSO$_4$ content of almost 30 wt% (10 mole%), Figure 5-1(b).
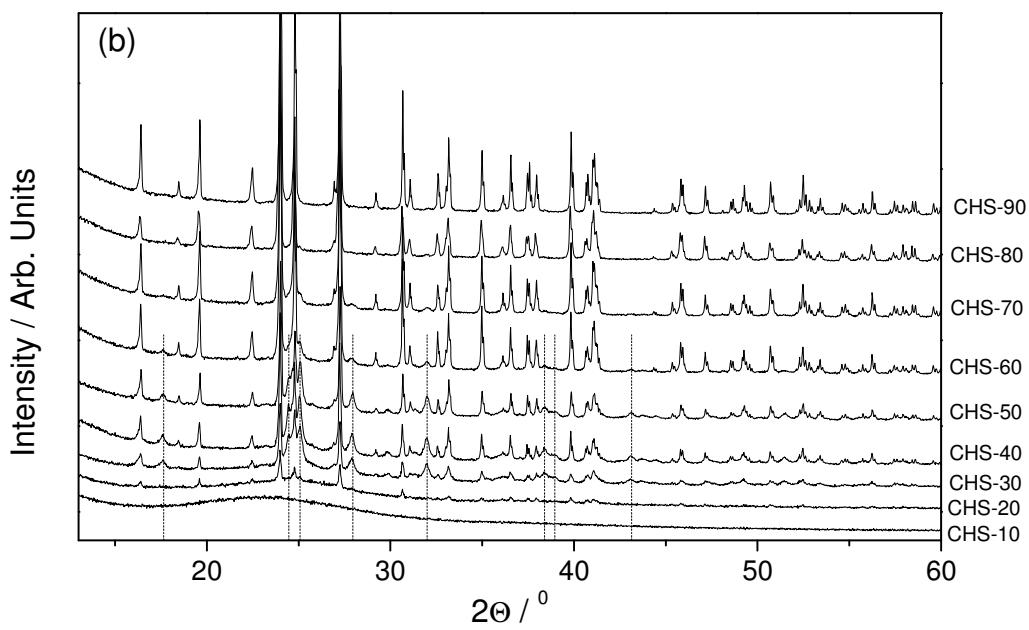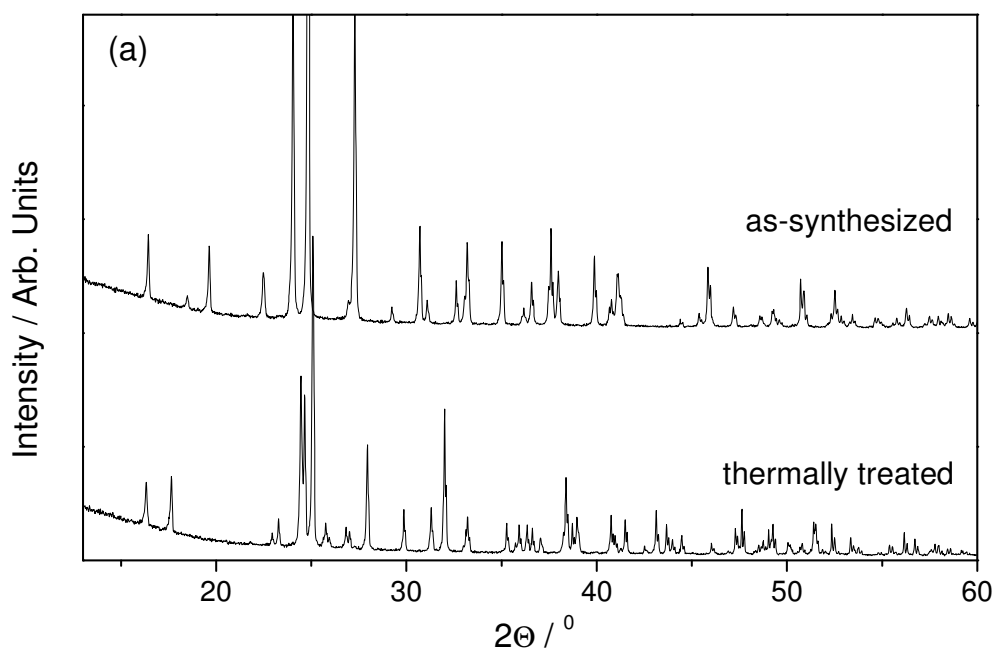
Figure 5-1 X-ray diffraction patterns of (a) pure phase-II and phase-III CsHSO$_4$ (b) composites of CsHSO$_4$ and SiO$_2$. Selected peaks uniquely attributable to phase II are indicated

5.3 Rietveld refinement of the crystalline phases at room temperature

Quantitative analysis of the crystalline phases in composites was performed using both Rietveld refinement following background subtraction and by direct evaluation of the peak intensities in the raw patterns.

Rietveld refinement was carried out using the software package X'Pert Plus[10],[11]. The structures reported by Chisholm[12] and by Itoh[13] for phases II and III, respectively, were used as starting models.

The following parameters were refined for all phases:

- Scale factors.

- Overall isotropic atomic displacement parameter and site occupancies.

- Peak profiles, $\Gamma = (W + U*\tan^2\theta + V*\tan\theta)^{1/2}$ (3 refined parameters per phase)

- 4 background parameters and zero shift parameter

- preferred orientation parameter (modified Bragg intensity $P_k = \exp(P_1 * a_k^2)$, where a_k is the acute angle between the scattering vector and the normal to the crystallites (1 parameter per phase)

Scale factors for the two phases directly yield the relative amounts of phases II and III in each of the composites. The relevant diffraction data for a typical analysis, specifically the CHS-50 sample, are shown in Figure 5-1.
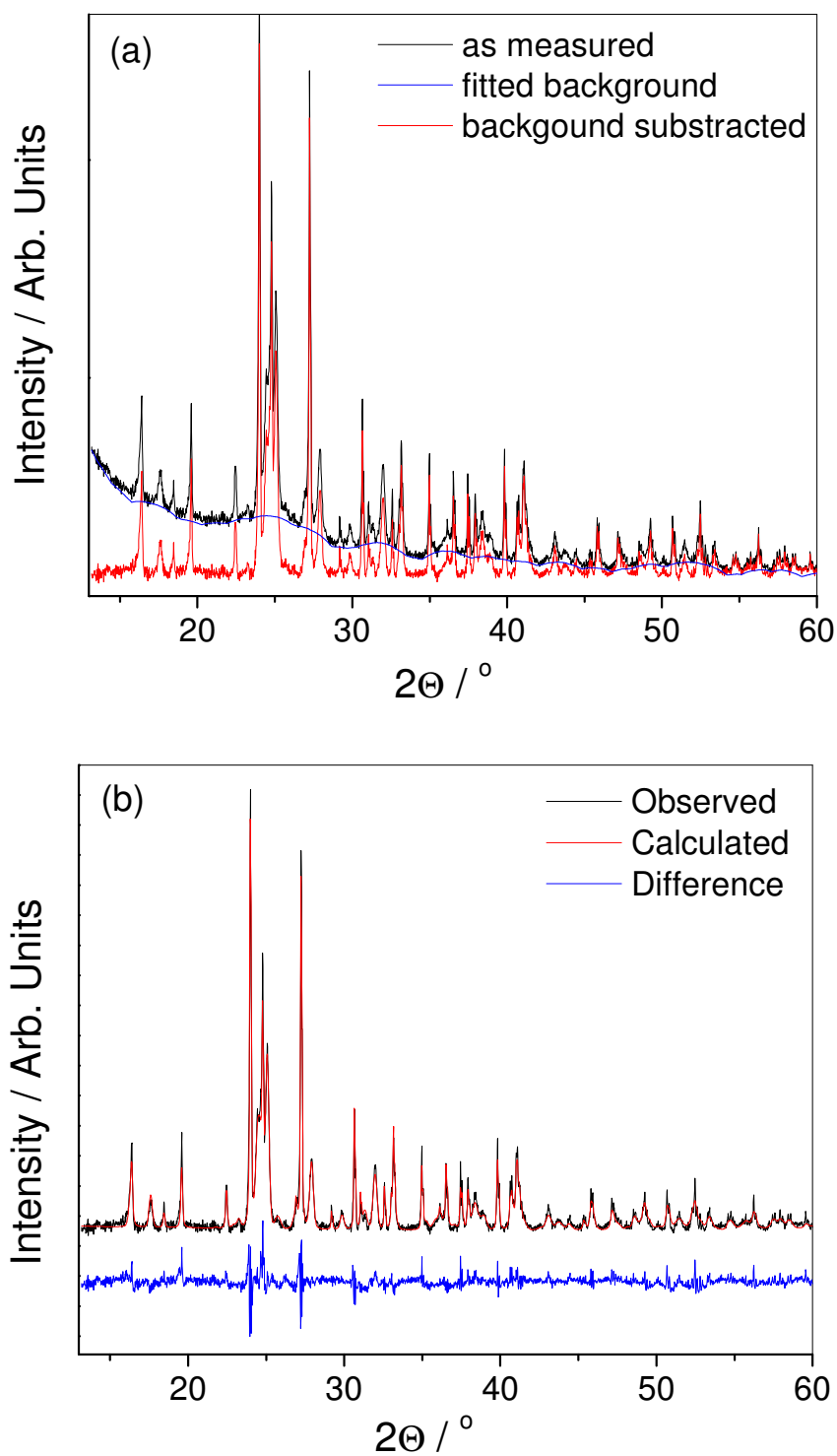
Figure 5-2 X-ray powder diffraction patterns of CHS-50 (a) Comparison of raw and background subtracted patterns, and (b) comparison of observed (background

corrected), calculated and difference patterns (the latter two obtained from Rietveld refinement)

Since phase-II $CsHSO_4$ is metastable at room temperatures, it is important to check long term stability of the composites. Sets of additional experiments were performed – as-synthesized composite was compared to the aged for 1 year sample. Diffraction pattern and phase contents are identical (Figure 5-3).
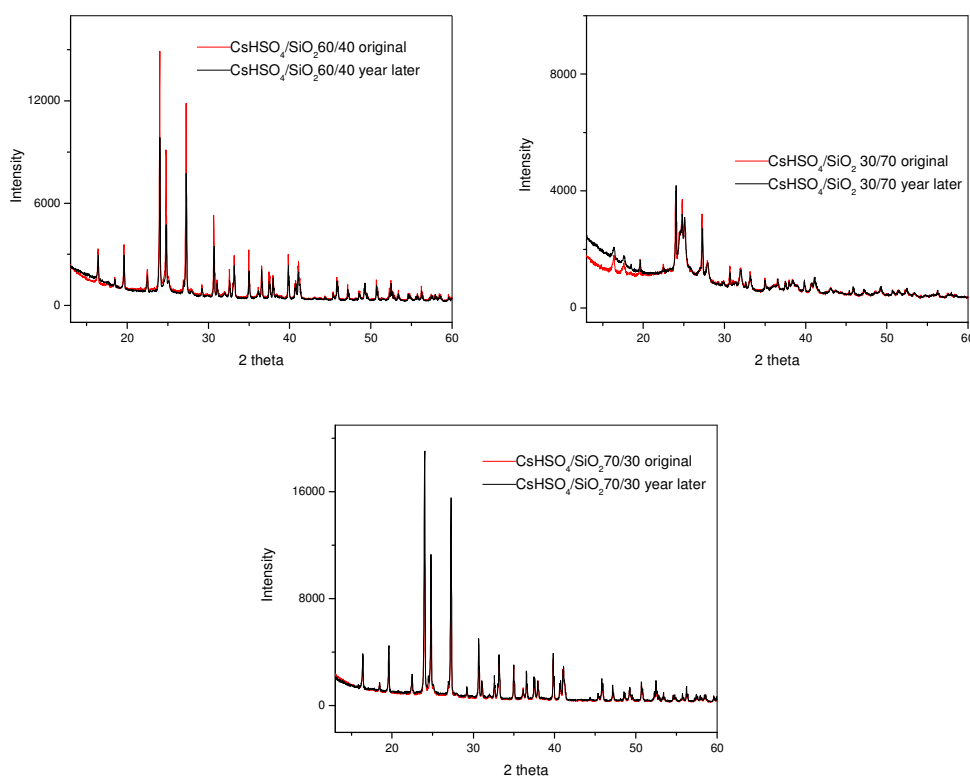
Figure 5-3 X-ray diffraction patterns of the $CsHSO_4$ composites as-synthesized and after one year

The results of the refinements for all compositions are summarized in Table 5-2, which shows stability of the composites over long term with identical phase fractions of the crystalline phases.

In addition, to provide the estimate of the amorphous phases the integrated intensity of the background profiles was additionally evaluated for the 2Θ range 20 to 30 °.

Table 5-2 Selected Rietveld refinement parameters of the CsHSO₄- SiO₂ composites The refinement statistics, R_{exp}, R_{prof}, $R_{w,prof}$, and R_{Bragg} have their usual meanings[14]. The background is the integrated intensity due to the fitted background function over the 2Θ range 20 – 30 °

Sample	R_{exp}, %	R_{prof}, %	R_{Bragg}-II, %	R_{Bragg}-III, %	$R_{w,prof}$ %	Weight % phase-II	Bkgd
CHS-10	n/a	n/a	n/a	n/a	n/a	n/a	11.6(5)
CHS-20	n/a	n/a	n/a	n/a	n/a	20[a]	6.7(5)
aged	n/a	n/a			n/a	8[a]	
CHS-30	5.00	7.30	3.90	4.59	9.64	61.0(9)	3.6(5)
aged	3.44	7.38			9.63	61.4(7)	
CHS-40	4.90	10.16	6.31	4.69	12.83	47.4(8)	2.7(5)
aged	3.54	8.94			11.53	49.7(8)	
CHS-50	6.16	10.13	5.20	5.16	13.10	47.5(3)	0.1(5)
aged	6.16	10.13			13.10	47.5(3)	
CHS-60	4.42	9.94	4.59	5.21	12.91	13.7(2)	1.0(5)
aged	3.43	9.20			12.15	14.1(4)	
CHS-70	4.52	10.45	6.55	4.57	13.42	4.7(8)	1.2(5)
aged	3.36	9.13			12.24	3.6(3)	
CHS-80	5.15	11.56	6.74	6.43	15.01	1.5(9)	0.3(5)

| CHS-90 | 4.59 | 12.29 | n/a | 7.61 | 15.99 | <1 | 0.5(5) |

(a) Rietveld refinement was unreliable due to the low quantity of crystalline $CsHSO_4$ in this sample. The values reported are based on direct evaluation of the integrated peak intensity at $2\Theta \sim 25°$.

Final values of the refinement statistics, R_{prof} and R_{Bragg}[14] ranged, respectively, from 7.3 to 12.3%, and from 3.9 to 7.6%. At the highest SiO_2 content the CHS-10 composite displayed no diffraction peaks due to crystalline $CsHSO_4$. Only the results for an analysis of the integrated background intensity are presented for this sample.

Because of the high amorphous fraction of the CHS-20 composite (with 80 mole % SiO_2), the phase III/phase II ratio was estimated directly from the ratio of the integrated intensities of selected peaks (the Rietveld refinement suffers from artifacts under such conditions). Consistent with the raw diffraction patterns presented in Figure 5-1, the phase fraction of phase II generally increases with increasing SiO_2 content up to high concentrations of SiO_2. Specifically, the weight fraction of phase III in the crystalline phase falls almost monotonically from 100% in the presence of 10 mol% SiO_2 to about 40% in the presence of 70 mol% SiO_2. While uncertainty in the phase III/phase II ratio is high for the CHS-20 sample, it is apparent that this sample, displaying a higher concentration of phase III to phase II, deviates from the trend of increasing amounts of phase II with increasing SiO_2 content.

5.4 Derivation of the X-ray diffraction-absorption intensity method for multi-component system with amorphous phases

The Rietveld refinement approach, as implemented here, cannot directly indicate the phase fraction of the amorphous phase, which may differ from the nominal input

quantity of SiO_2. Although the measurement of the intensity of the broad amorphous peak does provide some indication of the amorphous content, it is a qualitative rather than quantitative evaluation.

The following analysis is applicable to any material or mixture of the materials, satisfying certain conditions, mentioned in the Experimental Methods. For any pure crystalline material we can collect the diffraction pattern with corresponding peak intensities (Figure 5-4).
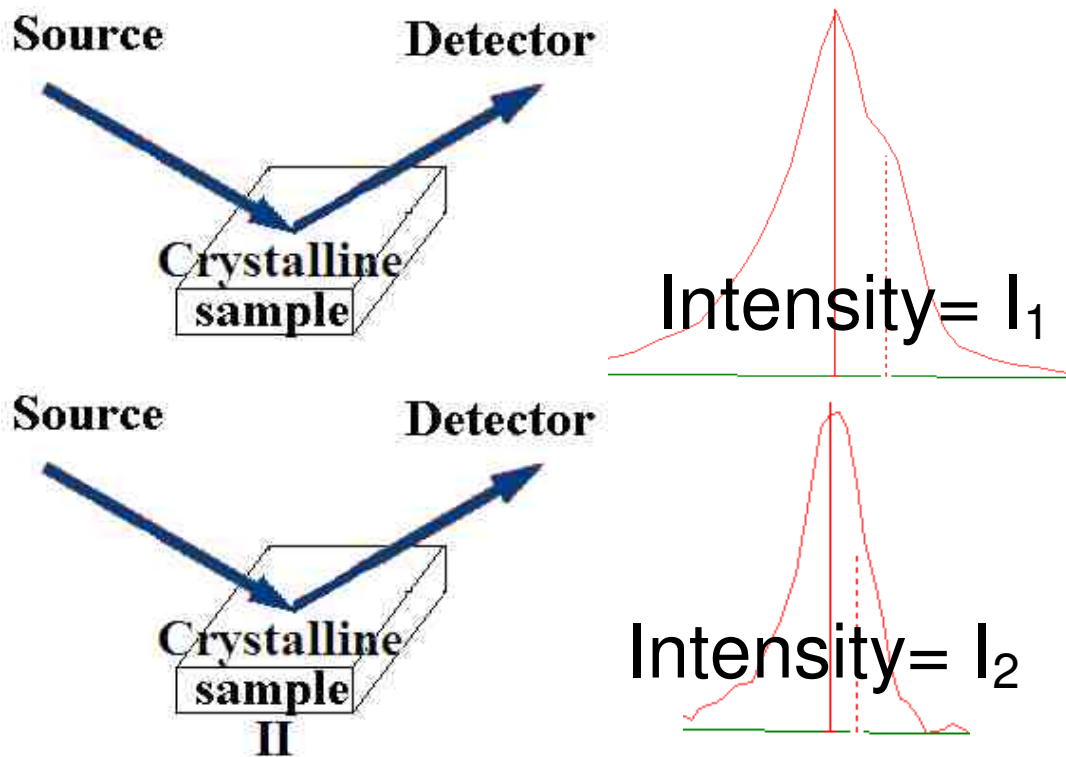
Figure 5-4 Schematic representation of the diffraction from the crystalline samples

The uniform mixture of the crystalline samples will produce the diffraction pattern according to Equation 5-1 and can be schematically represented in Figure 5-5 and Figure 5-6.
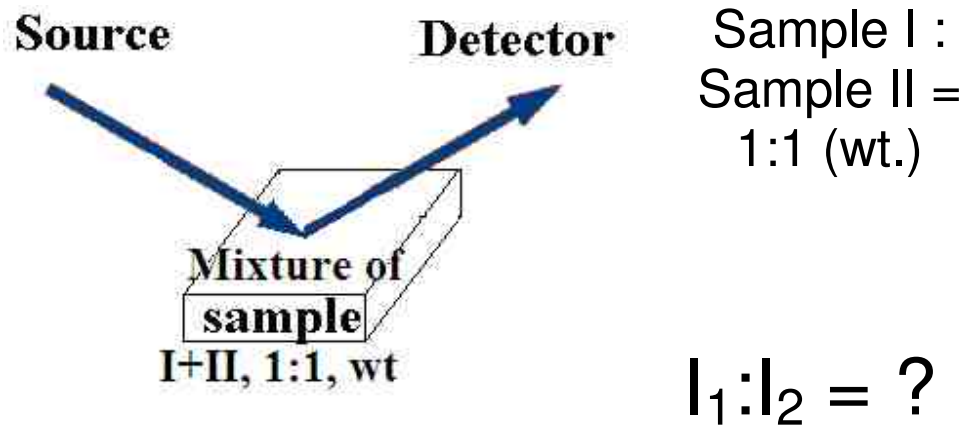
Figure 5-5 Schematic representation of the diffraction from the crystalline samples

- Mass-absorption coefficient
- Density and atomic number
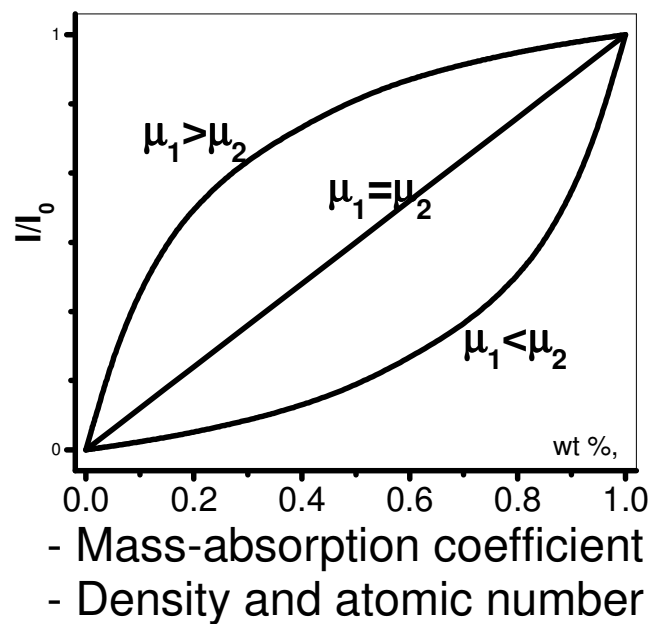
Figure 5-6 Relative peak intensity for materials with different mass-absorption

coefficient

We will start with the Equation 2-5. It represents relative intensity of the diffraction peak as a function of the mass-absorption coefficient and weight fraction for multi-component systems.

$$\frac{I_1}{I_1^{0}} = \frac{\mu_1^{m} * x_1}{\sum\limits_{i=1}^{n} \mu_i^{m} * x_i}$$

Equation 5-1 Relative intensity of the component 1 in the mixture of n components

Where in our case,

μ_i^{m} and x_i – mass absorption coef. and weight fraction of the i-component,

I_1^{0} - Absolute intensity for pure component 1,

I_1 - Absolute intensity for component 1 peaks intensity in the mixture.

To make the derivations easily adoptable to other systems, we will split it in two parts. In any three component system it is important to be able to plot relative intensities vs. weight fraction for all three components on one plot. In the first part we will show how to account for different phase contributions to relative intensities in 3-component system.

In the second part we will show the mathematical approach on how to extract the amorphous material fraction, based on discrepancies between theoretical and measured relative intensities.

a) Contribution of crystalline phases to the relative intensities in n component system (n>2).

By introducing additional constrains on the Equation 5-1, sum of all phase fraction equal 1:

a) $x_3 = 1-x_1-x_2$

Equation 5-2

and potentially known ratio of the two crystalline phases (x_1 and x_2)

b) $x_1/(x_1+x_2) = \omega_1$

Equation 5-3 Weight percent of the phase-III in phase-II phase-III mixture, data taken from Rietveld refinement

In our case, mass-absorption coefficients of the crystalline phases are equal, so we will use that as well. In general, that is not necessary and the same derivation is possible with some additional information even for different materials.

c) $\mu_1^m = \mu_2^m$ (mass absorption coefficients for phase-III (μ_1^m) and phase-II (μ_2^m) are equal), we will get

$$\frac{I_1}{I_1^0} = \frac{\mu_1^m * x_1}{\frac{x_1}{\omega_1}(\mu_1^m - \mu_3^m) + \mu_3^m}.$$

Equation 5-4

Since it is more convenient for us to plot relative intensity vs. total CHS concentration, by substituting $x_1 = \omega_1(x_1+x_2) = \omega_1 * x_{total}$, we will get

$$\frac{I_1}{I_1^0} = \frac{\omega_1 * x_{total} * \mu_{CsHSO_4}^m}{x_{total} * (\mu_{CsHSO_4}^m - \mu_3^m) + \mu_3^m}.$$

Equation 5-5

μ_3^m - mass absorption coefficient of the SiO_2,

μ_{CsHSO4}^m - mass absorption coefficient of the $CsHSO_4$,

$x_{total} = x_1+x_2$ total weight % of both phase-II and III in the system.

If we know the crystalline phase ratio (ω_1) we can calculate the contribution of the other crystalline phase on total relative intensity as a function of weight % of the third component.

b) Calculating amorphous material weight fraction, based on discrepancies between theoretical and measured relative intensities.

We can rewrite Equation 5-1 for relative peak intensities in the n-component system:

$$\frac{I_1}{I_1^0} = \frac{\mu_1^m * x_1}{\sum \mu_i^m * x_i} \, \prime$$

Equation 5-6

In our case we have phase-III CsHSO$_4$, phase-II, CsHSO$_4$, amorphous CsHSO$_4$ and amorphous SiO$_2$ and the expression for the relative intensity of the phase-III CsHSO$_4$ peaks will be:

$$\left(\frac{I_1}{I_1^0}\right)^{Measured} = \frac{\mu_1^m * x_1}{(\mu_1^m * x_1 + \mu_2^m * x_2 + \mu_3^m * x_3 + \mu_a^m * x_a)} \tag{5}$$

Equation 5-7

where in our case,

μ_1^m and x_1 – mass absorption coef. and weight fraction of the phase-III,

μ_2^m and x_2 - mass absorption coef. and weight fraction of the phase –II,

μ_3^m and x_3 – mass absorption coef. and weight fraction of the SiO$_2$,

μ_a^m and x_a- mass absorption coef. and weight fraction of the amorphous $CsHSO_4$,

I_1^0 - absolute intensity for pure phase-III,

I_1 - absolute intensity of the phase-III in the mixture.

In our case that is the value we directly measure (black filled squares in Figure 5-7).

$$\left(\frac{I_1}{I_1^0}\right)^{Measured} = \frac{\mu_1^m * x_1}{(\mu_1^m * x_1 + \mu_2^m * x_2 + \mu_3^m * x_3 + \mu_a^m * x_a)}.$$

Equation 5-8

We can also find the theoretical relative intensity under the assumption that all $CsHSO_4$ will be in the form of phase-III. (black open circles in Figure 5-7)

$$\left(\frac{I_1}{I_1^0}\right)^{Theoretical} = \frac{\mu_1^m * (x_1 + x_2 + x_a)}{(\mu_1^m * x_1 + \mu_2^m * x_2 + \mu_3^m * x_3 + \mu_a^m * x_a)}$$

Equation 5-9

assuming that $\mu_a^m = \mu_2^m = \mu_1^m$, let us divide Equation 5-8 by Equation 5-9 and we will get

$$\left(\frac{I_1}{I_1^0}\right)^{Measured} \Bigg/ \left(\frac{I_1}{I_1^0}\right)^{Theoretical} = \frac{x_1}{x_1 + x_2 + x_a}.$$

Equation 5-10

The resulting expression for the weight fraction of the amorphous material x_a will be

$$\frac{x_1}{\left(\frac{I_1}{I_1^0}\right)^{Measured} \Bigg/ \left(\frac{I_1}{I_1^0}\right)^{Theoretical}} - (x_1 + x_2) = x_a.$$

Equation 5-11

Since the weight fraction notation is for the entire composite,

$x_1 + x_2 + x_a + x_3 = 1$.

Equation 5-12

We will also use $w = x_1/(x_1 + x_2)$ – weight % ration of the phase-III to phase-II from Retvield refinement.

The goal would be to find $\dfrac{x_a}{x_1 + x_2 + x_a}$ as a function of $w = x_1/(x_1+x_2)$ and

$$\left(\dfrac{I_1}{I_1^0}\right)^{Measured} \bigg/ \left(\dfrac{I_1}{I_1^0}\right)^{Theoretical}$$, since those are directly measured parameters. To save space,

$$\left(\dfrac{I_1}{I_1^0}\right)^{Measured} \bigg/ \left(\dfrac{I_1}{I_1^0}\right)^{Theoretical} = m.$$

1. Divide both sides of Equation 5-11 by x_1+x_2. and recognize that $x_1/(x_1+x_2)=w$:

$$\frac{w}{m} - 1 = \frac{x_a}{(x_1 + x_2)}.$$

Equation 5-13

2. Write Equation 5-12 as

$(x_1 + x_2) = 1 - x_3 - x_a$

Equation 5-14

And solve for x_a;

$$x_a = \frac{\left(\frac{w}{m} - 1\right) * \left(1 - x_3\right)}{\frac{w}{m}}.$$

Equation 5-15

recognizing that $1-x_3 = x_1+x_2+x_a$, we will divide both parts of (12) by $x_1+x_2+x_a$:

$$\frac{x_a}{x_1 + x_2 + x_a} = 1 - \frac{m}{w} \quad \text{or} \quad \frac{x_a}{x_1 + x_2 + x_a} = 1 - \frac{\left(\frac{I_1}{I_1^0}\right)^{Measured} \Bigg/ \left(\frac{I_1}{I_1^0}\right)^{Theoretical}}{w} .$$

Equation 5-16

5.5 Application of the X-ray absorption technique for quantitative amorphous phase analysis in the composites

Discrepancy between the measured and computed values of I/Io for crystalline phases of $CsHSO_4$, in particular in cases where the measured value is lower than the computed value, suggest that some of the $CsHSO_4$ is not in the crystalline form. The relevant comparison is provided in Figure 5-7 as a function of $CsHSO_4$ content, where the analysis is performed using the (-1 1 1), (1 1 0), and (0 1 1) diffraction peaks of phase-III (which have relative intensities of 100, 18.8 and 9.2 %, respectively) and the results averaged. It is evident that for composites with low total $CsHSO_4$ content, the measured intensities are lower than the computed values, indicating the 'loss' of some of the crystalline $CsHSO_4$ to amorphization.
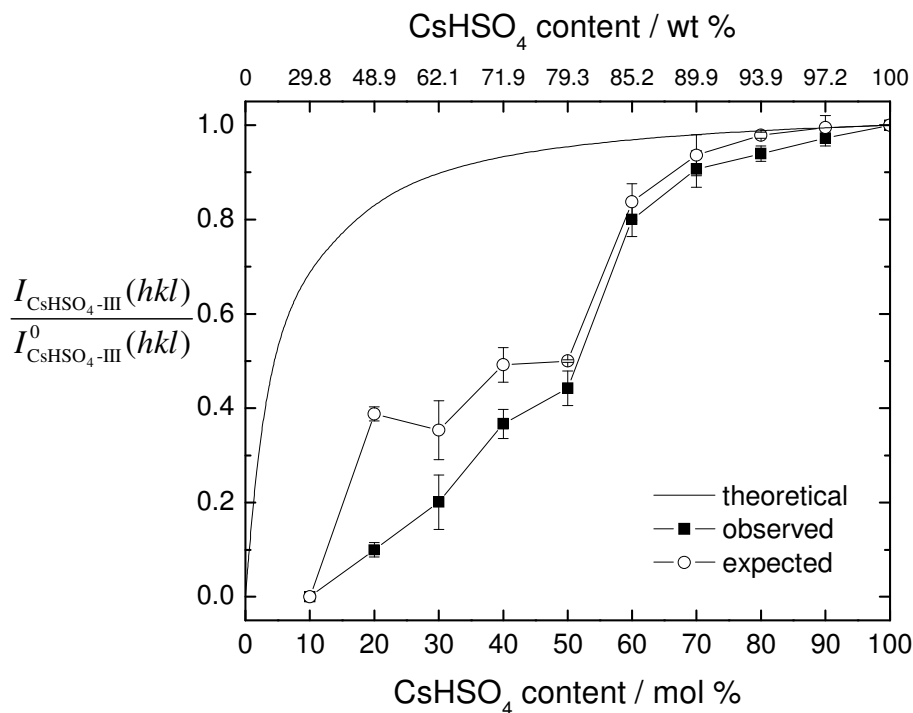
Figure 5-7 X-ray diffraction intensity ratios for CsHSO₄ phase III (for the intensity in the composites relative to the intensity in neat CsHSO₄ phase-III) as a function of CsHSO₄ content

The amount of amorphous $CsHSO_4$ was calculated using Equation 5-16, under assumption that amorphous $CsHSO_4$ has an absorption coefficient equal to that of crystalline $CsHSO_4$.

The results, Table 5-3, indicate that the fraction of $CsHSO_4$ that is amorphized increases monotonically with increasing SiO_2 content, consistent with the overall increase observed in the intensity of the broad amorphous peak with increasing SiO_2 content.

Table 5-3 Weight percent of CsHSO$_4$ that is amorphous (relative to the total amount of CsHSO$_4$ in the system), as determined by an evaluation of the absolute intensities of the diffraction peaks

Sample	weight % amorphous
CHS-10	100
CHS-20	74
CHS-30	43
CHS-40	25
CHS-50	12
CHS-60	5
CHS-70	3
CHS-80	3
CHS-90	2
CHS-100	0

X-ray diffraction peak broadening was measured for phase-II and phase-III in the composite. FWHM of the phase-II values is larger than phase-III by ~300%. It is another indicator of the interaction between CsHSO$_4$ and SiO$_2$. Notably, the broadening is limited to phase-II, compared to pure phase materials, as evident in Figure 5-8, in which the FWHM at 40 °2Θ is plotted as a function of composite composition for both phases.
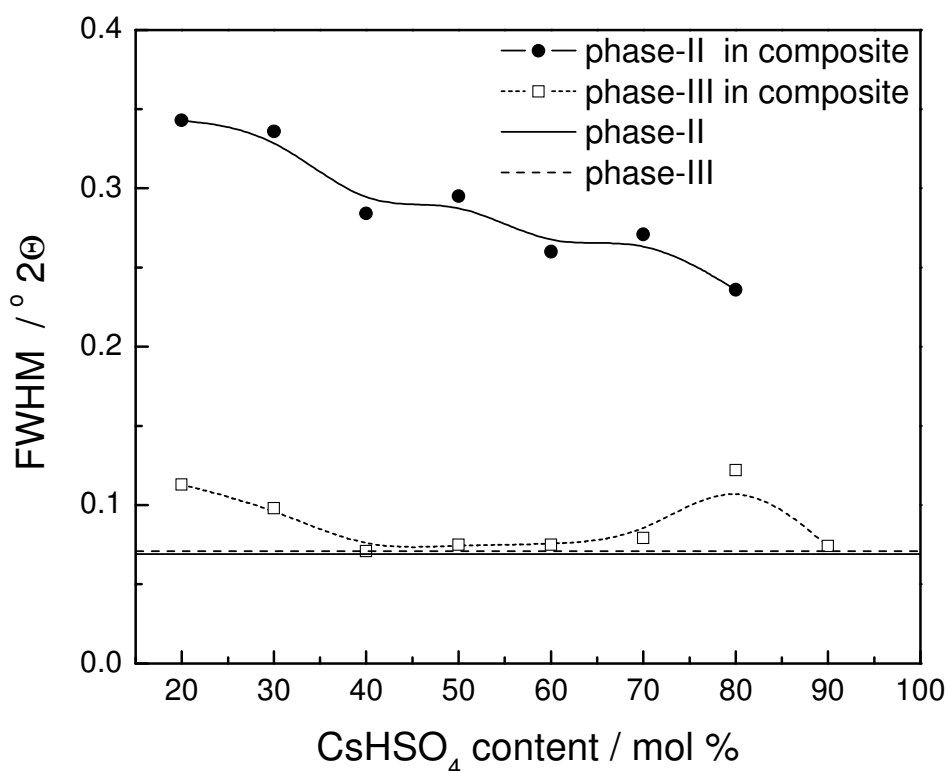
Figure 5-8 Full-width half-max of the diffraction peak effectively at 40 ° 2Θ for both phases of CsHSO$_4$ in the composites. The values for neat CsHSO$_4$ are shown as straight lines for comparison

Peak broadening has been previously reported in the literature on such composite systems[15],[16]. The effect has been generally attributed to the amorphization of the solid acid phase. What is noteworthy here is that the broadening occurs in addition to the amorphization that causes a reduction in the peak intensities from the CsHSO$_4$ crystalline phases and is responsible for the broad 'hump' loosely centered at 24 °2Θ. That is, the analysis above implies an amorphous phase that is plausibly independent of structural modifications to crystalline CsHSO$_4$. The broadening is attributed to a size effect rather than a disordering. The mean particle diameters implied by the Scherrer equation[17], after

taking into account instrumental broadening effects, are 35-45 nm for the crystallites of phase-II (and large particles for phase-III).

5.6 Phase transformations in 25-150^0 C

Another important question is how oxides additives affect phase transitions in solid acids and in CsHSO$_4$ in particular. As mentioned above, the magnitude of the conductivity discontinuity otherwise observed at the superprotonic transition is substantially lowered[2,5,6,7,8,9] and the existence of the superprotonic phase at temperatures below 141^{0}C was proposed. But no direct diffraction evidence was provided and it was not mentioned if the effect is kinetic or thermodynamic in origin. This work will study the phase behavior of the solid acids composites in the 25-150^{0}C temperature range.

In-situ high temperature X-ray diffraction was chosen as a major analytical tool of that work. This method allows us to quantitatively monitor phase existence at various temperatures. Powder samples of the CHS-10,30,40,50,60,70,90 were used. Heating rate was 1^{0}C/min and X-ray diffraction patterns were taken with the increment of 5-10^{0}C on heating and cooling for 10 to 70 degrees 2 theta and one minute delay before pattern collection. Collection time of one pattern was 15 minutes, which corresponds to 30s/step 2 theta. The combination of the slow heating range and long collection time within different temperatures allows us to study material close to equilibrium. It is interesting to note that solid-solid phase transformation in CsHSO$_4$ between high and low temperature phase usually takes less than a minute, while our timeline was 1-2 orders of magnitude longer.

5.6.1. Thermogravimetric study of the phase transformations in $CsHSO_4$ composites

The Thermogravimetric (TG)-Differential Scanning Calorimetry (DSC) measurements were performed with 1^0/min heating rate on the entire composite series. We can immediately see that transformation to high temperature phase occurs in composites CHS-30 to CHS-90 at an almost constant temperature of 139-141^{0}C.
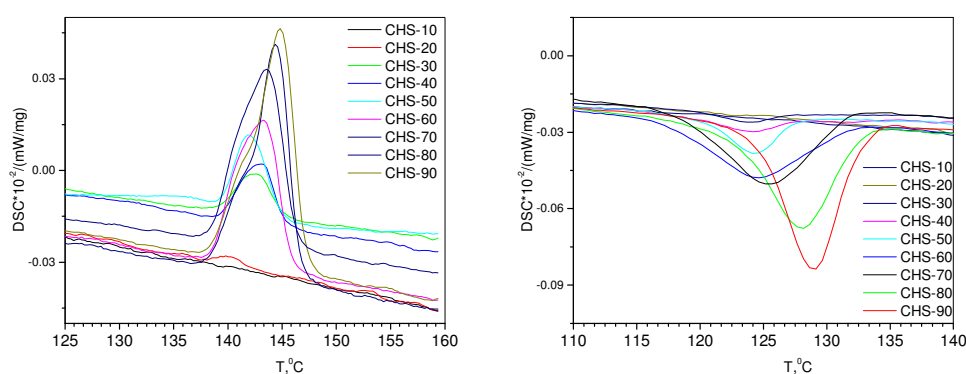
Figure 5-9 DSC data for all $CsHSO_4$-SiO_2 composites on heating (left) and cooling (right)

The situation is dramatically different for the cooling cycle – for high $CsHSO_4$ content samples, like CSH-90 tetragonal-monoclinic transformation starts at around 135^{0}C, which is consistent with pure $CsHSO_4$ measurements. But with increase of the silica in the material, transformation shifts to lower temperatures to 125^{0}C for CHS-30. The area of the peak can provide information about the thermal effects of the transformation. The summary of the thermal data is shown in Table 5-4.

Thermogravimetric analysis shows that all weight loss in composites occurs at temperatures up to 100^0C, suggesting the loss of the absorbed water. No mass loss above 100^0C suggests absence of the dehydration of the solid acid material. The amount of the weight loss is increasing with the increase of the amorphous SiO_2.

Table 5-4 Summary of the TG-DSC analysis of the composites

Composite	Weight% CsHSO4	J/g		Weight Loss,%
		Heating	Cooling	
CHS-90	0.972	20.4	-16.6	1.0
CHS-80	0.939	19.9	-16.0	2.1
CHS-70	0.899	16.7	-13.9	3.0
CHS-60	0.852	14.0	-11.5	3.8
CHS-50	0.793	5.2	-3.9	5.0
CHS 40	0.719	4.3	-1.9	6.4
CHS 30	0.621	3.4	-0.93	6.9
CHS 20	0.489	0	0	9.9
CHS 10	0.298	0	0	10.1

High differences between peak areas on heating and cooling for CHS-50,40,30 suggests that not all material transforms at that temperature range. The detailed transformation behavior will be studied later by in-situ high temperature X-ray diffraction techniques.

5.6.1. Diffraction study of the phase transformations in $CsHSO_4$ composites

CHS-10 composite showed no diffraction peaks at low temperatures despite 30 weight % of $CsHSO_4$ in it. First question we would like to know is if amorphous material will recrystallize into the superprotonic phase or recrystallize back to phase-II or phase-III of the $CsHSO_4$. You can see diffraction patterns on heating (Figure 5-10) and cooling (Figure 5-11).
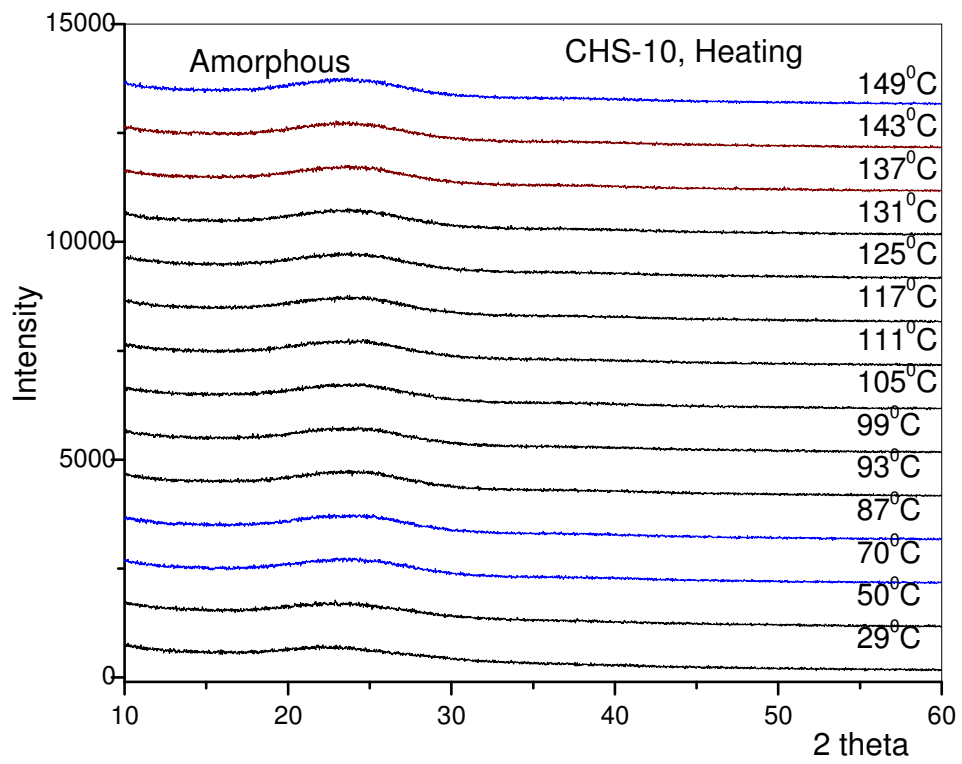
Figure 5-10 CHS-10 composite diffraction patterns on heating between 29 and 149^{0}C
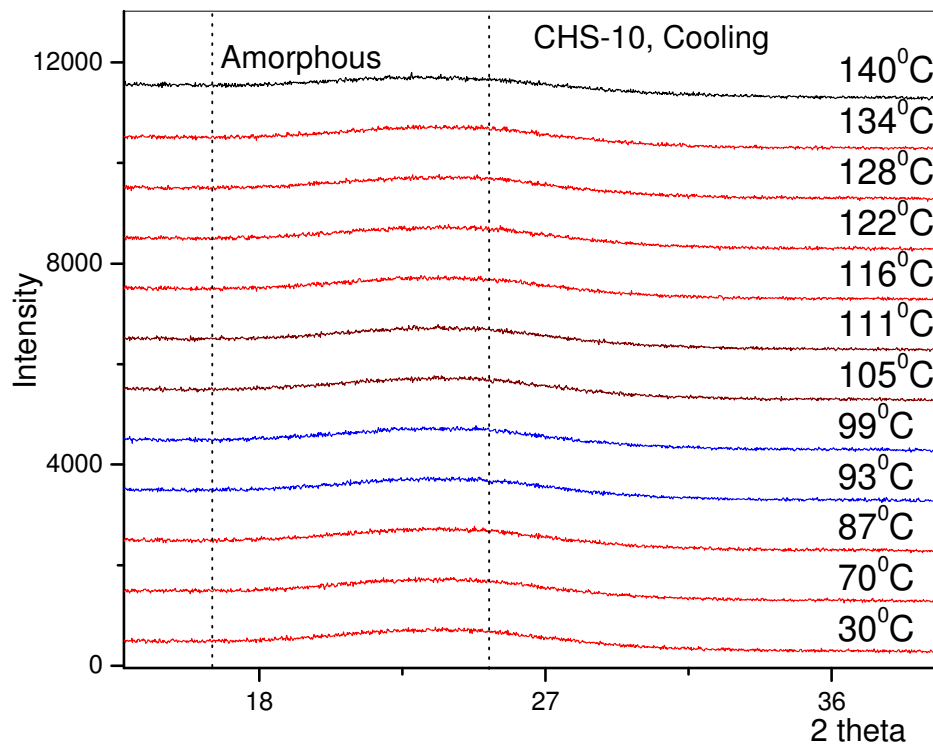
Figure 5-11 CHS-10 composite diffraction patterns on cooling between 29 and 149^{0}C

Absence of any phase transformations in diffraction patterns shows that the composite material is stable under heating and cooling conditions.

Similar experiments were performed for other compositions of the composites (CHS-30,40,50,60,70,90). Typical phase transitions behavior is shown in Figure 5-12 and Figure 5-13 for selected compositions.
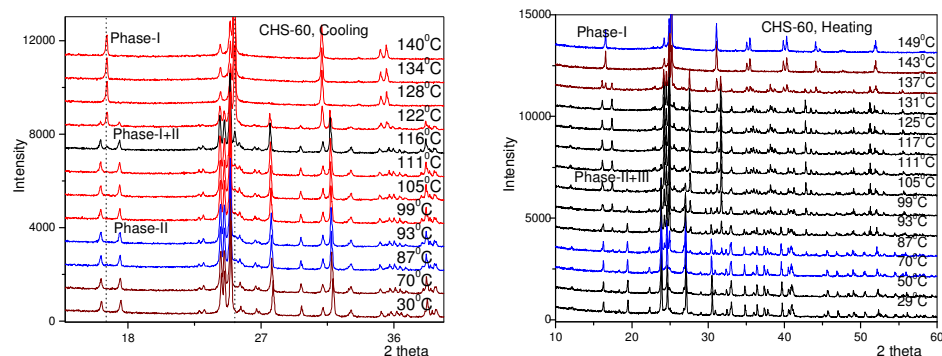
Figure 5-12 Diffraction patterns of the CHS-60 composites on heating (right) and cooling (left). Different color represents different phases – Blue –phase-I, Red-Phase-I+II, Black-Phase-II+III, Purple-Phase-II
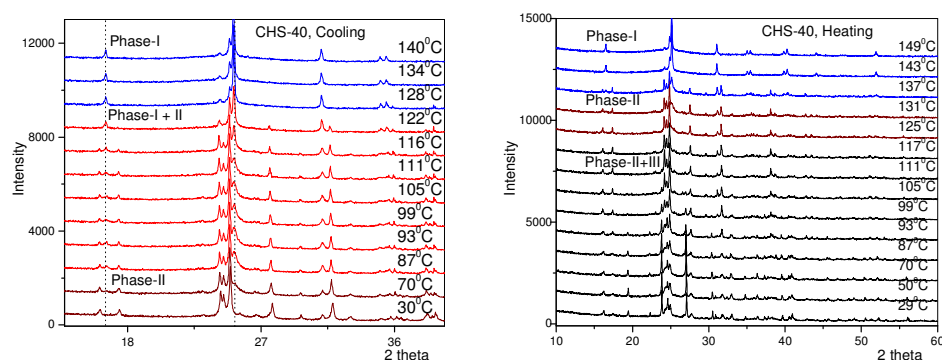
Figure 5-13 Diffraction patterns of the CHS-40 composites on heating (right) and cooling (left). Different color represents different phases – Blue –Phase-I, Red-Phase-I+II, Black-Phase-II+III, Purple-Phase-II

CHS-90 is very close to the pure phase $CsHSO_4$. For graphical representation of the phase content, each temperature X-ray pattern was refined using the Rietveld method. The structures reported by Chisholm[18] and by Itoh[19] and by Merinov[20] for phases II, III and I respectively, were used as starting models.

CHS-30,40,50,60,70,90 composites were analyzed by the following Rietveld diffraction method.

The following parameters were refined for all phases:

- Lattice parameters and scale factor.

- Overall isotropic atomic displacement parameter and site occupancies.

- Peak profiles, $\Gamma = (W + U*\tan^2\theta + V*\tan\theta)^{1/2}$ (3 refined parameters per phase)

- 4 background parameters and zero shift parameter

- preferred orientation parameter (modified Bragg intensity $P_k = \exp(P_1*a_k^2)$), where a_k is the acute angle between the scattering vector and the normal to the crystallites (1 parameter per phase).

Scale factors for the phases directly yield the relative amounts of phases II, III and I in each of the composites. It is possible to plot phase composition vs. temperature for all the composites and temperatures, resulting in phase transitions diagram. Three phase existence diagram for CHS-90 is shown on Figure 5-14.
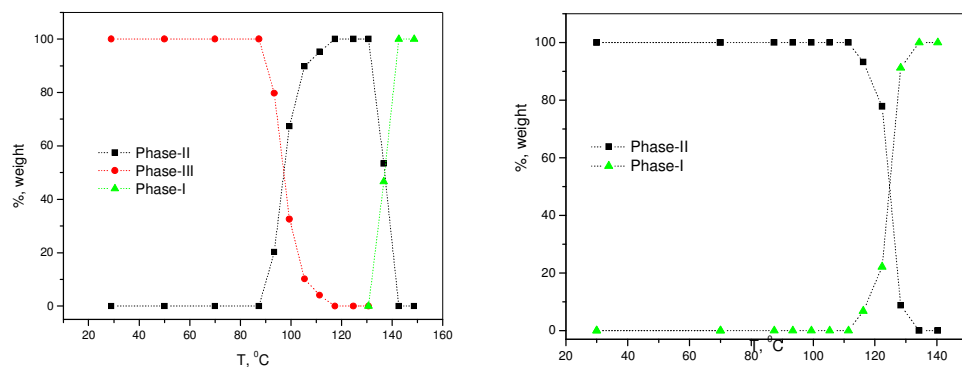
Figure 5-14 Phase existence diagram for CHS-90 composites, based on Rietveld refinement of the high temperature diffraction data. Heating (left) and Cooling (right)

Phase behavior on heating is shown below for selected composites. Silica causes stabilization of the phase-II at room temperature, with increase of the amount with SiO_2 increase, but significant phase-III-phase-II transformation occurs below 90^0C. We can see the transition on heating from phase-III to phase-II occurs at $90-120^0C$ and from phase-II to phase-I from $130-140^0C$, regardless of the composite fractions. The temperature range of phase transformations on heating for other composites is similar to the CHS-90 (see Figure 5-15).
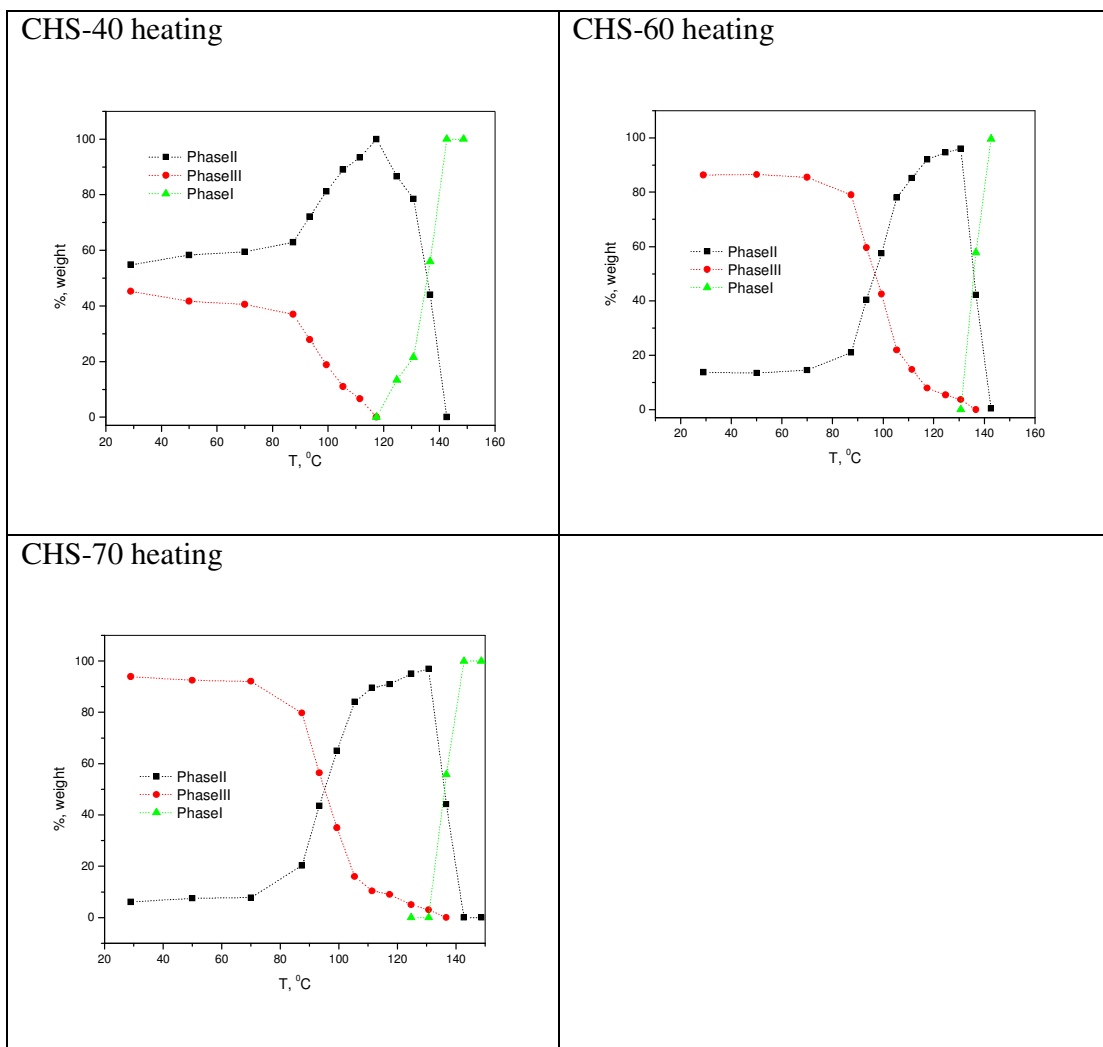
Figure 5-15 Examples of the phase transition diagrams for CHS-40, CHS-60 and CHS-70

Dramatically different behavior was observed on cooling. Temperature of the transition from superprotonic phase-I to phase-II strongly depends on the composition of the material (Figure 5-16).
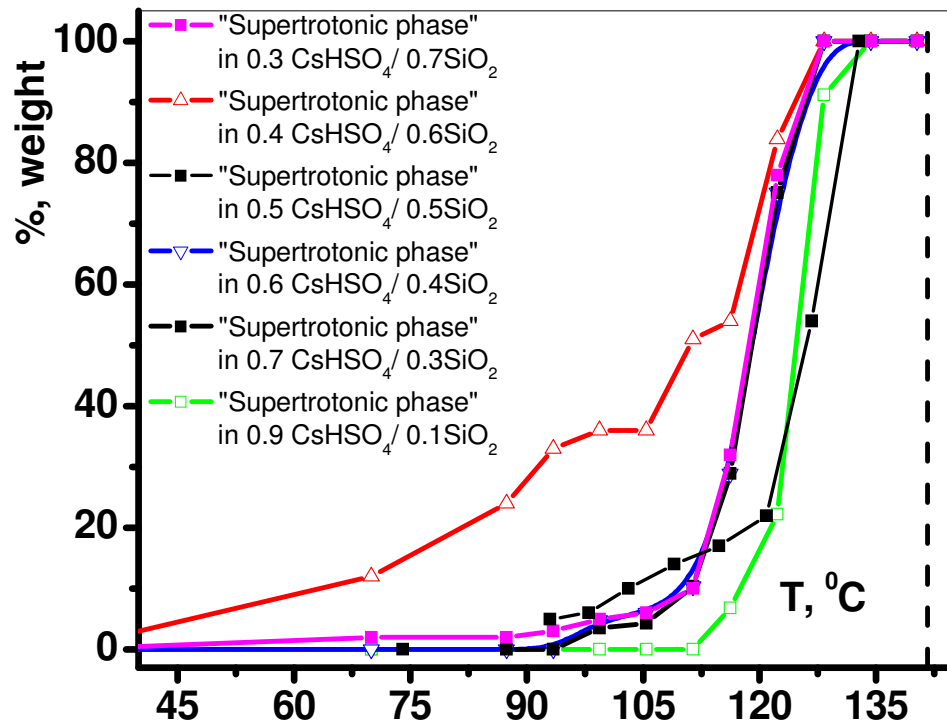
Figure 5-16 Superprotonic phase stabilization in composites on cooling. Maximum stabilization occurs in CHS-40 and shifts the end of the transformation temperature down to 70^{0}C

Reverse transformation of the CHS-90 composite is completely over at around 110^{0}C. With the increase of the silica in the system, the phase-II amount is still very significant at 110^{0}C. Maximum stabilization occurs in CHS-40 and shifts the end of the transformation temperature down to 70^{0}C. Somewhat unexpected, CHS-30 behaves

similar to the CHS-70 and does not have stabilized phase-I below 90^0C. That finding

explains the conductivity behavior studies from direct stabilized phase-I observation, for

the first time.

An equally important question regarding composite evolution during heating is

whether or not amorphous material recrystalizes back into the phase-II or phase-I in

CHS-20 to CHS-90 compositions. To test this hypothesis peak intensity of the crystalline

fraction of the systems were measured at the beginning of the experiment and after

heating up to 150^0 and cooling back down (Figure 5-17, Figure 5-18).
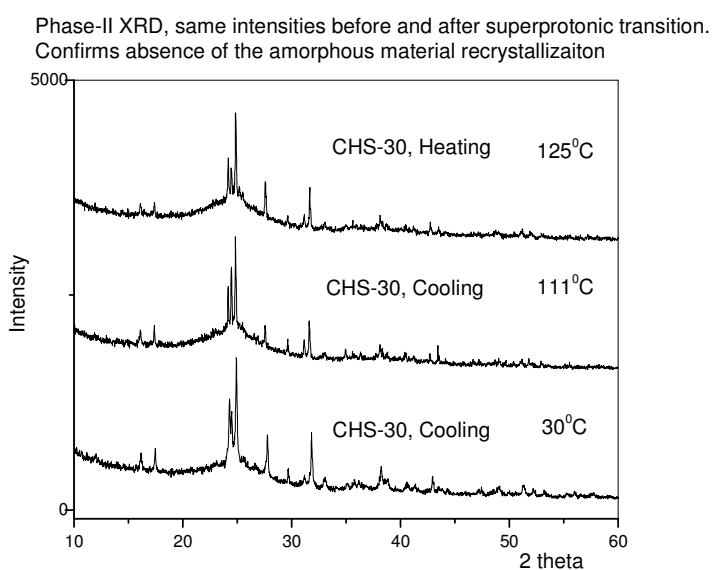
Figure 5-17 X-ray diffraction pattern of the CHS-30 composites at 125^0C on heating

and 111^0C 30^0C on cooling. Integrated intensities of the crystalline phases are equal
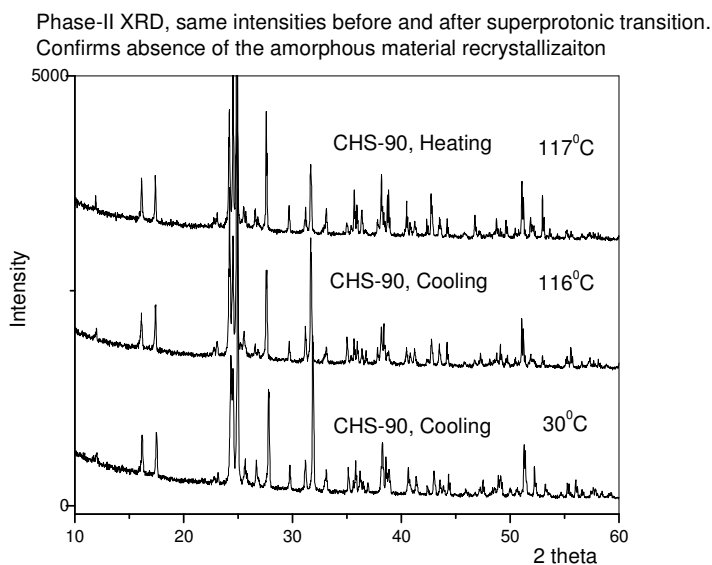
Figure 5-18 X-ray diffraction pattern of the CHS-90 composites at 117^{0}C on heating and 116^{0}C 30^{0}C on cooling. Integrated intensities of the crystalline phases are equal

Equality of the integrated intensities proves that there is no recrystallization of the amorphous phases of CsHSO$_4$ during phase transformations to high temperature superprotonic phase and back.

5.7. Conclusion

The influence of nanoparticulate SiO$_2$ on the crystallization behavior of CsHSO$_4$ from aqueous solution has been quantitatively evaluated.

X-ray diffraction method for quantitative analysis of the amorphous phases is developed. From X-ray analysis, it is shown that SiO$_2$ induces amorphization of a portion of the CsHSO$_4$ and the crystallization of the otherwise metastable phase II. While both amorphization and the occurrence of phase II in such composites have been previously suggested in the literature[21], the extent has not previously been fully quantified, nor have

the phenomena been observed for non-porous SiO_2. Thus, the interaction between $CsHSO_4$ and SiO_2 has a chemical rather than mechanical origin and, furthermore, does not require high temperature treatment to occur. The phase distribution was found to be stable for over one year, indicating the strength of the stabilization effect that SiO_2 has on phase II of $CsHSO_4$.

The overall microstructural picture that emerges from these studies is a system in which SiO_2 particles are covered with an amorphous coating of $CsHSO_4$-like material, in turn, covered by nanoscale phase-II, which then coexists with independently nucleated particles of phase-III.

"phase-II" + amorphous $CsHSO_4$
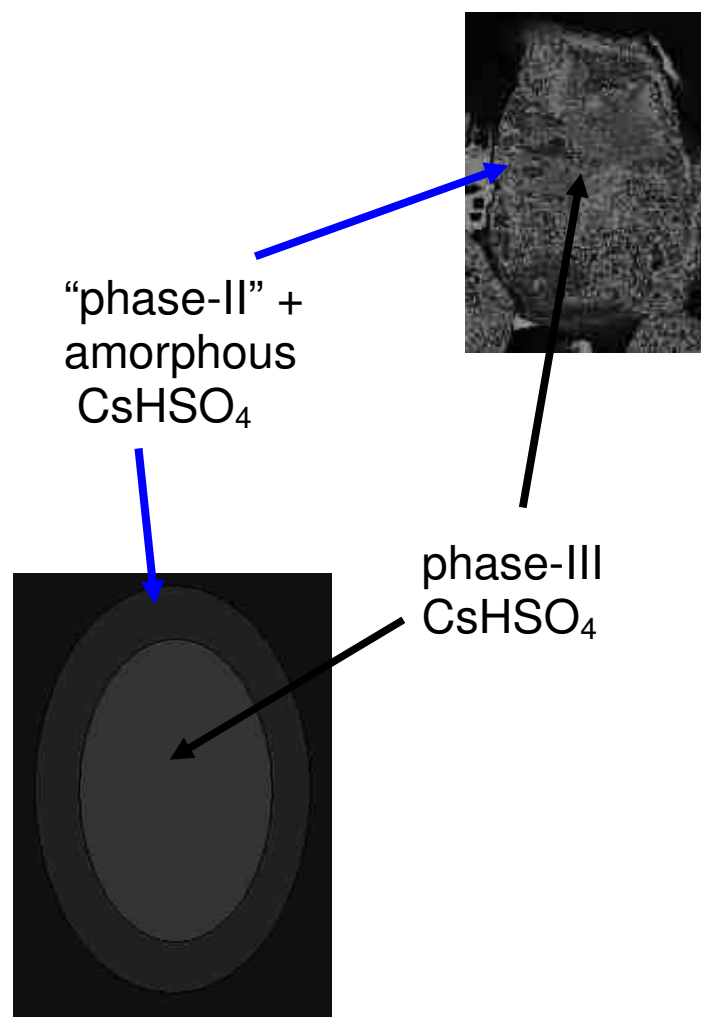
phase-III $CsHSO_4$

Figure 5-19 Schematic of the phase distribution in CsHSO$_4$ – SiO$_2$ composites. Phase-II size is 30-40 nm, while Phase-III particles are micrometers in size.

In composites with small molar fractions of CsHSO$_4$, the entirety of the acid salt is consumed in the amorphous layer. As the amount of CsHSO$_4$ is increased, 'normal' precipitation of phase-III competes with incorporation of CsHSO$_4$ into the amorphous phase, and it is only when the CsHSO$_4$ content exceeds a certain threshold that the CsHSO$_4$-II is observed. At high CsHSO$_4$ content, the extent of amorphization becomes negligible as does the extent of crystallization in metastable phase II.

Upon heating, composites CHS 30-90 transform into the superionic phase-I CsHSO$_4$ at temperatures of 135-141^0, independent of composition, no phase transitions were observed for CHS-10. On cooling we observe dramatically different behavior. Superionic phase stabilization occurs in composite materials, with the maximum in CHS-40. No recrystallization of the amorphous material was observed after heating past superprotonic transition temperature.

References

[1] Otomo, J.; Wang, S. Q.; Takahashi, H.; Nagamoto, H. *J. Membr. Sci.* **2006**, *279*(1-2), 256-265.

[2] Ponomareva, V. G.; Shutova, E. S. *Solid State Ionics* **2007**, *178*(7-10), 729-734.

[3] Otomo, J.; Shigeoka, H.; Nagamoto, H.; Takahashi, H. *J. Phys. Chem. Solids* **2005**, *66*(1), 21-30.

[4] Shigeoka, H. ; Otomo, J.; Wen, C. J.; Ogura, M.; Takahashi, H. *J. Electrochem. Soc.* **2004**, *151*(10), J76-J83.

[5] Ponomareva, V. G.; Shutova, E. S. *Solid State Ionics* **2005**, *176*(39-40), 2905-2908.

[6] Ponomareva, V. G.; Lavrova, G. V. *Solid State Ionics* **2001**, *145*(1-4), 197-204.

[7] Ponomareva, V. G.; Lavrova, G. V.; Simonova, L. G. *Solid State Ionics* **1999**, *119*(1-4), 295-299.

[8] Ponomareva, V. G.; Lavrova, G. V. *Solid State Ionics* **1998**, *106*(1-2), 137-141.

[9] Ponomareva, V. G.; Uvarov, N. F.; Lavrova, G. V.; Hairetdinov, E. F. *Solid State Ionics* **1996**, *90*(1-4), 161-166.

[10]IUCR *Powder Diffraction* **1997** , *22*(21).

[11] Hill, R. J.; Howard, C. J. LHMP1 Program: ANSTO Report M122 Lucas Heights Research Laboratories: Australia, 1986.

[12] Chisholm, C. R. I.; Haile, S. M. *Mater. Res. Bull.* **2000**, *35*, 999-1005.

[13] Itoh, K.; Ukeda, T.; Ozaka, T.; Nakamura, E. *Acta Cryst.* **1990**, *C46* 358-361.

[14] *The Rietveld Method*; Young, R. A., Ed.; International Union of Crystallography; Oxford Science Publications: Oxford, 1993; p 22.

[15] Shigeoka, H. ; Otomo, J.; Wen, C. J.; Ogura, M.; Takahashi, H. *J. Electrochem. Soc.* **2004**, *151*(10), J76-J83.

[16] Ponomareva, V. G.; Uvarov, N. F.; Lavrova, G. V.; Hairetdinov, E. F. *Solid State Ionics* **1996**, *90*(1-4), 161-166.

[17] *X-Ray Diffraction Procedures for Polycrystalline and Amorphous Phases*, 2nd ed.; Klug, H. P.; Alexander, L. E.; John Wiley and Sons: New York, 1974; p 656.

[18] Chisholm, C. R. I.; Haile, S. M. *Mater. Res. Bull.* **2000**, *35*, 999-1005.

[19] Itoh, K.; Ukeda, T.; Ozaka, T.; Nakamura, E. *Acta Cryst.* **1990**, *C46* 358-361.

[20] Merinov, B.V. (1997) Kristallografiya 42, 906-917 Localization of hydrogen atoms in protonic conductors with a dynamical disordered network of hydrogen bonds: Effect of anonalous manifestation of hydrogen atoms on electron-density maps

[21] Burgina, E. B.; Ponomareva, V. G.; Baltahinov, V. P.; Kostrovsky, V. G. *Journal of Structural Chemistry* **2005**, *46*(4), 608-618.

Chapter 6. Proton mobility study by NMR in CsHSO$_4$/SiO$_2$

6.1 Introduction

Nuclear Magnetic Resonance (NMR) is an excellent technique to study both crystalline and amorphous materials. The brief introduction to the method will be given, with the emphasis on spin relaxation behavior. The method based on Zeeman effect of nuclei's energies splitting into several levels. If magnetic field is in the z-direction spin experience force of the $F=\mu\times B_0$, causing the precession around the z-axis with the corresponding frequency $\omega_0=\gamma*B_0$ called Larmor frequency. (μ=magnetic moment, γ-gyromagnetic ratio.(Figure 6-1) A ^{1}H nucleus has spin of ½ and has only two states under the external magnetic field.
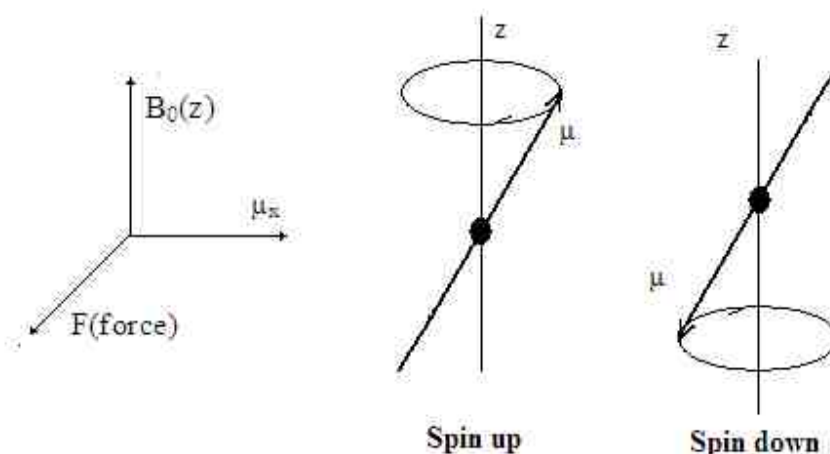
Figure 6-1 Spin precession in the magnetic field

The tendency towards Spin up precession in the presence of the magnetic field B_0 is defined by exponential Boltzmann's law and spin up state will be more energetically

favorable. If we sum all of the independent of each other precessing spins in the sample, the overall magnetization will be non-zero and aligned along z-axis, M(z). In the actual NMR experiment second fluctuating magnetic field B_1 at the Larmor frequency is applied along y-axes. Energy transfer between B_1 and nuclei spins is now possible. Absorption of energy occurs when +1/2 to -1/2 and emission when -1/2 to +1/2. Since we started with the excess +1/2 spins, we observe overall absorption of energy of the fluctuating B_1 field and that can be measured.

Since B_1 is a magnetic field, it also creates the force on a magnetization, perpendicular to applied field, causing the overall magnetization to rotate around x axis. That is resulting in correlating initially randomly rotating individual spins with the rotation of the B_1 magnetic field. The angle we rotate initial polarization is called pulse angle. After we turn off B_1 pulse when overall magnetization is along x-axis, we can observe two separate processes:

1. Under influence of the B_0, M_z component will increase return to equilibrium values at the rate determined by T_1. Increasing of the M_z towards equilibrium will require dissipation the excess energy to the surroundings. Rate constant T_1 is called spin-lattice relaxation time and describes effectiveness of the interaction between spin and surroundings. That process determines the mechanism of T_1 relaxation.

2. We also observe (Figure 6-2) that after applying B_1 field all spins are "bundle" together, causing M_x and M_y have non-zero values. Since equilibrium values of M_x and M_y are zero, process of returning then to zero called spin-spin relaxation. That process does not require net energy change

and one of the mechanisms involves simultaneous change of one spin from +1/2 to -1/2 state and other for -1/2 to ½. Repetition of that process will cause randomization of the spins with time constant T_2 (spin-lattice relaxation time).
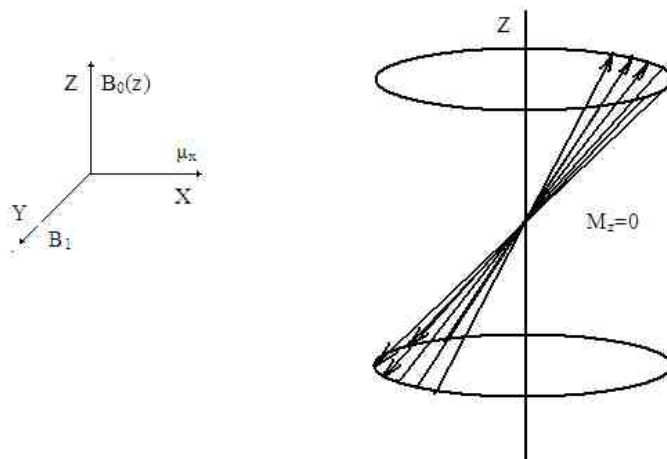
Figure 6-2 Schematic of spins states after applying B$_1$ oscillating magnetic field

In order for a nuclear spin to change orientation it has to give up $2\mu B_0$ of energy. The rate of M_z magnetization build up depends on energy transfer rate to translational, rotational or vibrational energy levels. The probability of the spontaneous emission depends on 3rd order of the frequency and very small for NMR[1]. Therefore, all NMR transitions must occur through nuclei interaction with the oscillating at its Larmor frequencies fields. Here are several examples of the possible mechanisms:

- Presence of the paramagnetic impurities.

- Atomic and molecule motion (rotation and translation) in non-metallic samples. Molecule movement generates randomly varying field at the site of the nucleus. In rigid lattice limit with slow reorientation frequency $w_0*t>>1$, $1/T_1 \sim H_0^{-2}$.

- Chemical shift anisotropy, due to the orbital effect of the nearby electrons $1/T_1 \sim H_0^2$.

Other mechanisms are usually field independent[1].

Techniques used for T_1 determination:

Saturation recovery sequence describes experiment of the magnetization recovery from zero after $\pi/2$ B_1 field pulse. It can be written as

$M_z(t) = M_0 (1-\exp(-t/T_1))$

t –waiting time before $\pi/2$ pulse.

Equation 6-1 Saturation recovery formula

Another method used in that work for T_1 determination is inversion recovery sequence. In that case π-$\pi/2$ sequence is used. The advantage of the method is that after the initial π sequence magnetization recovers over $2M_0$ range.

$M_z(t) = M_0 (1-2*\exp(-t/T_1))$

t –waiting time before $\pi/2$ pulse.

Equation 6-2 Inversion recovery formula

The spin-lattice relaxation time T_1 is defined only for exponential processes. For our purposes even if the relaxation time is not exponential, we are able to determine by that analysis how long do we have to wait for accurate spectra collection. In case of the non-exponential relaxation several adjustments can be made to formulas to fit experimental data and several adjustments can be made. Stretched exponential magnetization recovery function account for the possibility of the distribution of the relaxation times T_1[2].

$M_z(t) = M_0 (1-\exp(-t/T_1)^{\alpha})$

t –waiting time before $\pi/2$ pulse.

Equation 6-3 Stretched exponential magnetization recovery function

6.2 MAS Solid State NMR spectra of the pure phase-II and phase-III of CsHSO$_4$

The MAS (magic angle spinning) ^{1}H NMR spectra for CsHSO$_4$ phase II and phase III are shown in Figure 6-3. In both phases, there is a single crystallographically distinct proton site, and, accordingly, the NMR spectra each show a single peak. The peak is slightly broader for phase III than phase II, suggesting greater local anisotropy in the proton environment of phase-III. The chemical shifts are measured to be 11.02 and 12.35 ppm, respectively. These values correspond well to the reported correlation between the oxygen-oxygen distance in the hydrogen bond reported by Eckert *et al.*[3]:

$$\delta_{iso}/\text{ppm} = 79.05 - 0.255 \ (dO\text{-}H\ldots O)/\text{pm}$$
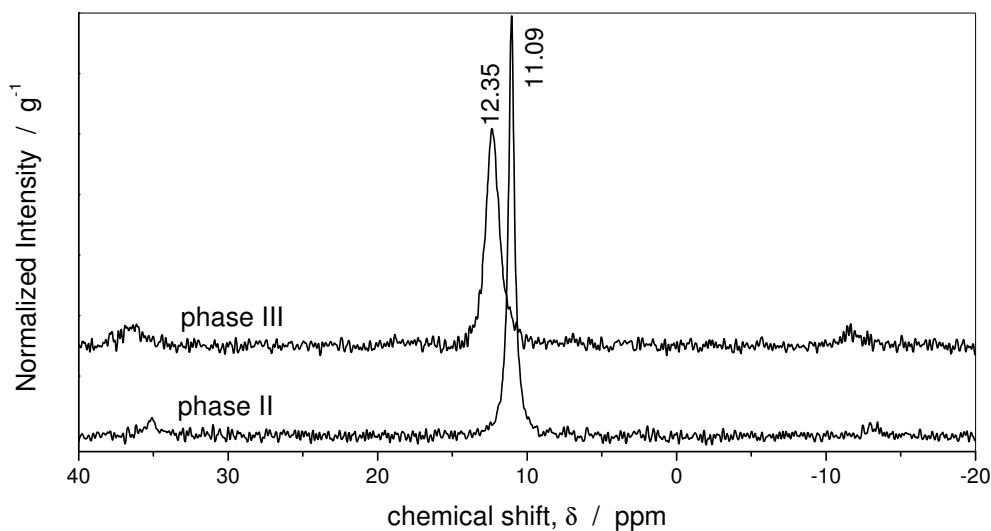
Figure 6-3 ^{1}H MAS NMR spectra for CsHSO$_4$; chemical shifts referenced to TMS. Peaks at chemical shifts of ~ 35 and ~ -12 ppm are spinning side bands

Chemical shifts of 11.9 and 13.9 ppm are expected for the crystallographic distances of 2.636 and 2.555 Å, respectively. That values suggests that phase-III lattice is much more rigid, with a stronger hydrogen bond, while phase-II has a weaker hydrogen bond and can have higher values of the proton mobility.

The integrated intensities from the two samples are equal within 1%, as expected from the identical chemical formulae. This result indicates that the pulse sequence and delay times employed are appropriate for quantitative phase analysis of the composites.

6.3 Measurements of the T_1 relaxation time for pure phases of $CsHSO_4$

Careful investigation of the correct spin-lattice relaxation time for phase-II and phase-III $CsHSO_4$ was carried out. Literature data analysis suggests T_1 value of at least on the order of tens of seconds for 25 to 200 MHz spectrometers. Since we operate at much higher frequencies (500 MHz spectrometer) and field dependence of the relaxation time is not known, careful T_1 measurements were taken. The following method was applied: one NMR spectra was taken with the increasing delay time. It was found that no significant rise of intensities was observed when the delay time was more than 3000 s. That gave us an approximate that T_1 value of around 600 s. (1/5 delay time) as commonly accepted in NMR measurements and describes ~96% spin relaxations, assuming exponential spin recovery. Example of the peak intensity increase with the increase of the delay time is shown in Figure 6-4.
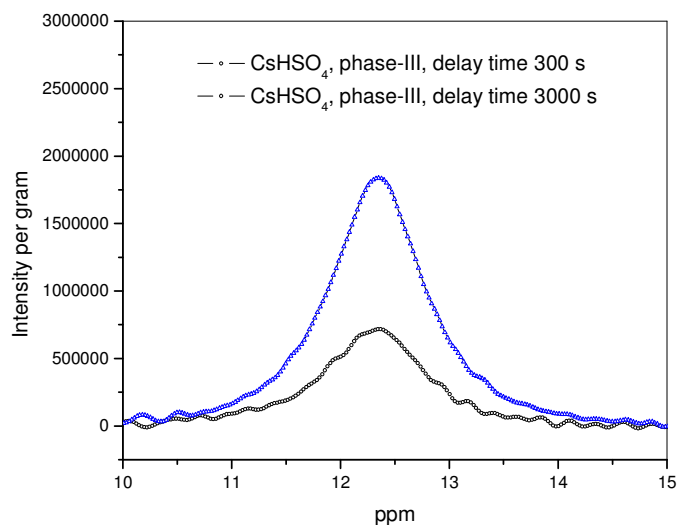
Figure 6-4 Phase-III CsHSO$_4$ NMR spectra with the delay time of 300 and 3000 s

After estimating phase-III relaxation time of around 600s, accurate measurement of the spin-lattice (T$_1$) relaxation times for pure phase-II and phase-III of CsHSO$_4$ was performed by inversion recovery methods.
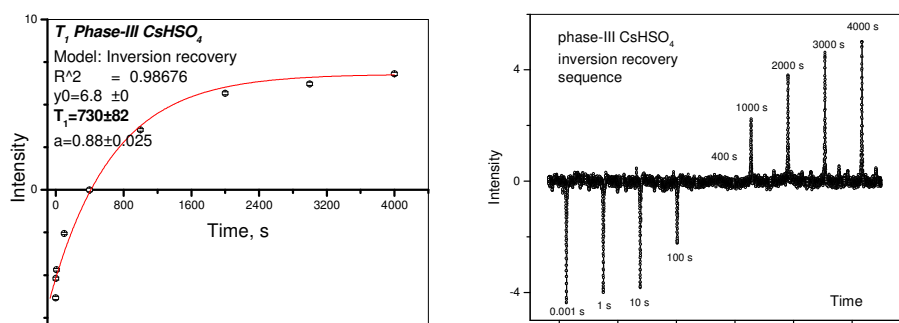
Figure 6-5 Inversion recovery method for T$_1$ determination in phase-III CsHSO$_4$.

Spin inversion recovery plot (right) and integrated area of the peak vs. time (left)
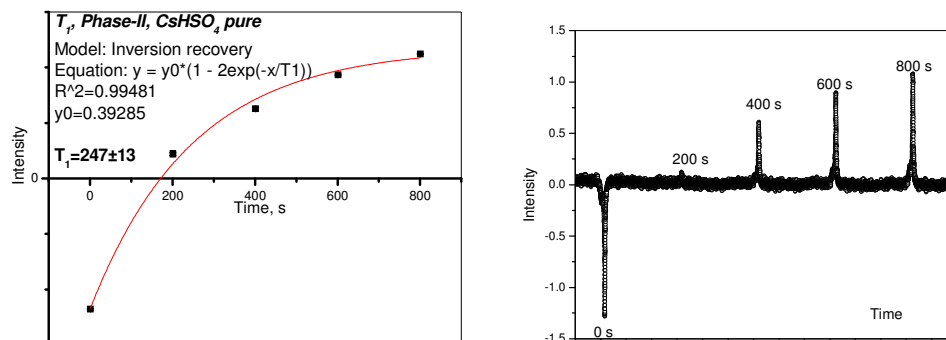
Figure 6-6 Inversion recovery method for T_1 determination in phase-II CsHSO$_4$. Spin inversion recovery plot (right) and integrated area of the peak vs. time (left)

The inversion recovery measurements (Figure 6-5 for phase-III and Figure 6-6 for phase-II) indicated T_1 relaxation times of 730±80s and 246±12s, for phases III and II, respectively in 500 MHz spectrometer. Inversion recovery method was used because it covers wider ($-M_z$ to M_z) spread of the magnetizations, potentially providing better accuracy.

Relaxation times are indeed quite long. Previous measurements of CsHSO$_4$ ~100s as reported by Mizuno *et al.*[4] at 200 MHz and 21 s by Damyanovich *et al.*[5] at 25 MHz spectrometer respectively.

Field dependence of the relaxation time can provide us information about the relaxation mechanism. Chemical shift anisotropy has $T_1 \sim H_0^{-2}$ field dependence while Atomic and molecule motion based mechanisms in low ion mobility regime ($w_0 * t \gg 1$) $T_1 \sim H_0^{2}$.

Mizuno *et al.* have estimated using BPP Equation 6-4 that, considering only dipolar contributions to the relaxation would lead to a T_1 of over 10^5 s at a field strength of 200 MHz (and a factor of ~ 6 increase in T_1 would result from the higher field of 500

MHz used here[4],[6] While measured T_1 values are much longer, the suggestion of combination of the dipole-dipole and mostly chemical shift anisotropy as a dominant mechanism of relaxations was made.

$$\frac{1}{T_1} = \frac{2}{3} M_{HH}^2 \left[\frac{0.5 * \tau_H}{1 + (0.5 * \omega_H * \tau_H)^2} + \frac{2 * \tau_H}{1 + (\omega_H * \tau_H)^2} \right] +$$

$$M_{CsH}^2 \left[\frac{0.5 * \tau_H}{1 + ((1 - \gamma_{Cs}/\gamma_H) * \omega_H * \tau_H)^2} + \frac{1.5 * \tau_H}{1 + (\omega_H * \tau_H)^2} + \frac{3 * \tau_H}{1 + ((1 + \gamma_{Cs}/\gamma_H) * \omega_H * \tau_H)^2} \right]$$

where $\tau\omega_H$ and ω_{Cs} are angular resonance frequencies of ^1H and ^{133}Cs, respectively. A mean residence time of H is τ_H. Only H is assumed to be mobile. M_{HH} and M_{HCs} are the second moments contributing to the relaxation and due to ^1H–^1H and ^1H–^{133}Cs dipole–dipole interactions, respectively.

Equation 6-4 Dipolar contribution ot spin-latitce relaxation according BPP theory[5],[7]

Detailed relaxation behavior of $CsHSO_4$ in phase-III was studied in[5]. Slow rotation of the HSO_4^- groups and different configuration of these groups creates glass-like features such as distribution of the T_1 values in phase-III. Although detailed discussion of the possible spin-lattice relaxation mechanisms is beyond the focus of this work, it is likely that these features as well as chemical shift anisotropy, due to the orbital effect of the nearby electrons and dipole-dipole interactions are among the possible mechanisms. Proper spectra collection is, on the other hand, critical to our goal of quantitatively extracting materials information. We used several techniques listed above to confirm that phase-III returns to the equilibrium around 700 s, so the delay time of 3000 s is sufficient for accurate data collection, regardless of the mechanism. Possibility of non-exponential relaxations in phase-III is observed, since the fluctuation of the pre-exponential factor β suggests either non-exponential contribution or non-uniform fields effects.

$M_z(t) = M_0 (1-2*\beta*exp(-t/T_1))$

t –waiting time before $\pi/2$ pulse.

$\beta=0.88\pm0.25$

Equation 6-5 Modified inversion recovery formula

Further proof of non-exponential behavior was observed while performing phase-III saturation recovery experiments with stretch exponential fitting. That gave us the value of $\alpha=0.37\pm0.04$ and $T_1=730\pm80$. Phase-II T_1 relaxation time is described well assuming exponential behavior in all cases.

6.4 MAS Solid State NMR spectra of the CsHSO$_4$/SiO$_2$ composites

^{1}H MAS Solid State NMR spectra of the composites are shown in Figure 6-7. Proton peaks occur at chemical shifts corresponding precisely to the two phases of CsHSO$_4$, and showing broader peak for phase III. That is consistent with pure phase-III NMR, suggesting rigid hydrogen bonds, compared to phase-II.

The peak intensity for phase II is decreasing with increasing SiO$_2$ content consistent with the X-ray powder diffraction data. Additional peaks in the vicinity of 5 to 7 ppm is due to surface water absorbed on SiO$_2$/amorphous CsHSO$_4$. 10 nm SiO$_2$ alone has a much broader peak at around 5 ppm. The peak at 6.5-7 ppm moves towards more acidic values and reaches maximum at CHS-50 composition and then moves to the less acidic (lower chemical shift) values. The peak intensity generally increases with increasing SiO$_2$ content, consistent with the diffraction data analysis and TGA data of the composites.
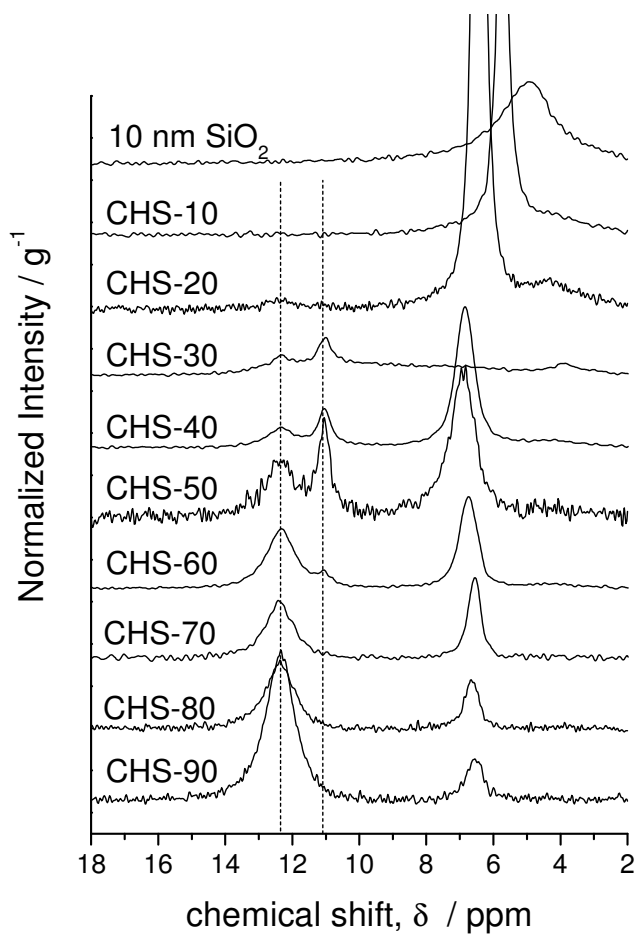
Figure 6-7 ^{1}H MAS NMR spectra for CsHSO$_4$ – SiO$_2$ composites and pure SiO$_2$. Chemical shifts referenced to TMS. Lines indicate chemical shift values of 12.35 and 11.02 ppm, corresponding to phases III and II, respectively, of crystalline CsHSO$_4$

On the other hand, peaks at 11.02 and 12.35 ppm correspond to crystalline phases, do not change their position as silica content rises.

NMR spectra of the CHS/SiO$_2$ composites were fitted with two Gaussian functions in order to determine the ration between phase-II and phase-III. Figures of the fittings are shown below. The relative amounts of the two phases implied by the

integrated NMR peaks precisely, to the relative amounts of these two phases implied by

the diffraction analysis, Figure 6-9.
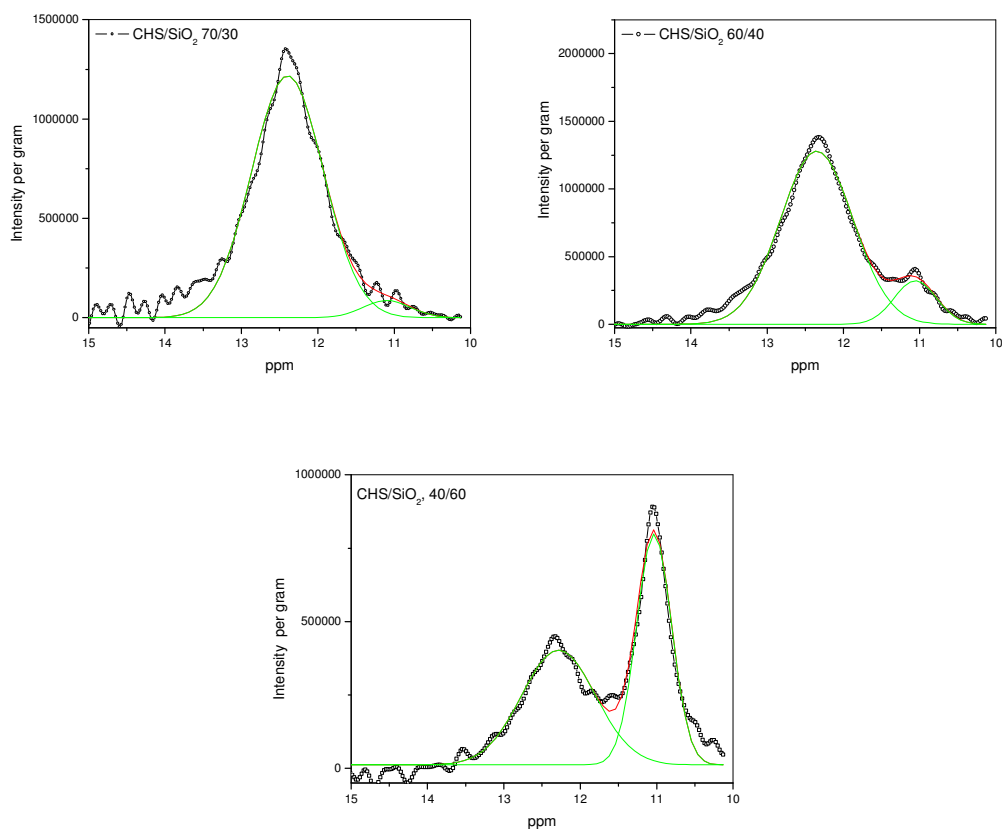
**Figure 6-8 Fitting phase-II and phase-III NMR peaks in composites gives us the
relative amount of phases, which is in excellent agreement with Rietveld refinement
data**

Phase-II/Phase-III ratio calculation in composites by the XRD and NMR methods

is shown in Figure 6-10. Both methods produce identical results.
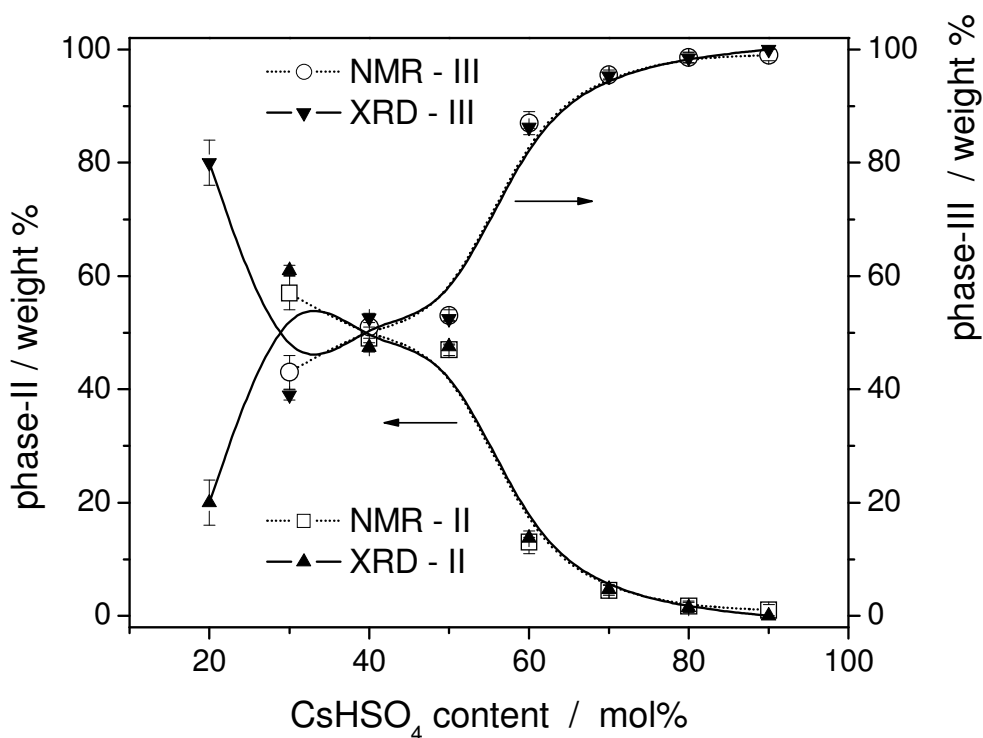
Figure 6-9 Relative amounts of phases II and III in the crystalline portion of CsHSO₄ within the CsHSO₄-SiO₂ composites; comparison of the results obtained by XRD (Rietveld refinement) and by NMR (ratio of integrated peak intensities). For CHS-20, the quantity of crystalline CsHSO₄ is low, and only the XRD estimate is included

In the case of the CHS-20 sample, it is apparent that, despite the low quantity of the crystalline phase and hence high uncertainty in the results, the amount of phase III exceeds that of phase II (as in the case of the XRD data).

An important conclusion is that although silica stabilizes phase-II in the composites, the position of the peak (which is related to the strength of the hydrogen bond) remains practically unchanged.

6.5 Measurements of the T_1 relaxation in $CsHSO_4/SiO_2$

Inversion or saturation recovery method was used to find T_1 relaxation times in composites. Due to phase-II stabilization in composites, T_1 for phase-III and phase-II needs to be found. Phase-III relaxation time is found to be the same in all composites as in pure phase-III material. An example of the precise determination is shown in Figure 6-10 for CHS-60.
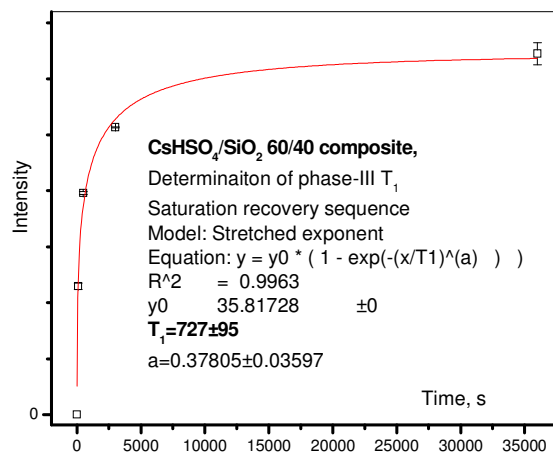
Figure 6-10 T_1 measurements in CHS-60 for phase-III

Relaxation times of the metastable phase-II were measured in composites with significant fraction of that phase (CHS-30 to CHS-60). It was found that relaxation time was dramatically different: between 100 to 170 ms, compared to 250 s for pure phase-II, representing more than 3 orders of magnitude decrease. Relaxation time experience exponential recovery in both cases and was fitted in inversion recovery equation. Examples of CHS-30 and CHS-60 measurements are shown on Figure 6-11.
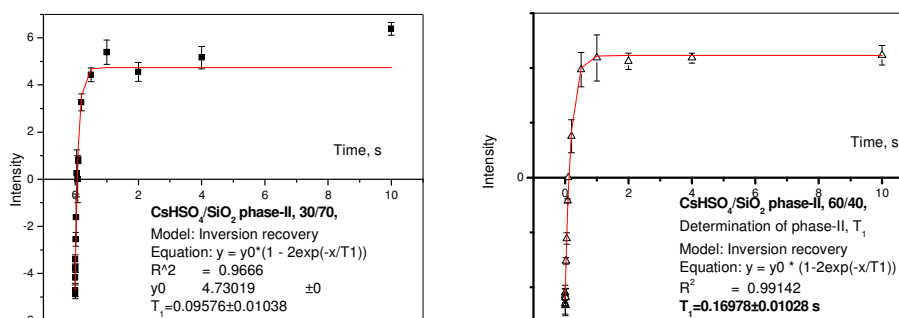
Figure 6-11 Example of T_1 measurements in CHS-30 and CHS-60 for phase-II

It is interesting to note that 6.5-5 ppm peak's relaxation time was on the order of 90 ms. That suggests extremely effective relaxation mechanism in the composites due to silica. Absorbed water has a similar relaxation time. Possible reasons for the relaxation time decrease based on our hypothesis is proposed. Due to the strong chemical and physical interaction between 30-40 nm phase-II with amorphous $CsHSO_4$/silica, ion movement in the system decrease the relaxation time of phase-II to the values observed in pure silica or amorphous $CsHSO_4$. Fast proton exchange between phase-II hydrogen ions and surrounded amorphous $CsHSO_4$ with SiO_2 and absorbed water is possible.

Dramatic decrease of the phase-II relaxation, while phase-III relaxation time remains constant further solidifies our hypothesis on the effect of the silica in the system. 10 nm SiO_2 particles serve as the nucleation site for $CsHSO_4$ precipitation. The material in direct contact with the SiO_2 is amorphized; when in contact with the amorphous solid acid adopts the phase-II crystalline structure and grows to dimensions of only 30-40 nm (as either isolated particles or a continuous layer). Simultaneously, $CsHSO_4$ that precipitates from the solution independent of the influence of the SiO_2 adopts the usual

phase-III crystalline structure and grows to macroscopic dimensions, typical of precipitation in the absence of SiO_2.

6.6. Spin-lattice relaxation behavior in surface-stabilized metastable materials as a method to study surface interactions in solid acids. Phase and microstructure evolution study based on solid state NMR

Based on NMR and X-ray diffraction results, suggested microstructure of the composites is shown in Figure 6-12.
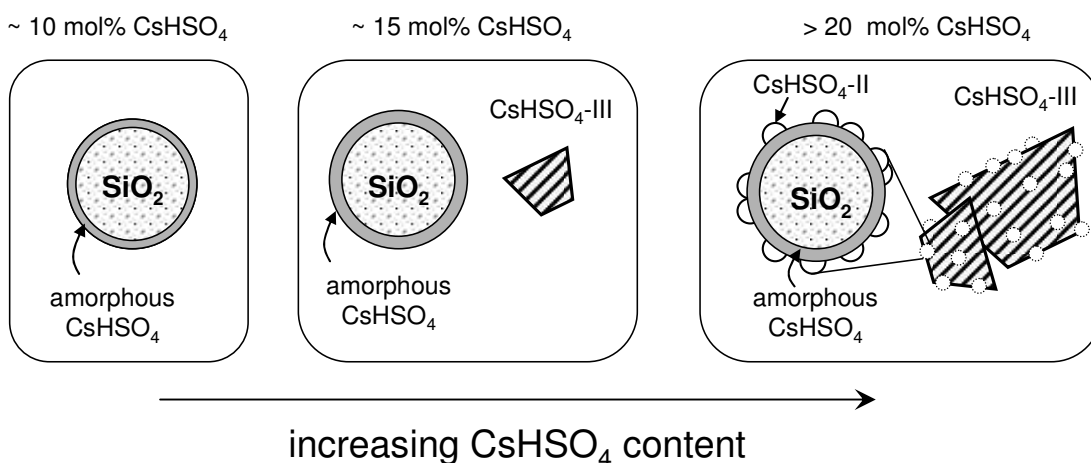
Figure 6-12 Schematic (not to scale) of the phase distribution in $CsHSO_4 – SiO_2$ composites

At small concentrations of $CsHSO_4$, the entirety of the solid acid is incorporated onto the surface of the silica in the form of an amorphous phase. A small increase in the $CsHSO_4$ concentration increases the amount of amorphous $CsHSO_4$, and also leads to direct precipitation of phase III. At higher $CsHSO_4$ concentrations, the amorphous $CsHSO_4$ serves as a nucleation size for phase II precipitation, while an increasing portion of the solid acid precipitates as phase III, independent of the silica nanoparticles.

Preliminary SEM imaging suggests that the SiO_2/$CsHSO_4$-II particles are distributed over the surface of the larger phase III particles. At the highest $CsHSO_4$ amounts, the phase III material dominates over the amorphous and phase II forms of $CsHSO_4$.

What happened after we heat the composite above the superionic transition temperature and cool it back down? Will the microstructure survive or what will be the new microstructure?

We already know, based on X-ray diffraction data that no recrystallization of the amorphous material occurs, but is there any difference between phase-II originally metastable because of the silica and phase-II metastable after cooling. Both X-ray and NMR techniques provide us with an identical diffraction pattern or NMR pattern, which consists only of one metastable phase-II, regardless of its origin (due to silica stabilization or thermal cycling) Figure 6-13.
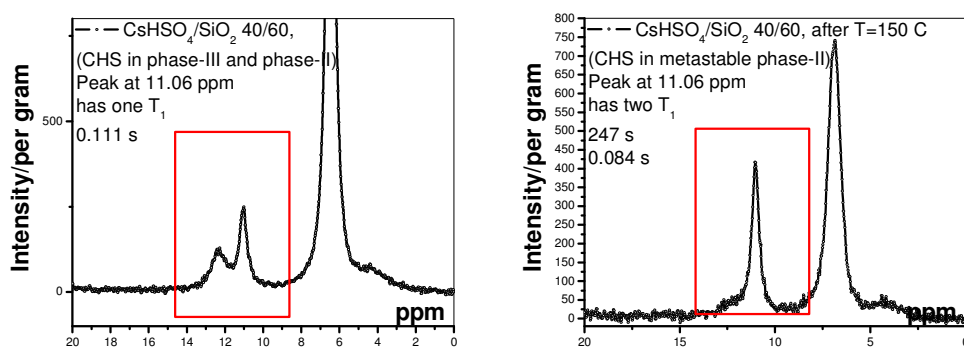
Figure 6-13 Solid State NMR of the CHS-40 composite. Original (left) and after heating to 150^0C (right). Spectra after cycling consist of one phase-II crystalline peak

Initially composites consist of phase-III and metastable phase-II (example of the typical NMR spectra is shown in Figure 6-13). Upon heating, both phases as proven by X-ray analysis transform to superionic phase-I and back to phase-II on cooling. That causes only one phase appear in the NMR spectra of the composites after thermal treatment.
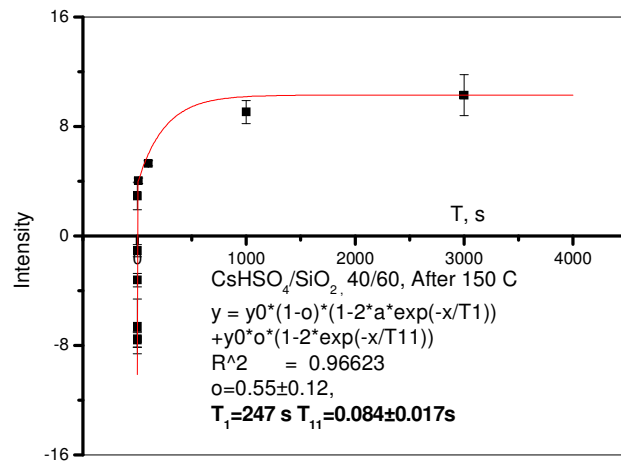
Figure 6-14 Fitting the relaxation behavior of the CHS-40 after heat treatment at 150^{0}C with two exponents

If composite microstructure is stable and original phase-III materials evolution is independent, as proposed in our hypothesis, it is possible to observe two relaxation times for one phase-II peak. Relaxation curve appears to have two components with 3 orders of difference between relaxation times. Fitting the relaxation behavior of the CHS-40 after heat treatment at 150^{0}C with two exponents was performed. That yielded two relaxation times - one with the 84 ms relaxation time represents the portion of the phase-II $CsHSO_4$ involved in the interaction with SiO_2. The other portion of the sample has a relaxation time of ~250 s, which is identical to the pure phase-II of $CsHSO_4$. The fact that relaxation

times of the SiO_2 stabilized phase-II remained the same after heat treatment suggested that composites phase interaction is stable in cycling and it is not effected by the other crystalline phase present in the system. The fraction of the SiO_2-stabilized phase-II cesium hydrogen sulfate remains relatively the same (55%) after the experiment, compared with the 49% before thermal cycling.

This technique allows us to confirm that composite microstructure is stable over thermal cycling. It still interacts strongly with nanosize silica and has reduced relaxation time values.

References

[1] Fukushima, E. and S. B. W. Roeder (1981). Experimental pulse NMR : a nuts and bolts approach. Reading, Mass., Addison-Wesley Pub. Co., Advanced Book Program.

[2] Sobol, W. T., I. G. Cameron, et al. (1987). "Stretched-Exponential Nuclear Magnetization Recovery in the Proton Pseudo-Spin-Glass Rb1-X(Nh4)Xh2aso4." Physical Review B **35**(13): 7299-7302.

[3] Eckert, H., J. P. Yesinowski, et al. (1988). "Water in Silicate-Glasses - Quantitation and Structural Studies by H-1 Solid Echo and Mas-Nmr Methods." Journal of Physical Chemistry **92**(7): 2055-2064.

[4] Mizuno, M. and S. Hayashi (2004). "Proton dynamics in phase II of CsHSO4 studied by H-1 NMR." Solid State Ionics **167**(3-4): 317-323.

[5] Damyanovich, A., M. M. Pintar, et al. (1997). "Proton pseudoglass-to-fast-ion-conductor phase transition in CsHSO4." Physical Review B **56**(13): 7942-7946.

[6] Bloembergen, N., E. M. Purcell, et al. (1948). "Relaxation Effects in Nuclear Magnetic Resonance Absorption." Physical Review **73**(7): 679-712.

[7] Abragam, A. (1961). The principles of nuclear magnetism. Oxford, Clarendon Press.

Chapter 7.   Mechanical properties of solid acids (CsHSO₄) and its composites

7.1 Introduction and theory

Solid acid electrolytes, such as $CsHSO_4$ or CsH_2PO_4, are quite brittle at room temperatures. But upon heating and above the superprotonic transition they become plastic and susceptible to irreversible deformation under stress. That can cause premature fuel cell failure. This long term mechanical stability problem has only been briefly mentioned in literature, including Uda's *et. al.* postulation that the microcracks caused by thermal expansion are mended with plastic flow of the material above superionic transition (SPT), thus leading to no alteration in conductivity[1] and solid acids' poor thermal stability[2]. Otherwise, solid acids' mechanical integrity during long term operations has remained unknown. In commercial applications, the stress by the fuel cell components and the pressures of gaseous fuel may deform the electrolyte over the duration of operation and cause fuel cell failure.

The purpose of this work is to study the mechanical properties of solid acids below and above the superprotonic phase transition. $CsHSO_4$ is a model material for these studies because it has been the most studied in the family of solid acids. Once the creep deformation has been studied and a deformation mechanism has been proposed, both findings can be used to develop a deformation model and to engineer a solid acid nanocomposite with improved mechanical properties suitable for use as fuel cell electrolytes.

Creep is a property of a material to irreversibly deform under the influence of stresses. Creep deformation occurs when a material is exposed to stresses, lower than yield module of the material over long periods of time at temperatures above half the melting temperature[3],[4],[5],[6]. When the material is exposed to the stress, first it experiences initial elastic strain. The characteristic of the elastic strain is its reversibility. If we continue to expose the material to the stress, it will experience primary, steady state creep, tertiary creep and a failure (see Figure 7-1 below). For long term stability, steady state creep contributes the most into the overall deformation.
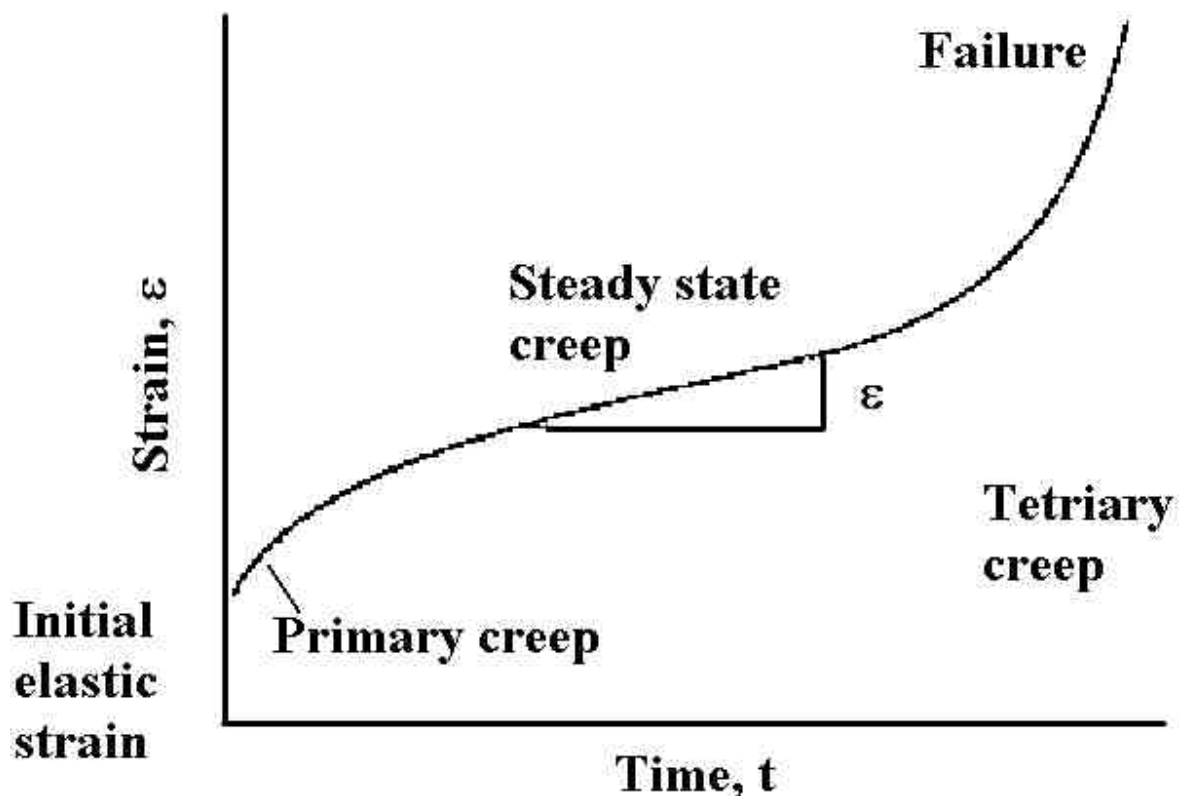
Figure 7-1 Graphical presentation of the different types of creep

For that reason we'll limit our study to the steady-state creep regime. An important characteristic of the high-temperature creep is a steady-state creep rate. There is a large body of theoretical and experimental work for the steady-state creep treatment[5].

Both theoretical and experimental data shows that creep strain rate depends on stress to the power (n) and Arrhenius dependence on temperature with the characteristic activation energy. Creep rate in this regime, for a fixed grain size, can be expressed as:

$$\dot{\varepsilon} = A \cdot \sigma^n \cdot e^{-Q/k_B T}$$

.

Equation 7-1 Creep power law.

where A- constant, σ – stress, n- stress exponent, Q-creep activation energy

The creep mechanism is usually determined by analyzing experimental data as a function of different stresses and temperatures. The mechanism dependence on the stress is presented in Figure 7-2.
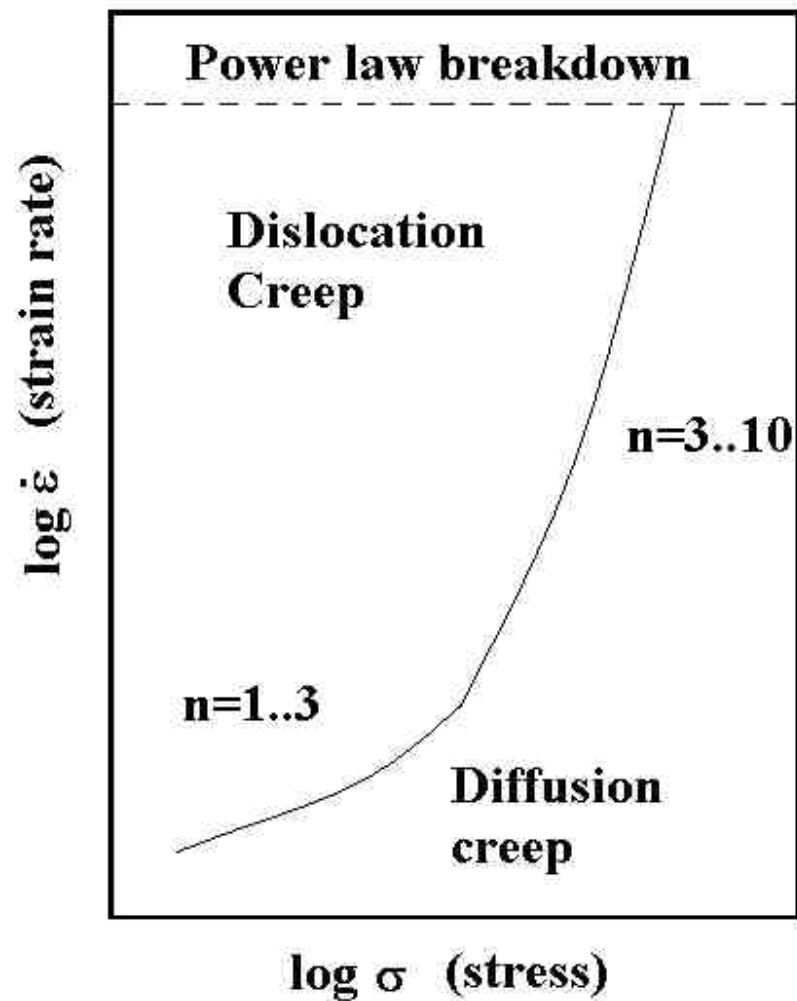
Figure 7-2 Creep mechanism dependence of the crystalline material as a function of different stresses

At low stresses and strain rates the dominating mechanism of creep is always diffusonal. That includes Nabarro-Herring creep[7],[8] Coble creep[9], Harper-Dorn[10] creep or grain boundary sliding[11],[12]. Stress exponent values are within n=1-3.

With the increase of the stress, creep is associated with some form of the dislocation creep, through dislocation glide or slip. At even higher stresses, we can

observe power-law breakdown. This transition is due to change in mechanism to the thermally activated flow[13].

7.2 Experimental design selection and solid acid sintering behavior

We will measure relative displacement under stress over time. Since we have materials with the unique phase transformation, the focus will also be to determine the effect of the transformation on the phase properties. The potential stresses during fuel cell operations are not expected to be very large. The closest well studied creep system with material possessing extensive hydrogen network is ice. Creep experiment on ice covers both low and high stress regimes with temperatures close to the melting temperatures. That allowed us to choose it as a model system. Appropriate experimental procedure and creep experiments on glacial ice were reviewed[14],[15]. Both a dilatometer and thermomechanical analyzer (TMA) were used in our study. Dilatometer can only apply force around 0.5N, while TMA can operate up to 7N.
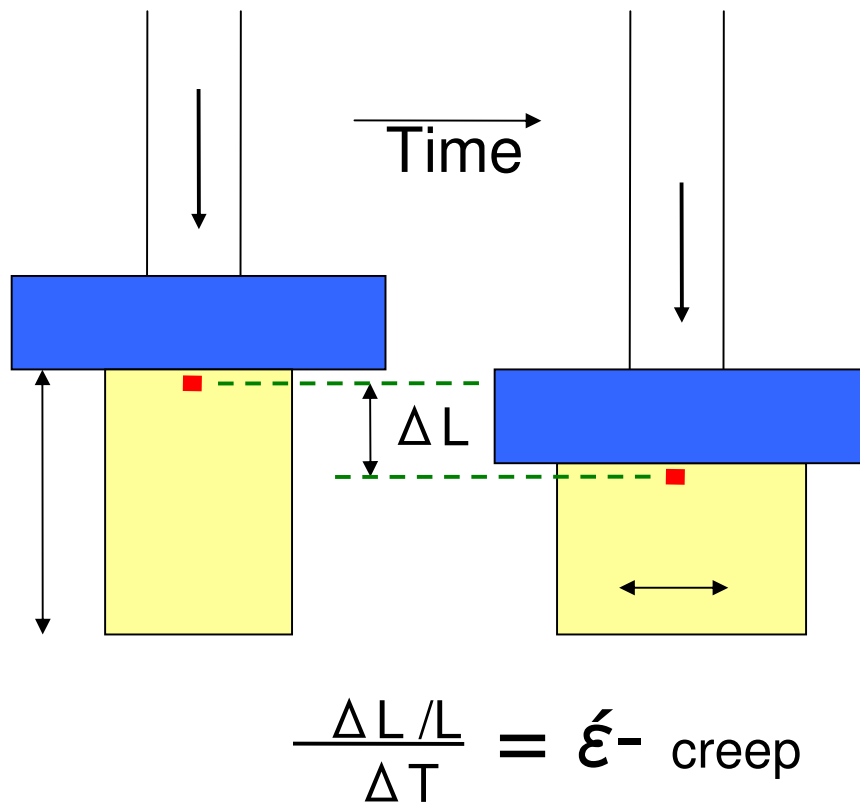
$$\frac{\Delta L / L}{\Delta T} = \acute{\varepsilon}\text{- creep}$$

Figure 7-3 Design of the compression stress apparatus

7.2.1 CsHSO$_4$ thermal stability

TGA equipped with mass spectrometry was used at a temperature range of 120 - 160 ℃ to verify that CHS decomposition did not affect creep deformation during thermal cycling that lasted 10 hours or more. The typical TGA measurement with a plot of mass loss as a function of temperature was not used but was modified to suit the purpose here. **Figure 7-4** represents decomposition as a function of time to compare the decomposition during long periods of time at temperatures $100 - 190$ ℃ ($T_m = 211$ ℃), which are conditions that reflected those occurring during thermal cycling of deformation experiments. The decomposition of CsHSO$_4$ is:

$$2CsHSO_{4(s)} \rightarrow H_2O_{(g)} + Cs_2S_2O_{7(s)}$$
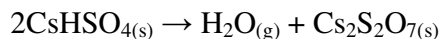
Equation 7-2

Mass loss during the decomposition is attributed to the water loss. The water product that evaporates is carried away by flowing argon, which causes a decrease in mass and is identified by mass spectrometry. Mass loss at 150 - 170 ℃ is only within 96 – 98% of the starting mass and can be attributed to the surface water. Significant mass loss starts at holding temperatures of around 180 ℃ and drastically increases near 190 ℃ and total value of mass loss at these temperatures over 10 hours corresponds to the complete materials decomposition. Those findings suggest that any long term experiments on $CsHSO_4$ without humidification are possible only at temperatures below 170^0C.
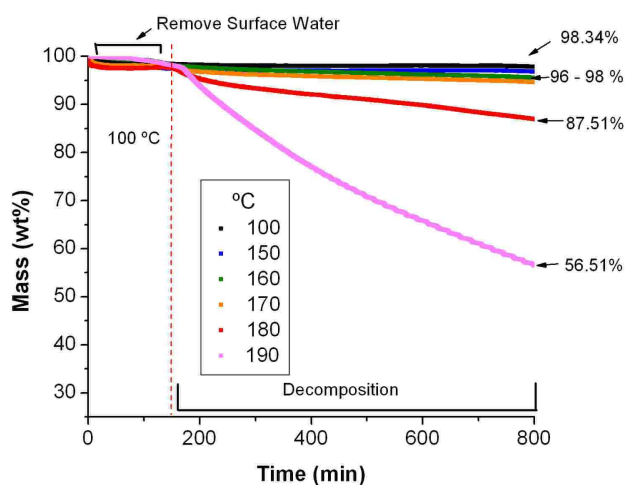

Figure 7-4 CsHSO$_4$ thermal stability (decomposition rate based on water loss measured by TGA for 800 min)

7.2.2 Experiment design and sample preparation

Cesium hydrogen sulfate was synthesized by the following equation:

$$CsHSO_4 + H_2SO_4 \rightarrow 2CsHSO_4$$

Equation 7-3

Acetone was added to the solution and stirred for 5 minutes until CHS fully

precipitated into a white powder. A Buchner funnel was used to separate the solvent from

the precipitate, which was then calcined in an oven at 80 ºC for 24 hours under stagnant

air. X-ray powder diffraction (XRD) analysis with a Philips X'Pert Pro diffractometer

confirmed the purity of $CsHSO_4$ and shown to be in Phase III. The synthesized $CsHSO_4$

powder was stored in a desiccator in order to avoid fluctuations in ambient humidity. The

$CsHSO_4$ powder was ground in an agate mortar for 5 minutes, and mechanical sieve

plates with openings of 38, 56, 106, 180 μm separated CHS polycrystalline powders at

the corresponding opening ranges. The powders were uniaxially pressed into pellets (5.16

mm diameter, 2 - 4 mm thick) under 938 MPa for 10 minutes. Only those with at least

98% theoretical density (3.34 g/cm^2) were used in experiments.

Experimental procedures were adopted and modified from ice experiments and

are as follows: only uni-directional, constant stresses were used to simplify the system;

$CsHSO_4$ pellets were deformed with stress loads of 94 kPa – 330 kPa in the temperature

range of 120 ºC - 160 ºC with a Perklin Elmer 7 thermomechanical analyzer (TMA);

deformation was measured as functions of time and temperature at constant stress loads;

and each pellet sample underwent a preliminary cycle that consisted of heating the

sample to 150 ºC and of holding it in isothermal conditions for 1 hour, while subsequent

cycles consisted of heating the sample to a desired temperature for 5 - 10 hours. Data

points were obtained during these isothermal time periods. Experiments ranged from 2-8

cycles in 24 - 100 hours. One data point was taken per second. All samples were heated and cooled at 1 ºC/min in flowing argon and free of water.

7.2.3 Sintering behavior of the cesium hydrogen sulfate. Thermal Expansion

$CsHSO_4$ exists in phase III as-synthesized and transformes into in phase II anywhere between 57-110 ºC, depends on the sample history. Phase I, also called the superprotonic phase transition (SPT), is stable above 141 ºC, and these phase transitions were noted when studying thermal expansion behavior in dilatometer. The minimal stress loads necessary were applied to the pellet in order to measure thermal expansion through simple heating and cooling thermal cycling as seen in Figure 7-5 where thermal expansions in the first and second heating cycles are plotted as a function of temperature. It should be noted that the second cycle and those that follow are identical, but are excluded for simplification.

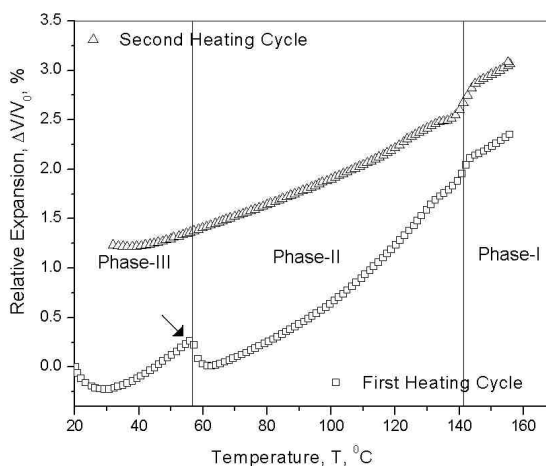**Figure 7-5 Sintering behavior at 24 kPa for $CsHSO_4$ in dilatometer**

The original experimental plan was to compare the expansion of $CsHSO_4$ *without* stress found in literature[1] to that of $CsHSO_4$ *with* stress at increasing increments, thereby

determining the thermal expansion coefficients ($\Delta V/V_o$). As stress increased, it was expected that CHS expansion would reduce until deformation began to occur.

However, the thermal expansion coefficients were not comparable because the dilatometer was limited to a small range of stress loads (1 – 24 kPa) that did not cause enough deformation in the material.

It was noticed that the first heating cycle is not reproducible as the thermal expansion slope of the first heating cycle is different from those of subsequent cycles. More importantly, a sudden, irreversible volume change occurs at 57 °C only in the first heating cycle, which also agreed with the phase III – II transition temperature. However, it should be emphasized that the volume change (arrow) only occurs during the first heating cycle and is absent in the second and subsequent cycles, which suggests that $CsHSO_4$ remains in phase II when cooled.

7.3 Determination of the creep mechanism, creep activation energies.

Creep deformation was obtained as a function of time at various stresses and temperatures. Figure 7-6 shows an example of one of the thermal cycles.
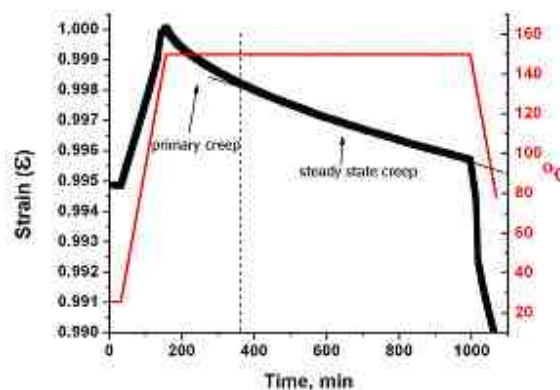
Figure 7-6 Examples of CHS deformation curves at 330 kPa at temperatures above

SPT (T_c = 141°C) Strain rates were obtained from the steady state creep

      In polycrystalline materials, it is generally found that a primary creep is followed by a steady-state creep, a tertiary creep, and then finally fracture or failure. The linear region of the strain-time curve is fitted to obtain the strain rate (εmin^{-1}) and corresponds to the steady-state creep. The steady-state creep can be described by the power law equation (Equation 7-1):

$$\dot{\varepsilon}_{ss} = A \cdot \sigma^n \cdot e^{-Q/k_BT}$$

Equation 7-4

$$\log \dot{\varepsilon} = \log A + n \log \sigma - \frac{Q}{k_B T}$$

Equation 7-5

where ε is the creep strain,

$\acute{\varepsilon}_{ss}$ is the steady-state creep rate,

A is a constant,

σ is the applied stress,

n is the stress exponent,

Q is the creep activation energy,

k_B is the Boltzmann constant,

T is the absolute temperature.

Activation energies (Figure 7-7) and the stress exponents (Figure 7-8) can be obtained from steady-state creep data as shown to have temperature dependence in Arrhenius form, Equation 7-5. These values can be used to develop a deformation model at the atomic level.
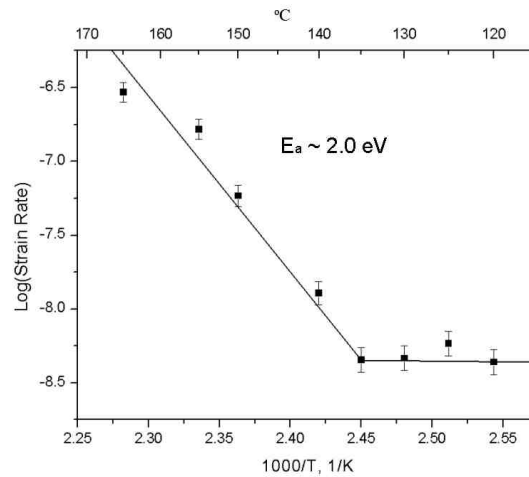

Figure 7-7 Creep deformation activation energy when σ = 330kPa. A drastic change in activation energy occurs near 141ºC, suggesting dependency on SPT. The plateau corresponds to a low E_a ~ 0.1 eV
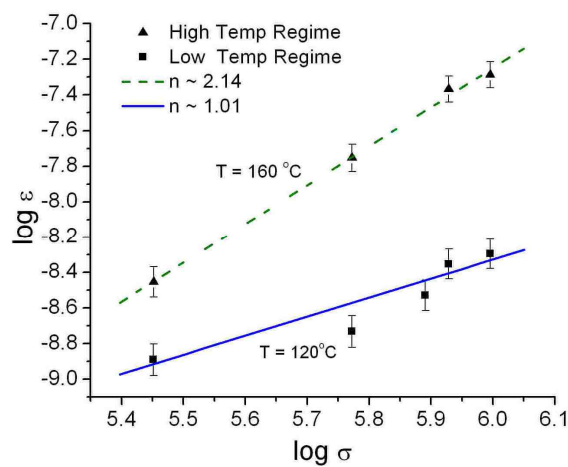
Figure 7-8 N-value fit at 120 ºC (low temp. regime) and 160 ºC (high temp. regime) when σ = 330kPa. will describe the deformation mechanisms Two distinct n-values will correspond to two deformation mechanisms

In Figure 7-7, Arrhenius form of temperature dependence of linear strain rate as plotted of logarithmic strain as a function of inverse temperature yields the activation energy for the creep deformation mechanism. Each point represents the average of at least 3 experiments. At temperatures close to SPT, the deformation mechanism transforms from one that is essentially athermal to one that is thermally activated with an activation energy of ~ 2 eV. At the lower temperature regime as seen by the plateau in Figure 7-7, the deformation activation energy is ~ 0.1 eV. This dramatic change in activation energy suggests that there are two deformation mechanisms, both of which are dependent on the SPT.

Further proof of two deformation mechanisms is displayed in Figure 7-8, where the logarithmic creep rate ($\log \dot{\varepsilon}$) is plotted against logarithmic stress ($\log \sigma$) using Equation 7-5. Two n-value values are produced and can be compared to those in literature to describe the creep deformation mechanism. The green dashed line, n ~ 2.14, represents experiments conducted at 160 ºC, and the blue line, n ~ 1.01, represents experiments conducted at 120 ºC. This n-value change is relatively drastic and displays dependency on SPT at 141 ºC. Therefore, two separate sets of evidence (one set of data is obtained as a function of stress and the other as temperature) are both in agreement that two deformation regimes exists and are dependant on SPT.

7.3.1. Dependence on the grain size

To check if creep deformation has dependency on grain size, $CsHSO_4$ grain sizes were selected by a mechanical sieve and verified with scanning electron microscopy (SEM). Figure 7-9 shows the steady-state strain rates of $CsHSO_4$ pellets with various grain sizes in the high (T = 150 & 160 ºC) and low (T = 120 & 130 ºC) temperature regimes. Although we started with different grain sizes, it was proven by the SEM that the resulting grain sizes in the pellets are very similar. That explains the absence of the strong particle size dependence of the steady state creep.
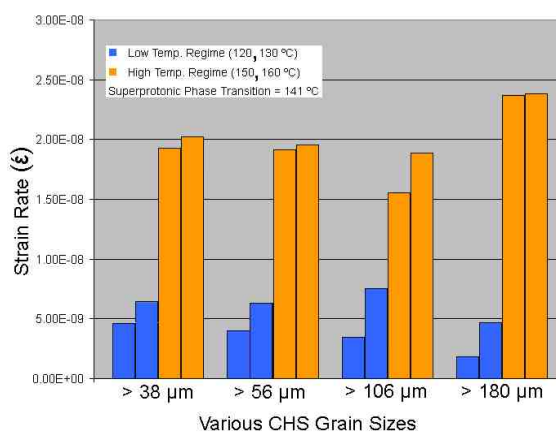
Figure 7-9 Creep dependency on grain size

Strain rates above SPT are approximately one order of magnitude greater than those below for all grain sizes. Generally, smaller grain sizes are known to strengthen materials because higher specific surface area creates more grain boundaries to resist movement[4]. The grain sizes in later experiments were not specifically separated by a sieve but were controlled through all syntheses with an average grain size of ~ 38 μm as verified by SEM.

7.3.2 Deformation mechanism
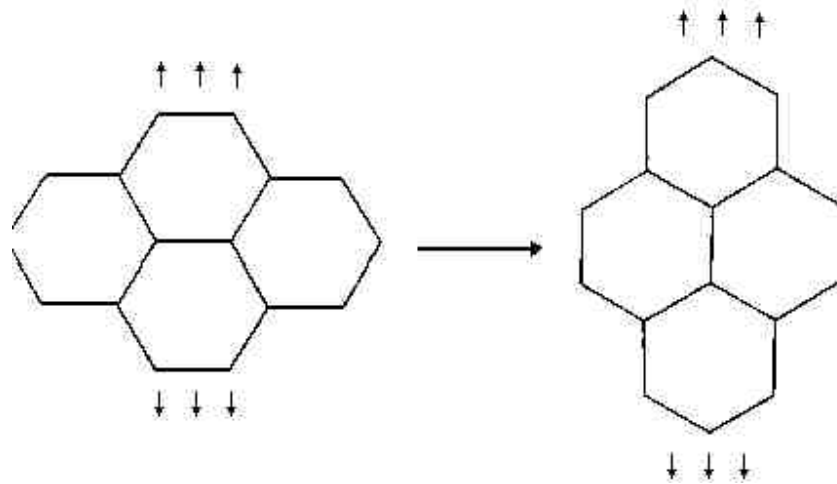
Figure 7-10. Grain boundary sliding creep mechanism
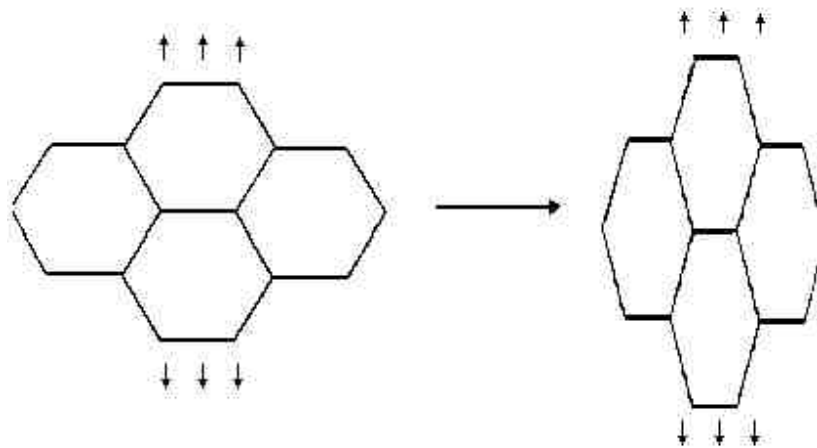
Figure 7-11. Bulk diffusion-limited creep mechanism

According to literature, deformations with stress exponents n < ~ 1 are likely to be limited by bulk diffusion, more specifically Nabarro-Herring diffusion creep in the low temperature regime[16]. Bulk diffusion creep refers to the stress-directed flow of vacancies within each polycrystalline grain as seen in Figure 7-7. A species will diffuse through the crystal lattice to maintain equilibrium. By definition, when n = 2, Rachinger

grain boundary sliding occurs[12]. Instead of diffusion within bulk $CsHSO_4$, whole polycrystalline grains begin to diffuse past one another on the grain surface to alleviate stresses and is seen in **Figure 7-10**.

The most plausible deformation mechanism above SPT, based on activation energy and values of n=2 is grain boundary sliding. It is hard to determine exactly the diffusion species, but in[17] it was stated that the diffusion in $CsHSO_4$ is limited by the slowest moving species and that cesium diffusion with E_a = 0.6 eV. Although we have an even higher activation energy of E_a = ~2 eV, that can be attributed to the fact that it is a grain boundary diffusion, and it is possible for it to have higher values.

These values and deformation mechanisms are in agreement with values reported for polycrystalline ice[14]. High temperature creep experiments performed on ice grain sizes of 25- 40 μm yielded n = 1.8 – 2.4 and E_a = 0.64 eV with grain boundary sliding as the major deformation process. This correlation may be due to the fact that both the $CsHSO_4$ used in this work and ice are both polycrystalline materials with extensive hydrogen networks deformed with low stresses.

Low temperature mechanism is likely to be limited by bulk hydrogen ion diffusion. Bulk deformation mechanism was determined based on values of n=1. Hydrogen ions have the smallest activation energy in the system, so it is reasonable to assume its bulk diffusion being the limiting step.

7.4 Possible stabilization routes

The mechanical properties of CHS were successfully investigated to characterize plastic deformation and to develop a deformation model that described behavior at the

macroparticle and atomic scale. This project is the first to correlate deformation behavior

to phase transition behavior. These findings of the first phase of research will then be

used to guide the development of solid acid materials with improved properties.

7.5 Influence of the SiO$_2$ on the mechanical properties and developing creep resistant electrolyte

7.5.1. Introduction

The second part of the Chapter will be focused on modification routes for the

cesium hydrogen sulfate, based on the proposed mechanism to decrease creep

deformation. There was a lot of work on solid acid composites focusing either on

improving conductivity properties or studying phase transition behavior without

addressing the structural integrity of the composites [18],[19],[20],[21]. However, not much was

done to suggest the novel approach that surface modification of solid acids could improve

its mechanical integrity.

7.5.2 Grain Boundaries Modification with SiO$_2$

Composites of $(1 - x)CsHSO_4$-$xSiO_2$, where $x = 0.5 – 0.9$, were prepared in a same
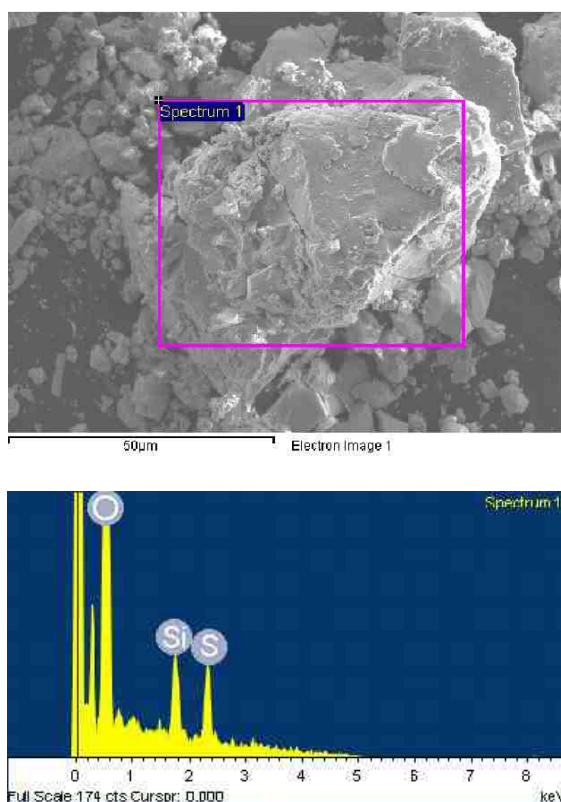
way as in Chapter 5.

Figure 7-12. EDS SEM of 0.5CsHSO$_4$-0.5SiO$_2$

Nonporous 10 nm silica, rather than mesoporous particles as used in literature, was chosen to dope the CHS surface because the former avoids pores that may complicate the system.

The understanding of the deformation mechanism of CsHSO$_4$ guided the engineering aspect of improving the mechanical strength of CsHSO$_4$. It was hypothesized that modifying CsHSO$_4$ grain surfaces with silica particles could reduce grain boundary sliding and creep deformation by increasing surface obstructions. To ensure that silica nanoparticles were present on the grain surface, SEM micrographs of the composites are shown in Figure 7-12. Although silica particles cannot be seen at this magnification,

through Energy Dispersive Spectroscopy (EDS), silica particles are present on the surface of larger phase-III $CsHSO_4$ particles.

7.5.2. Effect on structural integrity and mechanical properties

It is found that strain rates of $CsHSO_4$/ SiO_2 composites improved by 1 - 2 orders of magnitude than that of pure $CsHSO_4$.
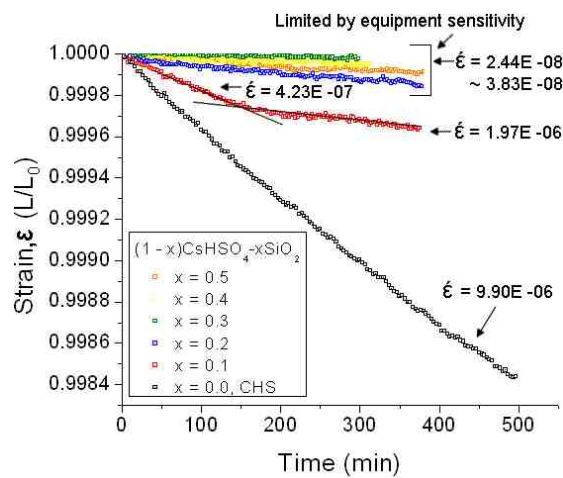

Figure 7-13. Strain rate (min^{-1}) comparison at 160 ^{o}C at σ = 335 kPa

The same experiments used on pure CHS in the first phase of research were repeated on CHS/SiO_2 composites to find strain rates (ε/min) as seen in Figure 7-13, which compares the strain rates of CHS and of CHS/SiO_2 composites. For composites (1 - x) CsHSO4 - xSiO$_2$ where x = 0.2 – 0.5, the strain rates are in the range of $\acute{ε}$ = 2.44 x 10^{-8} – 3.83 x 10^{-8} min^{-1}, and because deformations in this regime are extremely small (total deformations are < 0.01% of initial pellet height), extracting the difference between real deformation behaviors and possible instrumental errors is marginal. Because $CsHSO_4$/ SiO_2 composites are more resistant to deformation, it suggests that silica does restrict grain boundary sliding movement above SPT.

Furthermore, a unique behavior is observed. The composite where x = 0.1 (red) exhibits a strain rate ($\acute\epsilon$ = 1.97 x 10^{-6} min^{-1}) close to that of pure $CsHSO_4$ ($\acute\epsilon$ = 9.90 x 10^{-6} min^{-1}) in the first 200 minutes but flattens out afterwards, with the strain rate decreasing by about 1 -2 orders of magnitude ($\acute\epsilon$ = 4.23 x 10^{-7} min^{-1}).

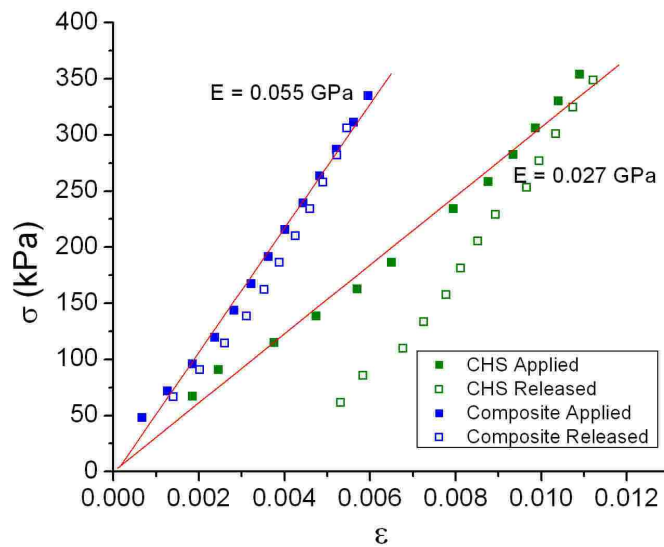**Figure 7-14. Young's Modulus comparison of pure CHS and 0.7CsHSO4 – 0.3SiO$_2$**

at 2 minute stress intervals

To further verify that silica improved $CsHSO_4$ stiffness, the elastic response (E, Young's Modulus) of the samples was measured at 160 ºC rather than at room temperature because the fuel cell will operate and undergo most deformation at the temperature in question. To avoid creep deformation that would have influenced the elastic measurements of these materials, constant stresses from 24 – 335 kPa at 25 kPa intervals were applied to the pellets at 2 minute intervals rather than the 10 hour procedures normally used to minimize influence of time-dependent creep. Measurements at 5 minute and 2 hour intervals showed the affects of creep with slightly different values

of E. For these reasons, this E value cannot be compared to other materials. But for the purpose here, the pseudo-Young's moduli values are useful to compare the stiffness of $CsHSO_4$ to that of $CsHSO_4/SiO_2$, because both systems undergo the same experimental environment and errors. In Figure 7-14 a stress/strain plot yields E ~ 0.055 GPa for $(1 - x)$ CsHSO4 - $xSiO_2$ where $x = 0.3$ and E ~ 0.027 GPa for pure $CsHSO_4$ at 2 minute stress intervals, showing that the elastic property of the composite is roughly two times better. Also, on the release it is observed that $CsHSO_4$ undergoes permanent deformation and does not return to original strain values while composites have a better elastic response. Therefore, silica surface doping of $CsHSO_4$ improves stiffness.

7.6 Conclusion

Silica nanoparticle surface modification of CHS improves mechanical integrity by 1 - 2 orders of magnitude in creep strain and is shown to have twice the elastic stiffness. Silica nanoparticles most likely acted as obstructions on the grain surface to prevent grain boundary sliding, thereby reducing deformation.

References

[1]Uda, T., D. A. Boysen, et al. (2005). "Thermodynamic, thermomechanical, and electrochemical evaluation of CsHSO$_4$." Solid State Ionics **176**(1-2): 127-133.

[2] Boysen, D. A., T. Uda, et al. (2004). "High-performance solid acid fuel cells through humidity stabilization." Science **303**(5654): 68-70.

[3] Allen, S.; T.Edwin, (1999)The Structure of Materials. John Wiley & Sons, Inc.: New York.

[4] Ashby, M.; D. R. H. Jones, (2005) Engineering Materials 1: An Introduction to Properties, Application and Design. 3 ed.; Elsevier Butterworth-Heinemann: Burlington.

[5] Langdon, T. G. (2002). "Creep at low stresses: An evaluation of diffusion creep and Harper-Dorn creep as viable creep mechanisms." Metallurgical and Materials Transactions a-Physical Metallurgy and Materials Science **33**(2): 249-259.

[6] Callister, W., (2005) Fundamentals of Materials Science and Engineering. John Wiley & Sons: Hoboken, NJ, p 154-205.

[7] Nabarro F.R.N., (1948) Report of a conference on strength of solids. The Physical Society, London**,** pp.75-90.

[8] Herring, C. (1950). "Diffusional Viscosity of a Polycrystalline Solid." Journal of Applied Physics **21**(5): 437-445.

[9] Coble, R. L. (1963). "A Model for Boundary Diffusion Controlled Creep in Polycrystalline Materials." Ibid. **34**(6): 1679-&.

[10] Harper, J. and J. E. Dorn (1957). "Viscous Creep of Aluminum near Its Melting Temperature." Acta Metallurgica **5**(11): 654-665.

[11] Rachinger, W. A. (1952). "Relative Grain Translations in the Plastic Flow of Aluminium." Journal of the Institute of Metals **81**(1): 33-&.

[12] Langdon, T. G. (1994). "A Unified Approach to Grain-Boundary Sliding in Creep and Superplasticity." Acta Metallurgica Et Materialia **42**(7): 2437-2443.

[13] Sherby, O. D. and P. M. Burke (1967). "Mechanical Behavior of Crystalline Solids at Elevated Temperature." Progress in Materials Science **13**(7): 325-&.

[14] Goldsby, D. L. and D. L. Kohlstedt (1997). "Grain boundary sliding in fine-grained Ice I." Scripta Materialia **37**(9): 1399-1406.

[15] Weertman, J. (1983). "Creep Deformation of Ice." Annual Review of Earth and Planetary Sciences **11**: 215-240.

[16] Langdon, T. G. (2002). "Creep at low stresses: An evaluation of diffusion creep and Harper-Dorn creep as viable creep mechanisms." Metallurgical and Materials Transactions a-Physical Metallurgy and Materials Science **33**(2): 249-259.

[17] Dolinsek, J. R. Blinc, A. Novak, L. A. Shuvalov, (1986). "Cs-133 and Deuteron Nmr-Study of the Superionic Transition in $CsDSO_4$." Solid State Communications**, 60**(11), 877-879.

[18] Ponomareva, V. G.; G. V. Lavrova, L. G. Simonova, (1999) "The influence of heterogeneous dopant porous structure on the properties of protonic solid electrolyte in the CsHSO4-SiO2 system." Solid State Ionics **118**(3-4), 317-323.

[19] Ponomareva, V. G.; E. S. Shutova, A. A.Matvienko (2004) "Conductivity of proton electrolytes based on cesium hydrogen sulfate phosphate." Inorganic Materials **40**(7), 721-728.

[20] Tezuka, T.; K. Tadanaga, A. Hayashi, M. Tatsumisago, (2006)"Preparation of proton conductive composites with $CsHSO_4/CsH_2PO_4$ and phosphosilicate gel." <u>Solid State Ionics</u>**, 177**(26-32), 2463-2466.

[21] Wang, S. Q.; J. Otomo, M. Ogura, C. Wen, H. Nagamoto; H. Takahashi, (2005) "Preparation and characterization of proton-conducting $CsHSO_4$-SiO_2 nanocomposite electrolyte membranes." <u>Solid State Ionics </u>**176**(7-8), 755-760.

Appendix A-1 Supplemental diffraction information

A-1.1 LaB$_6$ standard for powder X-ray diffraction

LaB$_6$ is a reference material usually used to calibrate diffraction instruments, like X-ray diffractometers or neutron sources. NIST standard of the LaB$_6$ was used to determine instrument full width half max (FWHM) it is assumed that the standard does not have any strain or size broadening. Measurements with all possible combinations of slits were performed; diffraction patterns were Rietveld refined to obtain FWHM parameter. ICSD reference # 40947 was used as a standard. Divergence slit range is 0.03125..1, Beam mask 5..20, 2 theta range 10..140 degrees.

Total number of refined parameters was 19. The following parameters were refined during Rietveld refinement:

Background, Zero shift, Scale factor, U,V,W, Lattice parameters, Preferred orientation, Asymmetry, Peak shape, B iso, site occupancy factor and thermal parameters for the La. Table 1 represents the quality of the refinement:

Table 1.

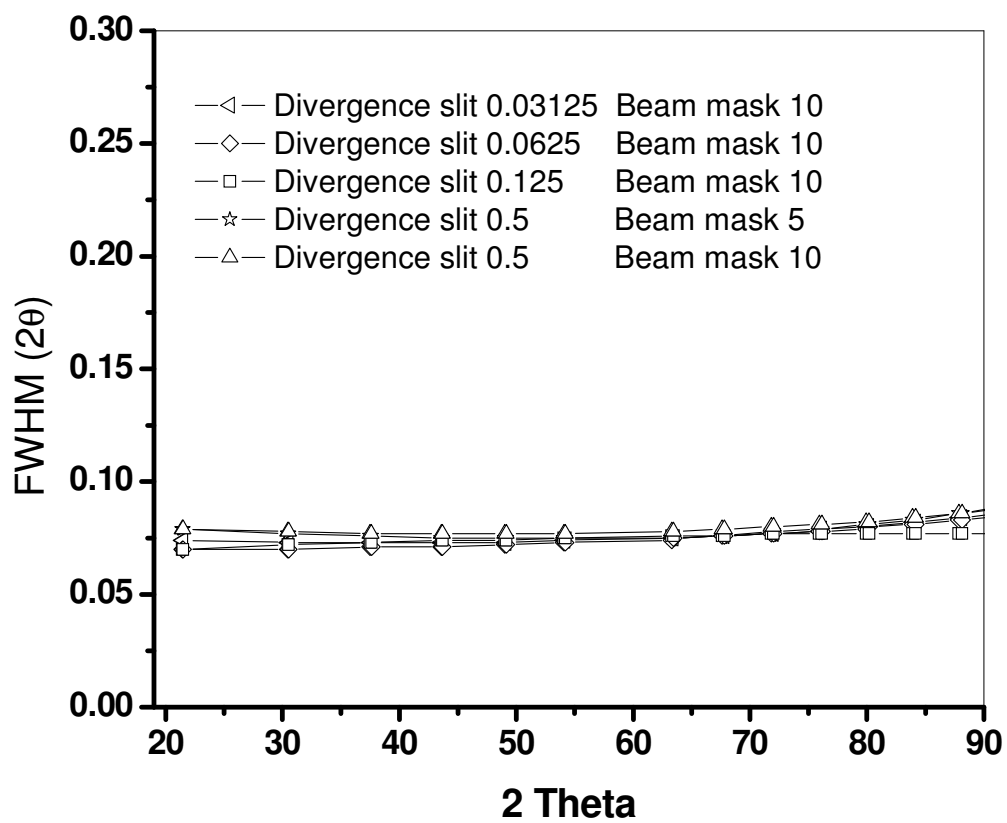| Divergence Slit	Beam Mask	R$_{ex}$	R$_{profile}$	R$_{wp}$
0.03125	10	42.61	51.93	62.51
0.125	10	22.82	17.30	23.49
0.0625	10	34.34	24.70	32.96
0.5	5	23.50	17.54	24.22
1	10	7.84	10.55	14.12
0.5	10	11.61	10.39	13.66

Figure A-1 FWHM vs. 2 theta for LaB$_6$ in different instrument configurations